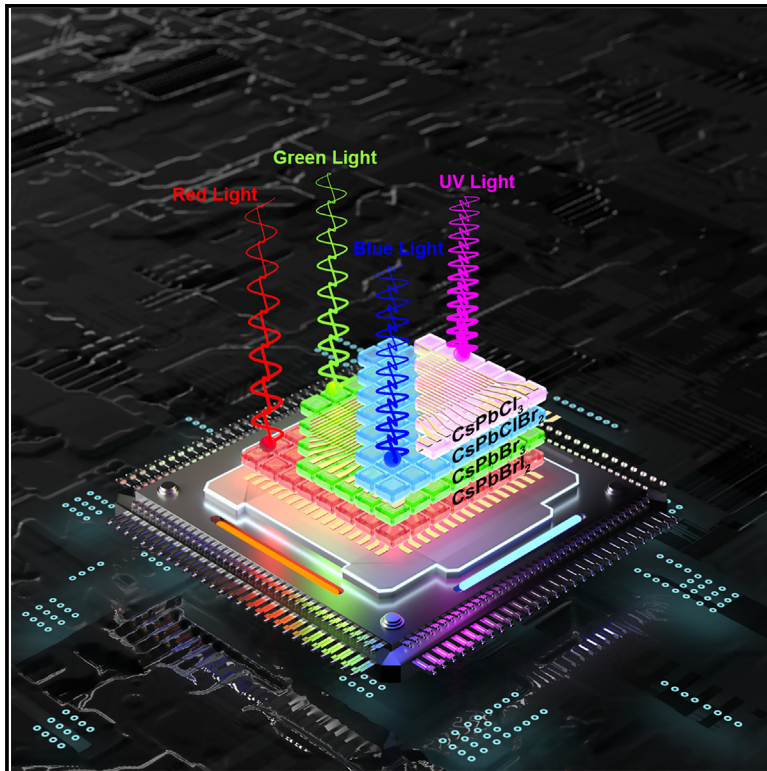


A tetrachromatic sensor for imaging beyond the visible spectrum in harsh conditions

Graphical abstract



Authors

Xiao Qiu, Yucheng Ding, Zhibo Sun, ..., Jiannong Wang, Hoi Sing Kwok, Zhiyong Fan

Correspondence

eezfan@ust.hk

In brief

The fully integrated tandem all-inorganic perovskite imaging system can detect ultraviolet, blue, green, and red light simultaneously. With four 32×32 color-selective pixel arrays, the device demonstrates reliable performance in extreme temperatures and atmospheric conditions, including aggressive thermal and vacuum cycles. The sensor offers a compact and reliable solution for tetrachromatic imaging in harsh environments, such as for space exploration and self-navigating vehicles.

Highlights

- An all-inorganic perovskite-based tandem image sensor is presented
- The tetrachromatic sensor can capture images in the ultraviolet and visible spectra
- It can operate reliably and withstand thermal cycling from 150 to 500 K



Develop

Prototype with demonstrated applications in relevant environment



Qiu et al., 2024, Device 2, 100357
May 17, 2024 © 2024 Published by Elsevier Inc.
<https://doi.org/10.1016/j.device.2024.100357>

Article

A tetrachromatic sensor for imaging beyond the visible spectrum in harsh conditions

Xiao Qiu,^{1,2,3} Yucheng Ding,^{1,2,3} Zhibo Sun,^{1,2} Haocheng Ji,⁵ Yu Zhou,^{1,2,3} Zhenghao Long,^{1,2,3} Gongze Liu,⁶ Peiyao Wang,⁷ Swapnadeep Poddar,^{1,2,3} Beitao Ren,^{1,2,3} Kemeng Zhou,⁸ Ziyun Li,⁹ Yang Bryan Cao,^{1,2,3} Zichao Ma,¹⁰ Baikui Li,⁷ Yuanjing Lin,⁸ Baoling Huang,⁶ Jiannong Wang,⁹ Hoi Sing Kwok,^{1,2} and Zhiyong Fan^{1,2,3,4,11,*}

¹Department of Electronic and Computer Engineering, The Hong Kong University of Science and Technology, Clear Water Bay, Kowloon, Hong Kong SAR, China

²State Key Laboratory of Advanced Displays and Optoelectronics Technologies, HKUST, Clear Water Bay, Kowloon, Hong Kong SAR, China

³Guangdong-Hong Kong-Macau Joint Laboratory for Intelligent Micro-Nano Optoelectronic Technology, HKUST, Clear Water Bay, Kowloon, Hong Kong SAR, China

⁴Department of Chemical and Biological Engineering, The Hong Kong University of Science and Technology, Clear Water Bay, Kowloon, Hong Kong SAR, China

⁵Tsinghua-Berkeley Shenzhen Institute & Tsinghua Shenzhen International Graduate School, Tsinghua University, Shenzhen 518055, China

⁶Department of Mechanical and Aerospace Engineering, The Hong Kong University of Science and Technology, Clear Water Bay, Kowloon, Hong Kong SAR, China

⁷Key Laboratory of Optoelectronic Devices and Systems of Ministry of Education and Guangdong Province, College of Physics and Optoelectronic Engineering, Shenzhen University, Shenzhen 518060, China

⁸School of Microelectronics, Southern University of Science and Technology, Shenzhen 518055, China

⁹Department of Physics, The Hong Kong University of Science and Technology, Clear Water Bay, Kowloon, Hong Kong SAR, China

¹⁰School of Microelectronics, South China University of Technology, Guangzhou 511442, China

¹¹Lead contact

*Correspondence: eezfan@ust.hk

<https://doi.org/10.1016/j.device.2024.100357>

THE BIGGER PICTURE With the increasing demand for image sensor technology, the integration of multi-spectral and visible/non-visible light sensing systems can help expand the capabilities of applications such as geographic remote sensing, biological monitoring, and space exploration. This research introduces an integrated wide-spectrum imaging system that combines ultraviolet and red-green-blue four-color channels, utilizing four layers of all-inorganic perovskites as the light-sensitive layers. The resulting sensor demonstrates exceptional reliability, operating consistently in atmospheric and vacuum environments from 150 to 500 K. This offers a compact solution for multispectral detection, particularly in challenging conditions for extravehicular operations and autonomous driving.

SUMMARY

A tetrachromatic light sensor can detect light in four independent color channels and extend its detection range beyond the visible spectrum. However, current tetrachromatic sensors face challenges such as the inability to work reliably in extreme temperatures. In this work, we present a fully integrated tandem tetrachromatic perovskite imaging system. Four layers of all-inorganic perovskites in the device serve as ultraviolet, blue, green, and red light detectors and can discriminate spectral and non-spectral colors. The tandem image sensor comprises four 32×32 color-selective pixel arrays. The non-encapsulated device is tested to function from 150 to 500 K under atmospheric pressure and vacuum environments. The fabrication process and device structure are scalable, with the potential to be used for tetrachromatic imaging under harsh environmental conditions.

INTRODUCTION

The biological world provides a diverse range of abilities within color vision.¹ In comparison to humans, some species of birds have cone receptors in their retinas that extend their visual range

to the ultraviolet (UV) spectrum to help them discriminate organisms with differences in UV absorption rates, navigate through the landscape, detect food and predators, and select their mates.^{2,3} In practical applications, tetrachromatic light sensors have usage in scenarios such as environmental monitoring,



including monitoring foliage and vegetation physiology by capturing multiple wavelengths of light and mapping for geology through the analysis of reflectance patterns at different wavelengths, as well as in industrial applications, such as implementation of multispectral lidar systems for autonomous driving, inspection of power infrastructure, and quality control in the industry.^{4,5}

Inorganic semiconductors, such as GaN, Si, PbS, and InGaAs, have so far been the predominant materials typically used in optoelectronics, as they offer absorption capabilities across a wide range from UV to infrared wavelengths. However, the complexity and cost of heterogeneous integration have created challenges when fabricating devices for sensing in the UV and red-green-blue spectrum (UV + RGB). Despite these challenges, recent research exploring alternative materials such as metal oxide, organic, and 2D materials has showcased promising advancements in this field. For instance, Li et al. presented a vanadium dioxide-based UV neuromorphic UV sensor for image optimization,⁶ and Wu et al. demonstrated a tetrachromatic optical synaptic device using a 2D tungsten diselenide optoelectronic p-type transistor for fully light-controlled bidirectional synaptic excitation and inhibition, emulating reindeer behavior.⁷ Jiang et al. reported a controllable UV-ultrasensitive neuromorphic vision sensor based on organic phototransistors with excellent optical figures of merit, enhancing recognition accuracy in UV image recognition.⁸ However, these works primarily focused on single-active-layer broadband image sensors and lacked the ability to accurately discriminate different color signals and reconstruct images with four channels.

Perovskite-based photodetectors have recently emerged as promising alternatives to these image sensors, with features such as high responsivity, high detectivity, fast response time, wide-dynamic-range tunable band gap, and low fabrication costs.^{5,9,10} Particularly, inorganic halide perovskites show the advantages of superior thermal stability with low-cost and efficient preparation methods. However, halide-perovskite-integrated imaging systems face challenges of solution process compatibility when more than two halide perovskite layers are stacked on each other and have poor compatibility with existing microfabrication and device miniaturization strategies, such as photolithography.^{11,12} Specifically, the existing strategies for constructing multicolor perovskite photodetectors uses either a parallel or a stacking design. Parallel structures necessitate a color filter array for monochromatic detection, which reduces efficiency, spatial resolution, and color accuracy,^{12,13} while stacking structures consist of multiterminal tandem perovskite units, thus increasing the cost and the complexity of processing, especially on pixel alignment. In this regard, integrating colorful perovskite imaging systems in one device is highly desirable.

In this work, we present a fully integrated UV + RGB all-inorganic perovskite image sensor system with four layers of 32×32 pixel arrays, in which CsPbX_3 perovskites serve as the photosensitive layers and metal oxides serve as the charge transport layers. The four sequentially thermal-evaporated perovskite layers exhibit high crystallinity, low defect density, and long carrier lifetime. The thickness of each layer is optimized through simulations to achieve over 99.5% color selectivity while maintaining high light transmittance. A tandem dual-band strategy

is used for the image sensor to dispense light without external filters and improve the optical efficacy.^{14–16} The integrated tetrachromatic image sensor works well under harsh environments, retaining over 95% responsivity after over 1,000 thermal cycles from 150 to 500 K and can remain functional down to 16 K.

RESULTS AND DISCUSSION

Selection and thickness optimization of the perovskite thin films

The tunable band gap of perovskite, modulated by halide ion mixing, enables four perovskite active layers: CsPbCl_3 , CsPbClBr_2 , CsPbBr_3 , and CsPbBrI_2 , which, respectively, mimic the UV- or violet-sensitive, short-wavelength-sensitive, medium-wavelength-sensitive, and long-wavelength-sensitive cones found in some species of birds. The CsPbCl_3 layer serves as a broadband UV image sensor, while the other layers function as single-color image sensors due to the color filter effect in the stacked architecture. As shown in Figure 1A, a thin quartz layer separates the device into two halves, one with the UV and blue sensors and the other with green and red sensors. To estimate the distribution of optical intensity and photon absorption for device design, we simulated the optical properties of all layers (Figure 1B). The required complex refractive indices (n, k) were obtained from UV-visible (UV-vis) spectroscopy and spectroscopic ellipsometry (Figure S1). Additionally, we performed optical simulation on the transmittance of four photoactive perovskite layers as a function of film thickness (Figure S2). Due to the sensor's stacked architecture, the lower layers require a high light intensity to achieve high responsivity, creating a trade-off between color selectivity and device performance. We conclude that the light leakage should be below 0.5% across the entire detection range to avoid crosstalk in light discrimination (the simulation results are shown in Figures S2 and S3). We chose the optimal thicknesses of 200, 300, 320, and 350 nm for the CsPbCl_3 , CsPbClBr_2 , CsPbBr_3 , and CsPbBrI_2 thin films, respectively. Figure 1C plots the measured transmittance of specific-thickness thin films derived from UV-vis (Figure S4). The photon absorption simulation profile shown in Figure 1C reveals that photons with wavelengths ranging from 300 to 410, 410 to 485, 485 to 520, and 520 to 650 nm are primarily absorbed in the CsPbCl_3 , CsPbClBr_2 , CsPbBr_3 , and CsPbBrI_2 layers. Indium tin oxide (ITO) electrodes, quartz, and charge-transporting layers contribute minimally to photon absorption, as substantiated by the UV-vis of these layers (Figure S4).

The perovskite layers are fabricated using a scalable physical vapor deposition process. Sequential thermal evaporation is used to achieve high-quality crystalline all-inorganic perovskite thin films with layer-by-layer process control while maintaining film uniformity, conformal substrate coverage, and compatibility with microfabrication processes.^{17,18} Figure S5 presents top-view and cross-sectional scanning electron microscope (SEM) images of the perovskite thin films and device structure, respectively. Atomic force microscopy (AFM) images in Figure S6 further verify that the obtained perovskite films are dense with a root-mean-square roughness below 20 nm. The UV-vis spectra in Figure S4 exhibit high excitonic peaks at absorption edges, which decay with the increase in absorption wavelength. This

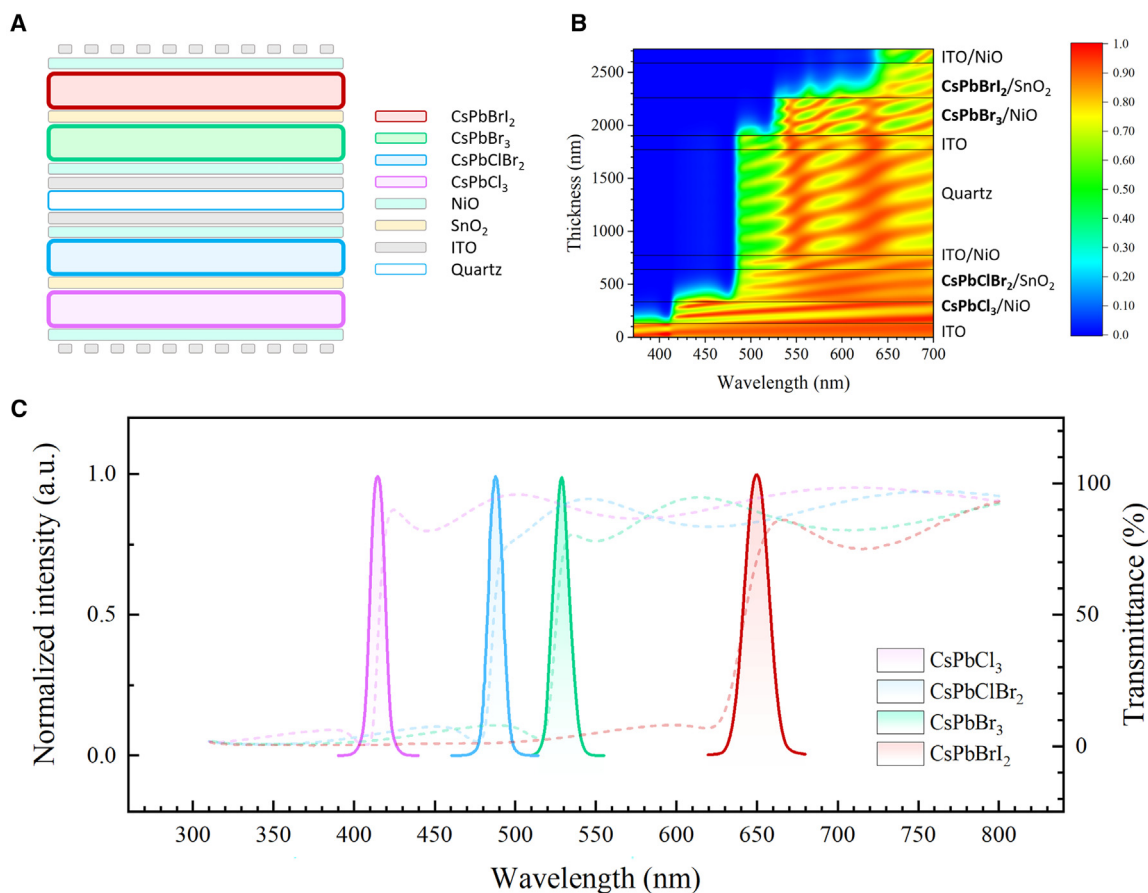


Figure 1. Overall tetrachromatic perovskite image sensor design

(A) Schematic of tetrachromatic image sensor structure.
 (B) Simulation of the wavelength-dependent optical field with respect to device position.
 (C) UV-vis and PL spectra of four perovskite thin films.

implies that the evaporated perovskite thin films have high crystallinity, as previous studies have suggested that excitons are more likely to form at locations with higher crystallinity and promote light absorption.¹⁹

The band gaps of the four perovskite materials are 3.01, 2.57, 2.36, and 1.93 eV, as estimated by the Tauc plots shown in the inset images of Figure S4. Solid lines in Figure 1F exhibit the photoluminescence (PL) with a narrow full width at half maximum (FWHM) between 20 and 35 nm. X-ray photoelectron spectroscopy (XPS) results (Figure S7) reveal a Pb 4*f* binding energy shift suggesting a strong interaction between Pb and Cl atoms in the [PbCl₆]⁴⁻ octahedral group. X-ray diffraction (XRD) spectra shown in Figure S8 confirm the high crystallinity of perovskite thin films. Specific XRD structural refinement results by FullProf are shown in Figures S9 and S10, which agree with the diffraction peaks and standard room temperature structures and show the impact of halogen ion densities on thin film stability. Except for the active perovskite layers fabricated by thermal evaporation, the remaining layers of metal oxide electrodes and charge-transporting layers are continuously prepared via magnetron sputtering. Metal oxide charge-transporting layers prepared by sputtering are dense, as substantiated by the

AFM morphology images in Figure S11. The fabrication process is shown in more detail in Figures S12–S14.

Working mechanism and basic characterization of the tetrachromatic sensor

UV photoelectron spectroscopy (UPS) and optical band-gap measurements were used to determine the valence and conduction band energies (E_v and E_c) of the NiO hole-transporting layer and the SnO₂ electron-transporting layer (ETL), as shown in Figure S15. To discriminate among the four spectral colors, we used two p-i-n-i-p structures (as illustrated by the energy-level alignment without bias in Figure 2A): one for detecting UV and blue light and the other for detecting green and red light. Each p-i-n-i-p configuration comprises a wide-band-gap perovskite p-i-n diode and a narrow-band-gap perovskite n-i-p diode. The reason for selecting SnO₂ as the ETL material is the large valence band offsets (i.e., ΔE_{v1} , ΔE_{v2} and $\Delta E'_{v1}$, $\Delta E'_{v2}$) between the perovskite layer and the n-type semiconductor.^{14,20} These offsets act as hole barriers preventing hole injection at the perovskite-ETL interface.²¹

A positive or negative bias is applied to the two side electrodes, activating one diode and deactivating the other within

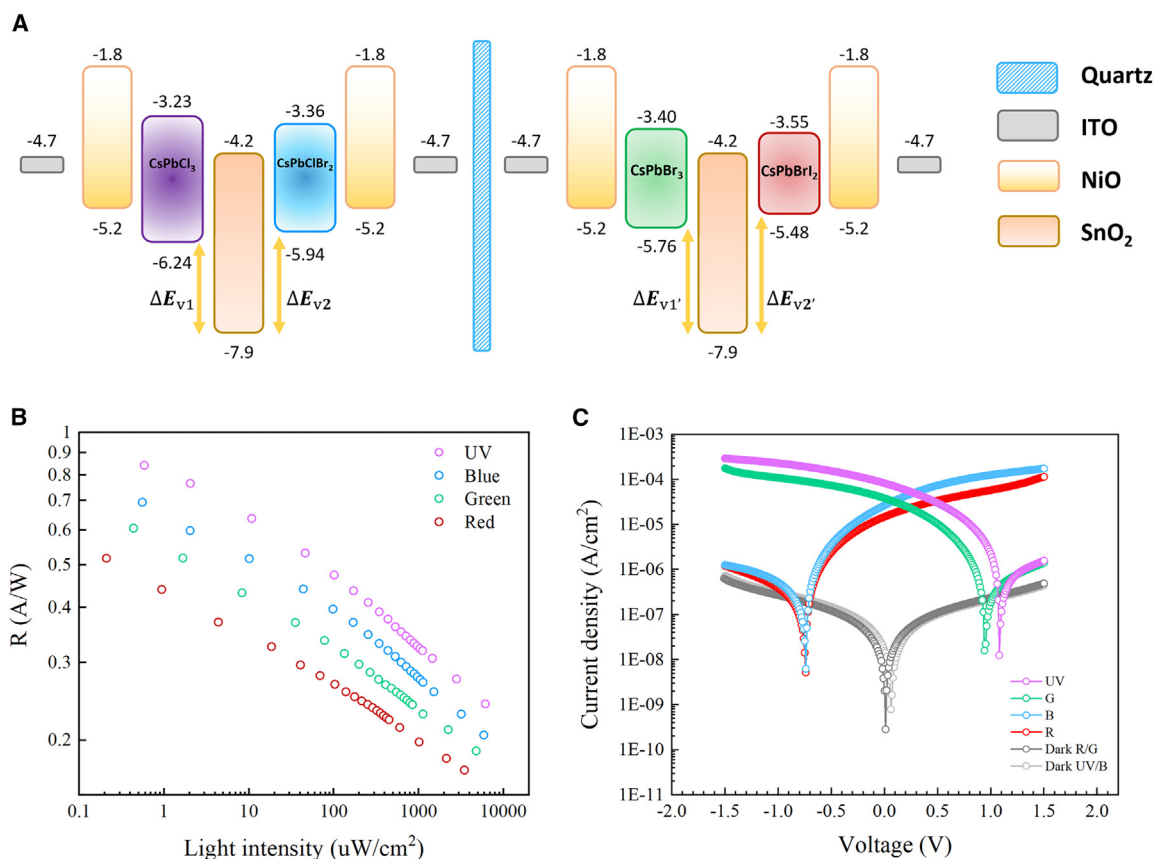


Figure 2. Photoelectric response characteristics of device

(A) Energy-level alignment of the device. The unit of the values in the energy level diagram is eV.

(B) Responsivity of the tetrachromatic image sensor as a function of incident light intensity under 405, 450, 520, and 635 nm light source.

(C) Density-to-voltage (J-V) characterizations of tetrachromatic image sensor under dark and single-wavelength illuminations.

the p-i-n-i-p configuration to distinguish short- and long-wavelength light signals. In the photodiode mode, photogenerated carriers exhibit a greater tendency to separate under reverse mode, i.e., when the positive terminal of the source is connected to the n side and the negative terminal is connected to the p side, whereas the opposite is true for the forward mode. When a positive bias is applied to the sensor, as depicted in Figure S16A, the NiO/(CsPbCl₃ or CsPbBr₃)/SnO₂ diode (p-i-n diode) is under reverse mode, while the SnO₂/(CsPbClBr₂ or CsPbBrI₂)/NiO diode (n-i-p diode) is under forward mode. The perovskite layer of the p-i-n diode serves as the photoactive layer, generating photogenerated carriers. After the electron-hole pairs separated, the electrons would drift toward the interface between the other perovskite layer and the ETL to recombine with the holes that had accumulated there due to the large valence band offset. In contrast, the n-i-p diode functions as a conduction layer, and no photocurrent is generated, even if long-wavelength light produces photogenerated carriers. These carriers cannot separate and transfer due to band bending under forward mode. Conversely, long-wavelength light is detected when a negative bias is applied, as shown in Figure S16B.

The optoelectronic properties of tetrachromatic image sensors were investigated using four single-wavelength lasers cor-

responding to UV + RGB light at 405, 450, 520, and 635 nm. As demonstrated by Figure 2B, the responsivities of the four sensors are presented as a function of a light intensity ranging from ~ 0.2 to ~ 6 mW/cm². The maximum responsivity values at 405, 450, 520, and 635 nm are 0.842, 0.694, 0.606, and 0.518 A/W under light intensities of 0.586, 0.555, 0.437, and 0.210 $\mu\text{W}/\text{cm}^2$ and applied working biases of 0.8, -1.0 , 0.8, and -1.0 V, respectively. The responsivity and detectivity values as functions of wavelength are shown in Figures 2B and S17. CsPbCl₃ responds to light with wavelengths below 410 nm, while the CsPbClBr₂, CsPbBr₃, and CsPbBrI₂ layers respond to wavelengths within 410 and 490, 490 and 520, and 520 and 650 nm, respectively. The linear dynamic ranges of all four layers are over 80 dB (Figure S18), and the noise equivalent powers of the device are calculated to be 3.7×10^{-13} W Hz^{-1/2} at 410 nm, 5.6×10^{-13} W Hz^{-1/2} at 450 nm, 7.0×10^{-13} W Hz^{-1/2} at 520 nm, and 8.6×10^{-13} W Hz^{-1/2} at 635 nm.

We assumed that random fluctuations in the applied current dominate the dark current, and we measured it under a working bias (0.8 V for positive bias and -1.0 V for negative bias). The photoresponse rise time and fall time of the sensors range from 0.85 to 16.2 ms (see Figure S19), and the response times for all photoactive layers increased as the layer thickness

increased. To assess the performance of our device in comparison to the relevant performance of perovskite photodetectors reported in previous works, we present a benchmark in Table S1. The current density-to-voltage curves are displayed in Figure 2C, which reveal that the UV and G diodes operate with a positive bias, while the B and R diodes function with a negative bias, respectively. Given that the open-circuit voltage (V_{oc}) increases with light intensity as a logarithmic function, we opted for relatively higher light intensities for function demonstration and selected 0.8 and -1.0 V as the working biases to obtain stable photoresponse currents and minimal noise from other photoactive layers.

To further understand the color selectivity of the four wavelength ranges, we conducted more color discrimination tests, as shown in Figures 3A–3D. The mixed light sources of UV + B and G + R activate the device separately at the given bias. For instance, Figure 3A shows the photoresponse cycles under UV detection mode with the UV laser being switched on and off while the blue laser stays on. The enlarged pictures in Figure 3A present a negligible difference between dark current density and the current density under high blue irradiance under a working bias of 0.8 V. This implies that blue light barely interferes with the device performance in the UV detection mode. Similarly, the other three detection modes are also demonstrated. Although the current generated by the non-working layer (e.g., the blue layer would be the non-working layer when the UV layer is working) flows against the main current, the current density of this interference is low enough and can be disregarded.

Testing under harsh environmental conditions

Owing to the all-inorganic components of the tetrachromatic image sensor, the device can be used for imaging in harsh conditions, such as under thermal shock and thermal cycling. Temperature-dependent XRD and PL measurements are used to understand the evolution of material structure and optoelectronic properties. Using XRD, we explored the perovskites' lattice distortions and phase transitions under temperature variations ranging from 170 to 570 K (Figure S20). As shown in the Figures 4A–4D, peak shifts for the crystal planes 001, 011, and 002 of the cubic phase at high temperature (or 002, 022, and 004 of the orthorhombic phase at low temperature) can be observed throughout the temperature range, while some other peaks appear and disappear due to the phase transitions.^{22–24} Interplanar spacings of all four perovskites expand as the temperature increases, as shown in Figure S21, which can be seen from the 100 peaks at 15.93° , 15.57° , 15.30° , and 14.80° at 170 K shifting to smaller values at 570 K for CsPbCl₃, CsPbClBr₂, CsPbBr₃, and CsPbBrI₂, respectively. Peaks corresponding to the 111 plane emerge when the materials are cooled to their phase transition points (Figure S22). For example, one peak of CsPbBrI₂ at 41.6° weakens at 415 K and another appears at 44.5° at 240 K. Due to the small temperature range of the tetragonal phase, particularly for CsPbCl₃, we provide a more detailed comparison of the lattice constants and volumes derived from the temperature-dependent XRD in Figure S23, which shows the phase transitions. While positive volume expansion coefficients for crystal units are observed in all mate-

rials, the anisotropic thermal expansion of individual lattice spacings is consistent with existing literature.^{24,25}

The optoelectronic properties of the four inorganic perovskite materials were measured using PL from 140 to 500 K, as shown in Figures 4E–4H. The subtle peak shifts to shorter wavelengths during heating suggest a slight enlargement of the band gap due to the synergistic effects of thermal expansion and electron-acoustic phonon interaction.²⁶ The PL FWHM broadening, as depicted in Figure S24, has been used to estimate the phonon scattering and electron-phonon coupling in semiconductors.^{27,28} Previous studies have suggested that the predominant factor of PL broadening above 100 K is not from acoustic phonon scattering but from electron longitudinal optical phonon interactions.²⁹ This may result in higher electron scattering in perovskite thin films within the high-temperature regime. The peak intensity increase during the cooling process suggests higher radiative recombination and lower defect density, even in the presence of a transition from a high-symmetry crystal structure to a low-symmetry one.³⁰

Responsivity measurements were carried out under various temperatures and pressures (shown in Figures S25 and S26). Pressure-dependent performance showed negligible changes from vacuum to atmospheric pressure. We found distinct steps in the curves indicating the variation of responsivity with temperature in Figures S25A and S25C, while there were no such steps in Figures S25B and S25D. We conjecture that the phase transition process in pure halide perovskite is significantly faster compared to that in mixed-halide thin films. Previous works on solar cells have indicated that the short-circuit density would decrease in the high-temperature regime^{31–33} or stay within a certain range in the low-temperature regime.^{30,34} The divergence in our results may be caused by different test conditions, device components, or structures. We hypothesize that at higher temperatures, injected holes possess greater thermal energy. This increased thermal energy facilitates the holes to drift across potential barriers and allows them to move more easily from the ITO/NiO layer to the perovskite layer at the forward mode junction, resulting in an increase in photocurrent. In addition, the dark state current density exponentially increases with the increased temperature, resulting in the decrease of V_{oc} and the on/off ratio.

To evaluate the operational and thermal stability of the device, we implemented two thermal cycling setups designed to simulate thermal shocks experienced in space applications (refer to Figures S27C and S27D). After running 1,000 cycles by gradually heating to 500 K and cooling to 170 K at a rate of 50 K/min, all four photoactive layers retained a responsivity of >95%. The device experienced less decay during these gradual thermal cycles than when kept at a constant temperature condition (Figure S27A). This is because of the crystalline reconstruction and defect repair after annealing at high temperatures. Even when the device is subjected to a more sudden thermal cycle of heating and cooling by transferring between a hotplate at 500 K and a vacuum environment at 170 K, the device retained >96% of its performance over the test that lasted 20 cycles. We also conducted photoresponse measurements at the extreme low temperature of 16 K (Figure S28), and the device maintained stable operation (responsivity over 95%) throughout the 1 h

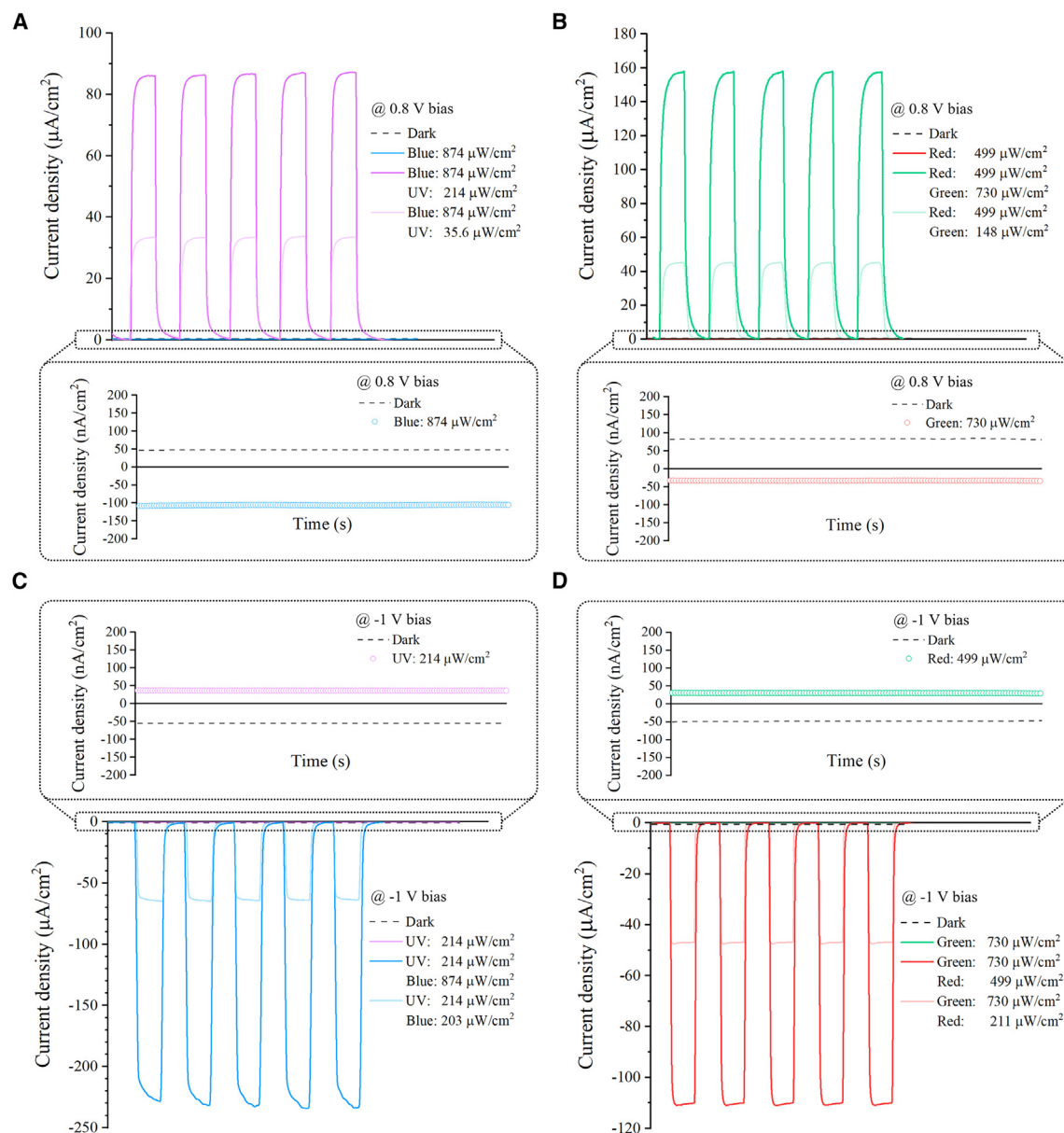


Figure 3. Photocurrent response of mixed light source

Photocurrent response of mixed light sources of 405 and 450 nm (A and C) and 520 and 635 nm (B and D) at forward working mode (A and B) and reverse working mode (C and D), respectively. The enlarged pictures depict the device's current densities under dark and light conditions, showcasing the device's ability to generate low interference signals even in mixed light environments.

measurement. The operational stability in high-temperature regimes (500 K) with the device soaking under various wavelength lasers for over 1 day (shown in Figure S29) reveals only slight performance degradation when operating at high temperatures.

The durability of the device under ambient and vacuum conditions is shown in Figures S30–S32. The estimated T_{90} values, which represent the lifetime at which the responsivity is diminished by 10%, were approximately 1,800, 650, 510, and 380 h, respectively, under vacuum testing for the four layers. While CsPbBr₂ demonstrates good stability under vacuum conditions, it experiences a significant degradation when stored in ambient

conditions. This degradation is primarily attributed to the presence of oxygen and water vapor in the air, which can react with the material and lead to hydrolysis and the subsequent breakdown of the crystal lattice. Furthermore, the specific composition and structure of CsPbBr₂, characterized by a low tolerance factor, render it less chemically stable compared to other halogen perovskite materials.³⁵

To further test the stability of the four perovskite materials under harsh conditions, we heated them up to 200°C and annealed for 100 h. The SEM images of thin films' morphology show negligible differences before and after annealing (Figure S33) except

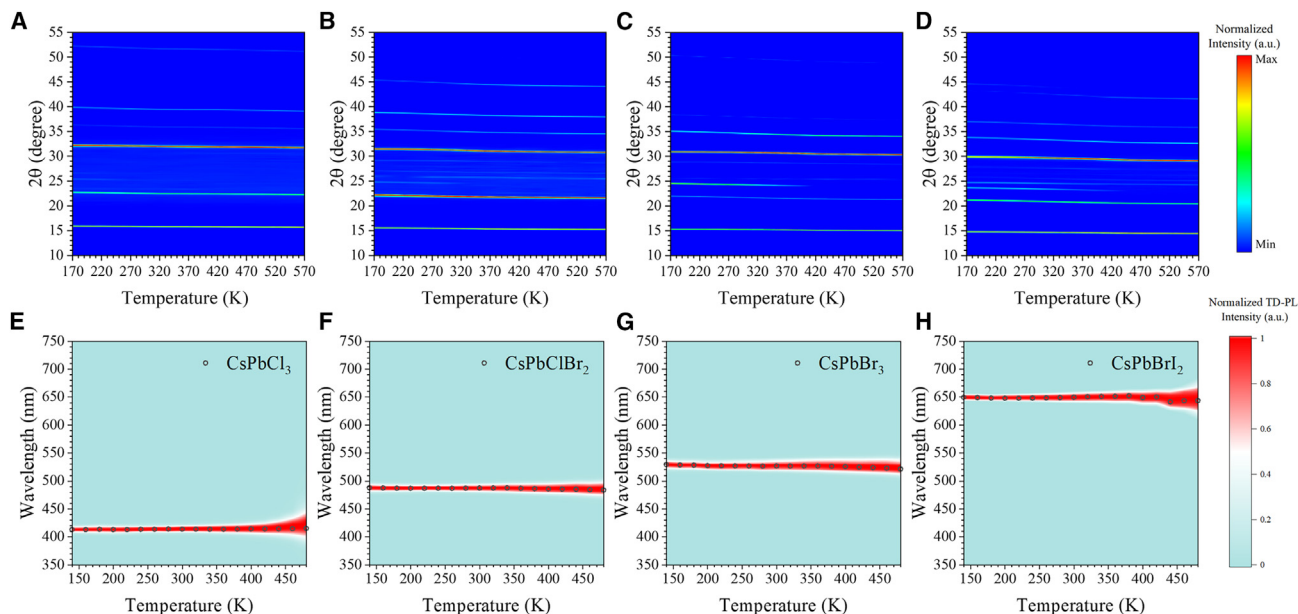


Figure 4. Temperature-dependent XRD (TD-XRD) and PL characterizations of the perovskite thin films

(A–D) TD-XRD contour map of CsPbCl₃, CsPbClBr₂, CsPbBr₃, and CsPbBrI₂ thin films.

(E–H) Contour map of normalized TD-PL spectra of four materials as a function of temperature. The black scatter circles point out the peak positions of each temperature.

for CsPbBrI₂, which is mentioned in the figure caption. As demonstrated in Figures S9 and S10, the XRD peaks of the three CsPbX₃ materials with varying Cl and Br ratios show minimal changes before and after annealing, with no notable formation of additional peaks. In contrast, as indicated in Figures S10C and S10D, CsPbBrI₂ exhibits significant changes in its XRD pattern marked by the appearance of the peaks for CsBr and PbI₂. This reflects a substantial alteration in the crystal structure attributed to the poor phase stability of CsPbBrI₂-type materials, which tend to undergo phase separation and transformation.^{25,36,37} To further examine this, we extracted the halogen vacancy content from the four perovskite materials after the temperature treatment. The results shown in Figure S34 indicate minimal impact on the two Cl-containing perovskite materials, CsPbCl₃ and CsPbClBr₂, with halogen vacancy levels below 2%. In contrast, CsPbBr₃ shows a modest increase in vacancy content (3.52%) after annealing, while CsPbBrI₂ exhibits the largest change with a halogen vacancy proportion of 6.19%, closely correlated with the formation of the additional peaks of decomposition product, proving that the material undergoes significant phase segregation during the annealing process.³⁸ It is crucial to emphasize that halogen vacancies do not imply the loss of halide ions but rather their migration and phase transition behavior.

Tetrachromatic color discrimination and imaging demonstration

To benchmark the device's discrimination capabilities and eliminate chromatic aberration from light sources, we measured absolute light intensities and relative intensity ratios using 405, 450, 520, and 635 nm single-wavelength lasers as light sources. To

control the combinations, we modulated the light intensities. In Figure 5A, each pair of black and white scatter points in the 3D tetrahedral and ternary images are in close proximity, indicating a high degree of resemblance between the reconstructed light combinations and the original light ratios. We further evaluated the variation between actual and detected values in Figure 5B. The blue box (UV/B/G) shown in Figure 5B illustrates a much smaller distance than the other three boxes, which means that the R layer plays a substantial role in the overall deviation (shown as the light pink box UV/B/G/R). Similarly, we inferred that the deviation of each layer occurs in the descending order of R, G, B, and UV layer. This phenomenon is likely caused by the light intensity calibration, as well as scattering and reflection when light passes through the multilayer interfaces. More details can be found in Note S2.

To demonstrate the imaging capabilities of the tetrachromatic image sensor, we created a 4 × 32 × 32 pixel sensor array with a pixel line width of 100 μm and a pixel pitch of 400 μm. The sensor array is integrated with readout circuits and on-chip temperature and pressure sensors, as shown in Figures 6A–6C. We tested the device in vacuum (Figure 6D), low-temperature (Figure 6E), and high-temperature (Figure 6F) environments using images of Earth, Neptune, and Venus from the National Aeronautics and Space Administration (NASA) to simulate the space environment, and an image of the Crab Nebula from NASA was used as the target in the ambient environment. We also used the sensor array to image a fuel stove, which can emit UV radiation (Figure 6G) at high temperature. We also used a filtered UV light-emitting diode backlight and patterns to demonstrate the UV channel's functionality further. The UV, B, G, and R channels are displayed separately to assess the image quality of each

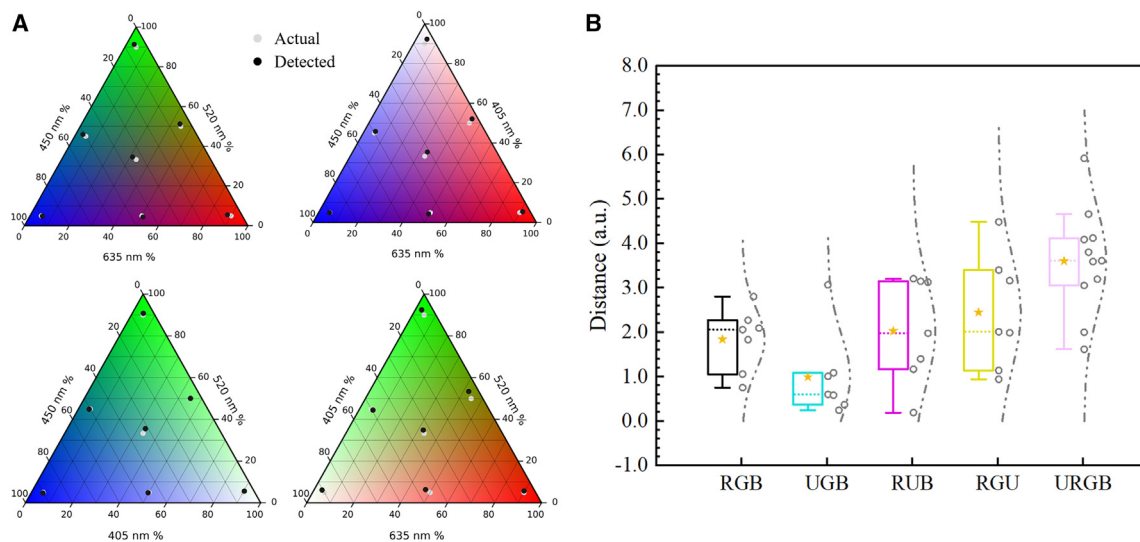


Figure 5. Capability of the tetrachromatic image sensor system to discriminate mixed lights

(A) Ternary light combination maps based on 405, 450, 520, and 635 nm light sources.

(B) Standard deviation of five maps that show the deviation of actual light combination and detected light combination after calculation.

channel (Figures S35 and S36). All channel figures were corrected according to the temperature coefficients from the temperature-dependent data of responsivity (Figure S25) in the image output process. The original images of low- and high-temperature demonstrations are presented in Figure S36. Small deviations were observed between the real and reconstructed images in a vacuum, and the deviations are more noticeable at high temperatures, corresponding closely to the temperature coefficients. Considering this, we installed on-chip sensors to provide feedback for calibrating the output data to produce better results (see Figure 6H). The UV/B channels exhibit higher accuracy than the R/G channels, which is consistent with the light discrimination results as aforementioned.

Conclusion and outlook

We have developed an all-in-one tetrachromatic image sensor system with a $4 \times 32 \times 32$ pixel configuration. The sensor uses two electrically switchable color-selective p-i-n-i-p structures to discriminate four wavelength ranges by using four perovskite layers with tunable band gaps. We measured the effects of temperature and pressure on the phase transition, lattice distortion, and optoelectronic performance of the four perovskites. Our research aims to enhance the performance and stability of various perovskite sensors for working in harsh environmental conditions. The tetrachromatic sensor can reproduce high-accuracy images under harsh environments even after being subjected to thermal shock cycles and changing pressures. However, the challenges of crosstalk and pixel size persist as the primary obstacles to miniaturize the device and increase its resolution. To address these challenges, we are investigating approaches including the incorporation of insulating layers,^{39,40} electrode isolation,¹¹ and optimization of electrode geometry. Additionally, we are exploring the potential of using thin-film transistors and complementary metal-oxide-semiconductor substrates as viable

alternatives to crossbar electrodes. These advancements provide a possibility of fabricating high-resolution pixel arrays in the near future. This device may find applications in space exploration, where sensors are required to be remain stable and durable under extreme temperatures and vacuum conditions while providing the ability to detect a wide range of wavelengths, including visible light, UV light, and other parts of the electromagnetic spectrum. This device offers a wide spectral response and high sensitivity, enabling the detection and analysis of diverse electromagnetic radiation wavelengths, and may also find uses in self-driving cars, artificial retinas, and industrial system monitoring.

EXPERIMENTAL PROCEDURES

Resource availability

Lead contact

Requests for further information, resources, and reagents should be directed to and will be fulfilled by the lead contact, Zhiyong Fan (eezfan@ust.hk).

Materials availability

This study did not generate new unique reagents.

Data and code availability

The data that support the findings of this study are included in the main text and the supplemental information. More data are available from the corresponding author upon reasonable request. The source codes for MATLAB and Python are available from the corresponding author upon reasonable request.

Materials

All chemicals were purchased from Xi'an Polymer Light Technology and used as received without further purification.

Simulations

Below are the details of the optical simulation conducted for the design of the tetrachromatic all-inorganic perovskite image sensor. For the optical simulation for the design of the tetrachromatic image sensor, a numeric computing environment developed by MathWorks (Zenodo link: <https://doi.org/10.5281/zenodo.10781549>) (MATLAB) was used to simulate the transmission

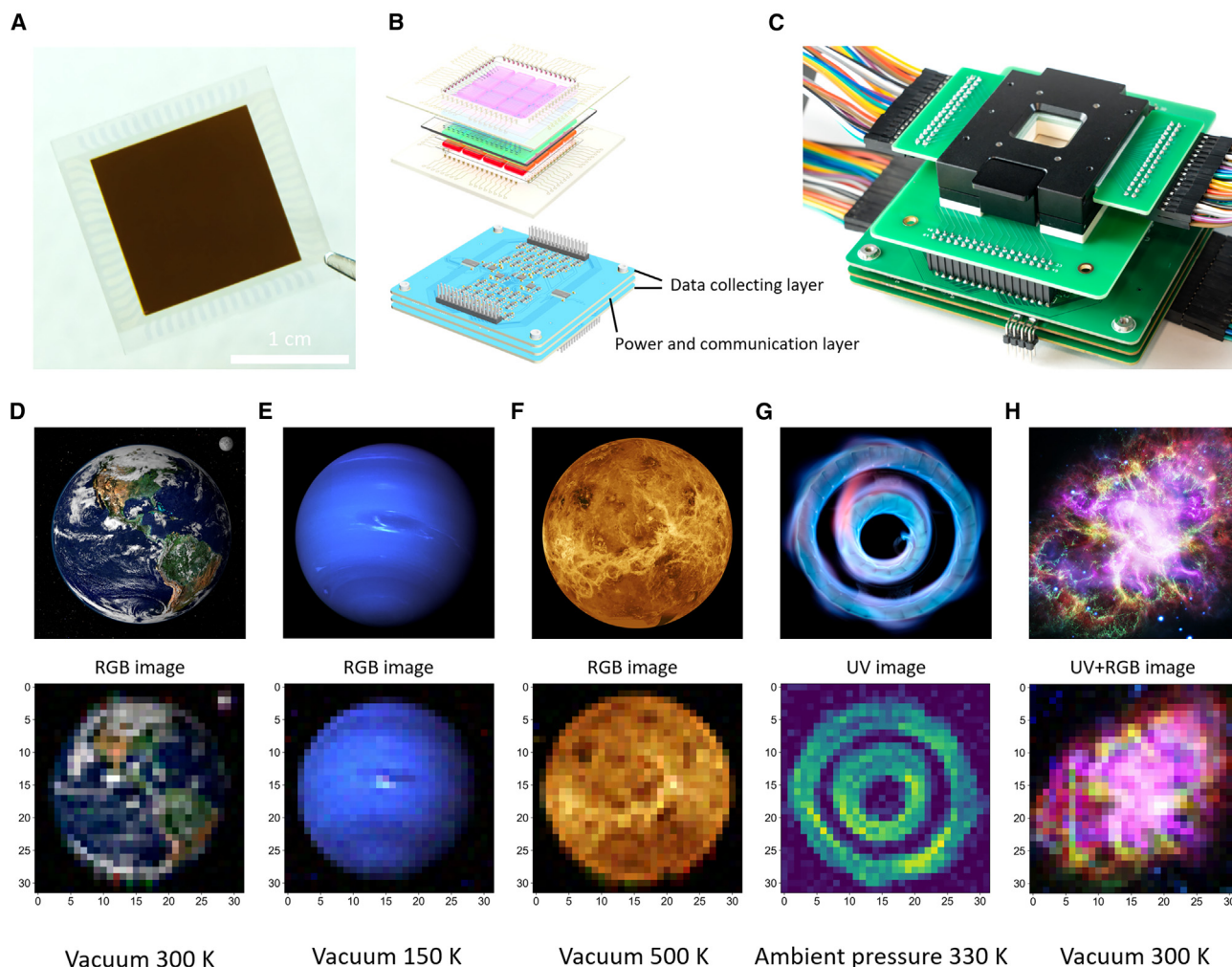


Figure 6. Image detection demonstration in the extreme environment

(A) Image of the four-layer device.

(B and C) Schematic (B) and image (C) of the tetrachromatic image sensor system.

(D–H) Photographs and captured images of Earth (D), Neptune (E), Venus (F), flame (G), and Crab Nebula (H) in different environments (labeled in the images). Notably, the fuel stove emblazened the flame, and the projector projected the other pictures. The calculated output image of flame detection was UV channel, while other images were RGB channel.

versus the wavelength and thickness of different perovskite materials (see [Figure S2](#)) based on the refractive index and absorption (n , k) measured by the ellipsometer (J.A. Woollam M-2000VI). The simulation is based on the multi-layer interference theory, which is widely used in designing antireflection coating. By adding the absorption term of the refractive index and the refraction factor of the incident angle, the reflective and transmissive spectra are influenced by the real and imaginary parts of the index of refraction layer by layer. Then, the angular dependence of the image sensor, especially the cross-talk between the neighboring pixels, is calculated (see [Figure S3](#)). Based on those simulation results, the performance of the tetrachromatic image sensor is designed with a critical thickness for different layers including all the layers in the sensor.

Fabrication of tetrachromatic all-inorganic perovskite image sensor

Double-sided ITO-patterned (ITO thickness is 120 nm on each side) quartz plates (100 μm line width and 400 μm pitch as shown in [Figure S12](#)) were cleaned in sequence with detergent, deionized water, ethanol, acetone, and isopropyl alcohol by an ultrasonic washer. Before use, ITO-coated substrates

were dried by N_2 and exposed to O_2 plasma for 10 min. More details about the fabrication processes can be found in [Note S1](#).

Characterization of material and photoresponse

Complex refractive indices (n , k) and UV-vis absorption and transparency spectra of four perovskite materials were obtained using J.A. Woollam M-2000VI Spectroscopic Ellipsometer and Lambda 1050+ (PerkinElmer). Surface morphology of thin films was carried out on the Dimension ICON (Bruker). A field-emission SEM (JSM-7100F, JEOL) was used to characterize the device's top view and cross-section view under an acceleration voltage of 5 or 10 kV. The XPS and UPS spectra were recorded on a PHI 5000 Versa Probe III. TD-XRD spectra were derived from an X-ray diffractometer (Rigaku SmartLab, 9 kW, Cu target, BB geometry). Temperature-dependent PL measurements were carried out on the QE-Pro spectrometer (Ocean Insight) and Newton 920 CCD (Oxford Instruments). The emission wavelength used in the measurements was 266 nm, and the sample temperatures were controlled by the Linkam Optical Shearing System (CSS450). As for the photoresponse characterization, we used an optical power meter (Thorlabs, PM100D) to

calibrate the light intensity. The 3 and 30 mW lasers of 405, 450, 520, and 635 nm controlled by a pulse-width modulation controller were used as single-wavelength light sources, and we used neutral-density filters to adjust the light intensities. A xenon lamp with grating served as a wavelength-tunable light source (300–900 nm). The current-time curves and current-voltage curves of devices under high- and low-temperature conditions were measured by TTPX Cryogenic Probe Station, Lake Shore model 336 Cryogenic Temperature Controller, and a Keithley 2450 source meter and with a liquid nitrogen tank. All temperature-dependent measurements had a temperature step and holding time of 20 K and 10 min, respectively.

Integration of tetrachromatic all-inorganic perovskite image sensor system

We designed the test system as shown in Figures S36 and S37. For both UV/B and R/G layers, we used two 16-channel multiplexers (ADG1606) for row selection. In each column, there was one transimpedance amplifier (based on AD8615), one amplifier (AD8615), and one 16 bit analog-to-digital converter (ADC; ADS1110). All 32 ADCs were connected in series with an I2C bus for output. The microcontroller unit (MCU) used in this design was the ESP WROOM 32D. This MCU was responsible for scanning the photodetector arrays, processing the signals, and communicating the data to external devices. The I2C bus connected the MCU to the ADCs, enabling seamless data transfer. The printed circuit board was also embedded with one temperature sensor (DS18B20U) and one pressure sensor (BMP280) to monitor environmental conditions (Figure S39).

Demonstration under normal and harsh conditions

We calibrated every pixel by taking dark and flat files under room temperature (298 K), and flat-field images were taken under a 3 mW/cm² light source. The images were projected on the image sensor by a projector with two convex lens sets. The image detected under normal conditions (room temperature, atmospheric pressure) is reconstructed by the Python program based on readout signals. Furthermore, a microheater was used to heat the image sensor to 200°C to simulate the harsh heat environment, while a vacuum chamber with circulating liquid nitrogen cooled the device down to –100°C to simulate harsh cold circulation. All aforementioned harsh condition measurements were carried out under 5 × 10⁻² Pa.

SUPPLEMENTAL INFORMATION

Supplemental information can be found online at <https://doi.org/10.1016/j.device.2024.100357>.

ACKNOWLEDGMENTS

The authors acknowledge support from the Material Characterization and Preparation Facility (MCPF) and the State Key Laboratory of Advanced Displays and Optoelectronics Technologies, HKUST. The authors acknowledge the assistance of the Southern University of Science and Technology Core Research Facilities. Z.F. acknowledges support from the New Cornerstone Science Foundation through the XPLOER PRIZE and the Hong Kong Alliance of Technology and Innovation through the BOCHK Science and Technology Innovation Prize. This work was financially supported by the Hong Kong Research Grant Council (16205321, 16309018, and 16214619), the Shenzhen Science and Technology Innovation Commission (JCYJ20170818114107730 and JCYJ20180306174923335), the Innovation and Technology Fund (GHP/014/19SZ), the Guangdong-Hong Kong-Macao Intelligent Micro-Nano Optoelectronic Technology Joint Laboratory (2020B1212030010), and the Foshan Innovative and Entrepreneurial Research Team Program (2018IT100031).

AUTHOR CONTRIBUTIONS

Z.F. and X.Q. conceived the ideas and designed the experiments of this work. X.Q. and Y.D. fabricated the device, integrated the demo system, and reconstructed the images. H.J. and X.Q. carried out the XRD data analysis and refinement. Z.S. and X.Q. contributed to the optical characterizations and sim-

ulations. X.Q., H.J., Y.Z., P.W., B.R., K.Z., Z.L., Y.B.C., B.L., J.W., and Y.L. performed the materials characterizations for perovskite and metal oxide thin films. X.Q., Z.F., Y.Z., S.P., Y.D., Z.L., B.R., Y.B.C., and Z.M. wrote and revised the manuscript. All the authors discussed the results and commented on the manuscript.

DECLARATION OF INTERESTS

We, the authors, have a pending patent related to this work: "Tetrachromatic Perovskite Image Sensor," US patent, application no. 63/587,148, filing date: Oct. 1, 2023.

DECLARATION OF GENERATIVE AI AND AI-ASSISTED TECHNOLOGIES IN THE WRITING PROCESS

During the preparation of this work, the authors used ChatGPT-3.5 Turbo in order to polish the language. After using this tool, the authors reviewed and edited the content as needed and take full responsibility for the content of the publication.

Received: January 17, 2024

Revised: February 26, 2024

Accepted: March 20, 2024

Published: April 16, 2024

REFERENCES

- MORRIS, P. (2012). *Animal Eyes* (Oxford Animal Biology Series) - by Michael F. Land & Dan-Eric Nilsson, 166 (Zool J Linn Soc), p. 912. <https://doi.org/10.1111/j.1096-3642.2012.00849.x>.
- Wilby, D., and Roberts, N.W. (2017). Optical influence of oil droplets on cone photoreceptor sensitivity. *J. Exp. Biol.* 220, 1997–2004. <https://doi.org/10.1242/jeb.152918>.
- Olsson, P., Lind, O., and Kelber, A. (2015). Bird colour vision: Behavioural thresholds reveal receptor noise. *J. Exp. Biol.* 278, 184–193. <https://doi.org/10.1242/jeb.111187>.
- Liu, J., Hu, D., Ni, M., Zou, Y., Gu, Y., Han, Z., Li, J., He, Y., Zhang, Z., and Xu, X. (2022). Monolithic RGB-NIR Perovskite Photodetector for Fused Multispectral Sensing and Imaging. *J. Phys. Chem. Lett.* 13, 3659–3666. <https://doi.org/10.1021/acs.jpcclett.2c00701>.
- Tang, H., Zhang, X., Zhuo, S., Chen, F., Kutulakos, K.N., and Shen, L. (2015). High Resolution Photography with an RGB-Infrared Camera. In 2015 IEEE International Conference on Computational Photography (ICCP) (IEE), pp. 1–10. <https://doi.org/10.1109/ICCPHOT.2015.7168367>.
- Li, G., Xie, D., Zhong, H., Zhang, Z., Fu, X., Zhou, Q., Li, Q., Ni, H., Wang, J., Guo, E.J., et al. (2022). Photo-induced non-volatile VO2 phase transition for neuromorphic ultraviolet sensors. *Nat. Commun.* 13, 1729. <https://doi.org/10.1038/s41467-022-29456-5>.
- Wu, R., Liu, X., Yuan, Y., Wang, Z., Jing, Y., and Sun, J. (2023). Biomimetic Artificial Tetrachromatic Photoreceptors Based on Fully Light-Controlled 2D Transistors. *Adv. Funct. Mater.* 33. <https://doi.org/10.1002/adfm.202305677>.
- Jiang, T., Wang, Y., Zheng, Y., Wang, L., He, X., Li, L., Deng, Y., Dong, H., Tian, H., Geng, Y., et al. (2023). Tetrachromatic vision-inspired neuromorphic sensors with ultraweak ultraviolet detection. *Nat. Commun.* 14, 2281. <https://doi.org/10.1038/s41467-023-37973-0>.
- Zhou, Y., Qiu, X., Wan, Z., Long, Z., Poddar, S., Zhang, Q., Ding, Y., Chan, C.L.J., Zhang, D., Zhou, K., et al. (2022). Halide-exchanged perovskite photodetectors for wearable visible-blind ultraviolet monitoring. *Nano Energy* 100, 107516. <https://doi.org/10.1016/j.nanoen.2022.107516>.
- Zhang, D., Zhu, Y., Jiao, R., Zhou, J., Zhang, Q., Poddar, S., Ren, B., Qiu, X., Cao, B., Zhou, Y., et al. (2023). Metal seeding growth of three-dimensional perovskite nanowire forests for high-performance stretchable photodetectors. *Nano Energy* 111, 108386. <https://doi.org/10.1016/j.nanoen.2023.108386>.

- Hou, Y., Li, J., Yoon, J., Knoepfel, A.M., Yang, D., Zheng, L., Ye, T., Ghosh, S., Priya, S., and Wang, K. (2023). Retina-inspired narrowband perovskite sensor array for panchromatic imaging. *Sci. Adv.* 9, eade2338. <https://doi.org/10.1126/sciadv.ade2338>.
- Wang, Q., Zhang, G., Zhang, H., Duan, Y., Yin, Z., and Huang, Y. (2021). High-Resolution, Flexible, and Full-Color Perovskite Image Photodetector via Electrohydrodynamic Printing of Ionic-Liquid-Based Ink. *Adv. Funct. Mater.* 31, 2100857. <https://doi.org/10.1002/adfm.202100857>.
- Xu, X., Dong, Y., Zhang, Y., Han, Z., Liu, J., Yu, D., Wei, Y., Zou, Y., Huang, B., Chen, J., and Zeng, H. (2022). High-definition colorful perovskite narrowband photodetector array enabled by laser-direct-writing. *Nano Res.* 15, 5476–5482. <https://doi.org/10.1007/s12274-022-4163-3>.
- Tang, X., Ackerman, M.M., Chen, M., and Guyot-Sionnest, P. (2019). Dual-band infrared imaging using stacked colloidal quantum dot photodiodes. *Nat. Photonics* 13, 277–282. <https://doi.org/10.1038/s41566-019-0362-1>.
- Lan, Z., and Zhu, F. (2021). Electrically Switchable Color-Selective Organic Photodetectors for Full-Color Imaging. *ACS Nano* 15, 13674–13682. <https://doi.org/10.1021/acsnano.1c04908>.
- Lan, Z., Lei, Y., Chan, W.K.E., Chen, S., Luo, D., and Zhu, F. (2020). Near-infrared and visible light dual-mode organic photodetectors. *Sci. Adv.* 6, eaaw8065-10. <https://doi.org/10.1126/sciadv.aaw8065>.
- Kosasih, F.U., Erdenebileg, E., Mathews, N., Mhaisalkar, S.G., and Bruno, A. (2022). Thermal evaporation and hybrid deposition of perovskite solar cells and mini-modules. *Joule* 6, 2692–2734. <https://doi.org/10.1016/j.joule.2022.11.004>.
- Li, H., Zhou, J., Tan, L., Li, M., Jiang, C., Wang, S., Zhao, X., Liu, Y., Zhang, Y., Ye, Y., et al. (2022). Sequential vacuum-evaporated perovskite solar cells with more than 24% efficiency. *Sci. Adv.* 8, eabo7422. <https://doi.org/10.1126/sciadv.abo7422>.
- Huang, J., Yuan, Y., Shao, Y., and Yan, Y. (2017). Understanding the physical properties of hybrid perovskites for photovoltaic applications. *Nat. Rev. Mater.* 2, 17042. <https://doi.org/10.1038/natrevmats.2017.42>.
- Kim, W., Kim, H., Yoo, T.J., Lee, J.Y., Jo, J.Y., Lee, B.H., Sasikala, A.A., Jung, G.Y., and Pak, Y. (2022). Perovskite multifunctional logic gates via bipolar photoresponse of single photodetector. *Nat. Commun.* 13, 720. <https://doi.org/10.1038/s41467-022-28374-w>.
- Kim, H., Kim, W., Pak, Y., Yoo, T.J., Lee, H., Lee, B.H., Kwon, S., and Jung, G.Y. (2020). Bias-Modulated Multicolor Discrimination Enabled by an Organic-Inorganic Hybrid Perovskite Photodetector with a p-i-n-i-p Configuration. *Laser Photon. Rev.* 14, 2000305. <https://doi.org/10.1002/lpor.202000305>.
- Malyskin, D., Sereda, V., Ivanov, I., Mazurin, M., Sednev-Lugovets, A., Tsvetkov, D., and Zuev, A. (2020). New phase transition in CsPbBr₃. *Mater. Lett.* 278, 128458. <https://doi.org/10.1016/j.matlet.2020.128458>.
- Haeger, T., Ketterer, M., Bahr, J., Pourdavoud, N., Runkel, M., Heiderhoff, R., and Riedl, T. (2020). Thermal properties of CsPbCl₃ thin films across phase transitions. *J. Phys. Mater.* 3, 024004. <https://doi.org/10.1088/2515-7639/ab749d>.
- Marronnier, A., Roma, G., Boyer-Richard, S., Pedesseau, L., Jancu, J.M., Bonnassieu, Y., Katan, C., Stoumpos, C.C., Kanatzidis, M.G., and Even, J. (2018). Anharmonicity and Disorder in the Black Phases of Cesium Lead Iodide Used for Stable Inorganic Perovskite Solar Cells. *ACS Nano* 12, 3477–3486. <https://doi.org/10.1021/acsnano.8b00267>.
- Steele, J.A., Jin, H., Dovgaliuk, I., Berger, R.F., Braeckvelt, T., Yuan, H., Martin, C., Solano, E., Lejaeghere, K., Rogge, S.M.J., et al. (2019). Thermal nonequilibrium of strained black CsPbI₃ thin films. *Science* 365, 679–684. <https://doi.org/10.1126/science.aax3878>.
- Wright, A.D., Verdi, C., Milot, R.L., Eperon, G.E., Pérez-Osorio, M.A., Snaith, H.J., Giustino, F., Johnston, M.B., and Herz, L.M. (2016). Electron–phonon coupling in hybrid lead halide perovskites. *Nat. Commun.* 7, 0. <https://doi.org/10.1038/ncomms11755>.
- Segall, B., and Mahan, G.D. (1968). Phonon-Assisted Recombination of Free Excitons in Compound Semiconductors. *Phys. Rev.* 171, 935–948. <https://doi.org/10.1103/PhysRev.171.935>.
- Rudin, S., Reinecke, T.L., and Segall, B. (1990). Temperature-dependent exciton linewidths in semiconductors. *Phys. Rev. B* 42, 11218–11231. <https://doi.org/10.1103/PhysRevB.42.11218>.
- Wang, S., Zhao, Q., Hazarika, A., Li, S., Wu, Y., Zhai, Y., Chen, X., Luther, J.M., and Li, G. (2023). Thermal tolerance of perovskite quantum dots dependent on A-site cation and surface ligand. *Nat. Commun.* 14, 2216. <https://doi.org/10.1038/s41467-023-37943-6>.
- Chen, Y., Tan, S., Li, N., Huang, B., Niu, X., Li, L., Sun, M., Zhang, Y., Zhang, X., Zhu, C., et al. (2020). Self-Elimination of Intrinsic Defects Improves the Low-Temperature Performance of Perovskite Photovoltaics. *Joule* 4, 1961–1976. <https://doi.org/10.1016/j.joule.2020.07.006>.
- Afshari, H., Sourabh, S., Chacon, S.A., Whiteside, V.R., Penner, R.C., Rout, B., Kirmani, A.R., Luther, J.M., Eperon, G.E., and Sellers, I.R. (2023). FACsPb Triple Halide Perovskite Solar Cells with Thermal Operation over 200 °C. *ACS Energy Lett.* 8, 2408–2413. <https://doi.org/10.1021/acsenerylett.3c00551>.
- Li, G., Su, Z., Li, M., Lee, H.K.H., Datt, R., Hughes, D., Wang, C., Flatken, M., Köbler, H., Jerónimo-Rendon, J.J., et al. (2022). Structure and Performance Evolution of Perovskite Solar Cells under Extreme Temperatures. *Adv. Energy Mater.* 12, 1–7. <https://doi.org/10.1002/aenm.202202887>.
- Dong, Z., Li, W., Wang, H., Jiang, X., Liu, H., Zhu, L., and Chen, H. (2021). High-Temperature Perovskite Solar Cells. *Sol. RRL* 5, 2100370. <https://doi.org/10.1002/solr.202100370>.
- Li, G., Su, Z., Canil, L., Hughes, D., Aldamasy, M.H., Dagar, J., Trofimov, S., Wang, L., Zuo, W., Jerónimo-Rendon, J.J., et al. (2023). Highly efficient p-i-n perovskite solar cells that endure temperature variations. *Science* 379, 399–403. <https://doi.org/10.1126/science.add7331>.
- Saparov, B., and Mitzi, D.B. (2016). Organic-Inorganic Perovskites: Structural Versatility for Functional Materials Design. *Chem. Rev.* 116, 4558–4596. <https://doi.org/10.1021/acs.chemrev.5b00715>.
- Huang, J., Wang, H., Jia, C., Tang, Y., Yang, H., Chen, C., Gou, K., Zhou, Y., Zhang, D., and Liu, S. (2024). Advances in Crystallization Regulation and Defect Suppression Strategies for All-inorganic CsPbX₃ Perovskite Solar Cells. *Prog. Mater. Sci.* 141, 101223. <https://doi.org/10.1016/j.pmatsci.2023.101223>.
- Zhu, H., Ding, G., Liu, X., Huang, H., Chen, B., McGehee, M.D., Sargent, E.H., and Bakr, O.M. (2023). Long-term operating stability in perovskite photovoltaics. *J. Diabetes* 15, 569–582. <https://doi.org/10.1038/s41578-023-00582-w>.
- Muscarella, L.A., and Ehrler, B. (2022). The influence of strain on phase stability in mixed-halide perovskites. *Joule* 6, 2016–2031. <https://doi.org/10.1016/j.joule.2022.07.005>.
- Gu, L., Poddar, S., Lin, Y., Long, Z., Zhang, D., Zhang, Q., Shu, L., Qiu, X., Kam, M., Javey, A., and Fan, Z. (2020). A biomimetic eye with a hemispherical perovskite nanowire array retina. *Nature* 581, 278–282. <https://doi.org/10.1038/s41586-020-2285-x>.
- Ding, Y., Liu, G., Long, Z., Zhou, Y., Qiu, X., Ren, B., Zhang, Q., Chi, C., Wan, Z., Huang, B., and Fan, Z. (2022). Uncooled self-powered hemispherical biomimetic pit organ for mid- to long-infrared imaging. *Sci. Adv.* 8, eabq8432-8. <https://doi.org/10.1126/sciadv.abq8432>.

DEVICE, Volume 2

Supplemental information

A tetrachromatic sensor for imaging beyond the visible spectrum in harsh conditions

Xiao Qiu, Yucheng Ding, Zhibo Sun, Haocheng Ji, Yu Zhou, Zhenghao Long, Gongze Liu, Peiyao Wang, Swapnadeep Poddar, Beita Ren, Kemeng Zhou, Ziyun Li, Yang Bryan Cao, Zichao Ma, Baikui Li, Yuanjing Lin, Baoling Huang, Jiannong Wang, Hoi Sing Kwok, and Zhiyong Fan

Table of Content

Note S1 Fabrication process

Note S2 Light discrimination

Fig. S1 Refractive index (n) and extinction coefficient (k) of CsPbCl₃, CsPbClBr₂, CsPbBr₃, and CsPbBrI₂ thin films

Fig. S2 Transmittance simulation within the depth of CsPbCl₃, CsPbClBr₂, CsPbBr₃, and CsPbBrI₂ thin films

Fig. S3 Simulation of optical crosstalk with a function of light incidence angle (θ) and quartz thickness (d)

Fig. S4 UV-Vis spectra of CsPbCl₃, CsPbClBr₂, CsPbBr₃, CsPbBrI₂ thin films, and quartz

Fig. S5 SEM images of four materials and device

Fig. S6 AFM topography images and RMS surface roughness of perovskite films

Fig. S7 XPS spectra of perovskite thin films

Fig. S8 XRD spectra of (a) CsPbCl₃, (b) CsPbClBr₂, (c) CsPbBr₃, and (d) CsPbBrI₂ thin films under ambient conditions

Fig. S9 XRD spectra of CsPbCl₃ and CsPbClBr₂ thin films before and after annealing

Fig. S10 XRD spectra of CsPbBr₃ and CsPbBrI₂ thin films before and after annealing

Fig. S11 AFM topography images and RMS surface roughness of SnO₂ (a) and NiO (b) films

Fig. S12 Fabrication process of the tetrachromatic perovskite imaging sensor

Fig. S13 A designed copper chamber for double sides perovskite thin films annealing

Fig. S14 Illustration of sequential evaporated metal halide layers before annealing

Fig. S15 UPS spectra of the secondary cutoff region and the Fermi level region of SnO₂ and NiO thin film

Fig. S16 Illustration of working mechanism of tetrachromatic image sensor

Fig. S17 Detectivity of CsPbCl₃, CsPbClBr₂, CsPbBr₃, and CsPbBrI₂ thin films under as a function of wavelength

Fig. S18 Current density as a function of light intensity curves of the tetrachromatic perovskite imaging sensor

Fig. S19 Response time of four photo active layers

Fig. S20 TD-XRD spectra of perovskite thin films

Fig. S21 Enlarged TD-XRD contour map of (100) and (200) planes of perovskite thin films

Fig. S22 Phase transition with the temperature evolution of perovskite thin films from TD-XRD spectra

Fig. S23 Normalized anisotropic lattice constants and volumes of four materials with respect to temperature

Fig. S24 The TD-PL intensity and FWHM of perovskite thin films

Fig. S25 Temperature dependent normalized responsivity of tetrachromatic image sensor

Fig. S26 Pressure dependent normalized responsivity

Fig. S27 Stability of devices with the simulated extravehicular thermal shock cycling test

Fig. S28 Photoresponse of CsPbBr₃ layer (blue sensor) working under a cryogenic environment of 16 K

Fig. S29 Long-time device stability under continuous light soaking in a vacuum at 500 K

Fig. S30 Shelf stability of unencapsulated device under ambient storage (a) and vacuum (b) conditions

Fig. S31-Fig. S32 Long-time operational device stability under continuous light soaking in a vacuum

Fig. S33 SEM images of four materials before and after 100h annealing at 200 °C

Fig. S34 XRD spectra of miscellaneous of CsPbBr₂ perovskite thin films and halide vacancy proportion of each perovskite thin film compared with the films before annealing

Fig. S35 UV channel demonstration

Fig. S36 RGB channels w/wo temperature coefficient correction under the vacuum, low-, and high-temperature environments

Fig. S37 Illustration of imaging setup

Fig. S38 Schematic diagram of signal-connecting circuits

Fig. S39 Configuration for PCB design

Fig. S40 Photograph of tetrachromatic image sensor and single layer perovskite thin films

Fig. S41 Benchmark of the perovskite photodetectors' responsivity with a function of light intensity

Table S1 Comparison of the device performance between the tetrachromatic perovskite imaging sensor and other reported perovskite-based photodetectors

Note S1, Fabrication process

A 20 nm thick NiO film was sputtered on both sides of patterned ITO-coated substrates, as illustrated in Fig. S12. The plates were annealed under a protective atmosphere at 350 °C for 15 min, then taken into a vacuum evaporator to deposit the metal halides. PbX₂ and CsX were sequentially deposited by thermal evaporation layer by layer, as described in Fig. S14. CsPbClBr₂ and CsPbBr₃ layers were initially evaporated on both sides, followed by annealing at 280 °C in ambient atmosphere for 2 min on the hotplate (directly put the sample on the hotplate for 2 min), and then annealing on the hotplate in the glovebox with protective atmosphere for 10 min at the same temperature. The metal chamber designed for double-side annealing is displayed in Fig. S13, which facilitated uniform heat transfer, resulting in a high-crystalline thin film. The metal chambers were heated to the target temperature before setting the sample. After two 18 nm SnO₂ layers were sputtered on both sides, the CsPbCl₃ layer was prepared with the same method mentioned before on the top of the CsPbClBr₂ layer. Subsequently, a 20 nm thick NiO and 120 nm thick ITO layer were generated by magnetron sputtering. Finally, CsPbBrI₂, NiO and ITO layers were then prepared. Notably, all transfer processes were protected with the nitrogen gas, except for the ambient annealing process. The thermal evaporation processes were started at 5×10⁻³ Pa, while the sputtering process was started at 5×10⁻⁴ Pa. A designated thickness perovskite film is fabricated with a constant deposition rate of 1.0 Å/s.

Note S2, Light discrimination

Colour reconstruction and discrimination methods applied for perovskite image sensors are almost based on the CIE 1931 XYZ colour space that is based on a series of experiments on the human vision system^{S1,S2}. Due to the avian vision system based tetrachromatic image sensor carried out with four photoactive layers, including a UV detection layer, it is not easy to describe colours in traditional colour space and the display. We directly used 4D and 3D light intensity discrimination measurements to estimate the colour discrimination capabilities of our device (Fig. 4). The dots' position shown in 3D tetrahedral and ternary images are calculated as follows:

$$L_X \propto I_X^{\alpha_X} \cdot \mu_X$$

$$R_X = \frac{L_X}{L_{UV} + L_B + L_G + L_R}$$

Where X represents UV, B, G, R light, L_X is the calculated light intensity, I_X is the measured, α_X is the measured exponential coefficient, μ_X is the measured temperature-dependent coefficient, R_X is the calculated light intensity ratio.

To evaluate the deviation of detected light intensity, we calculated distance (D) as follows:

$$D = \sqrt{(R_{UV} - R_{UV0})^2 + (R_B - R_{B0})^2 + (R_G - R_{G0})^2 + (R_R - R_{R0})^2}$$

Where R_{X0} is the original ratio of light intensity.

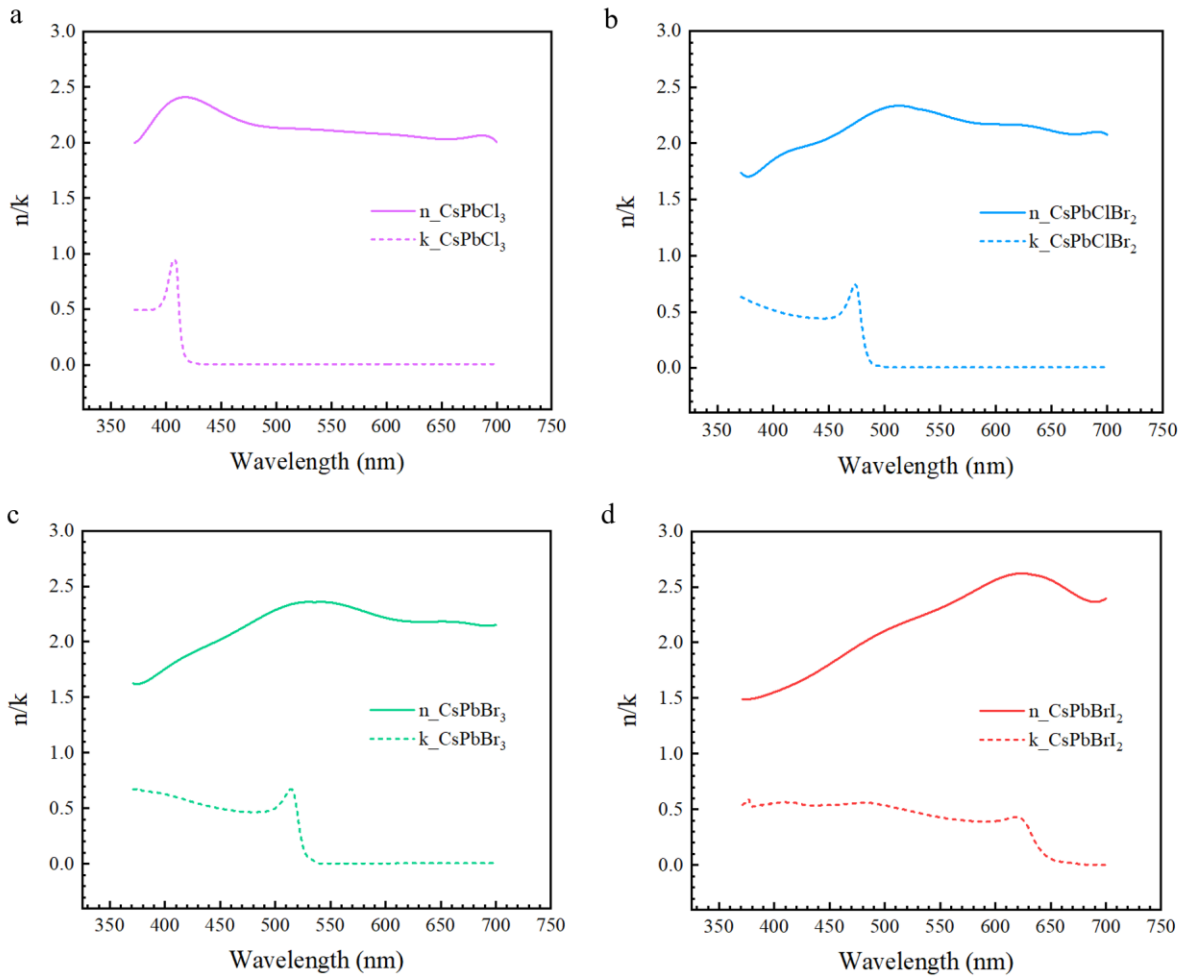


Fig. S1 Refractive index (n) and extinction coefficient (k) of CsPbCl₃, CsPbClBr₂, CsPbBr₃, and CsPbBrI₂ thin films. The n, k values are derived from UV-vis spectra and ellipsometer characterization.

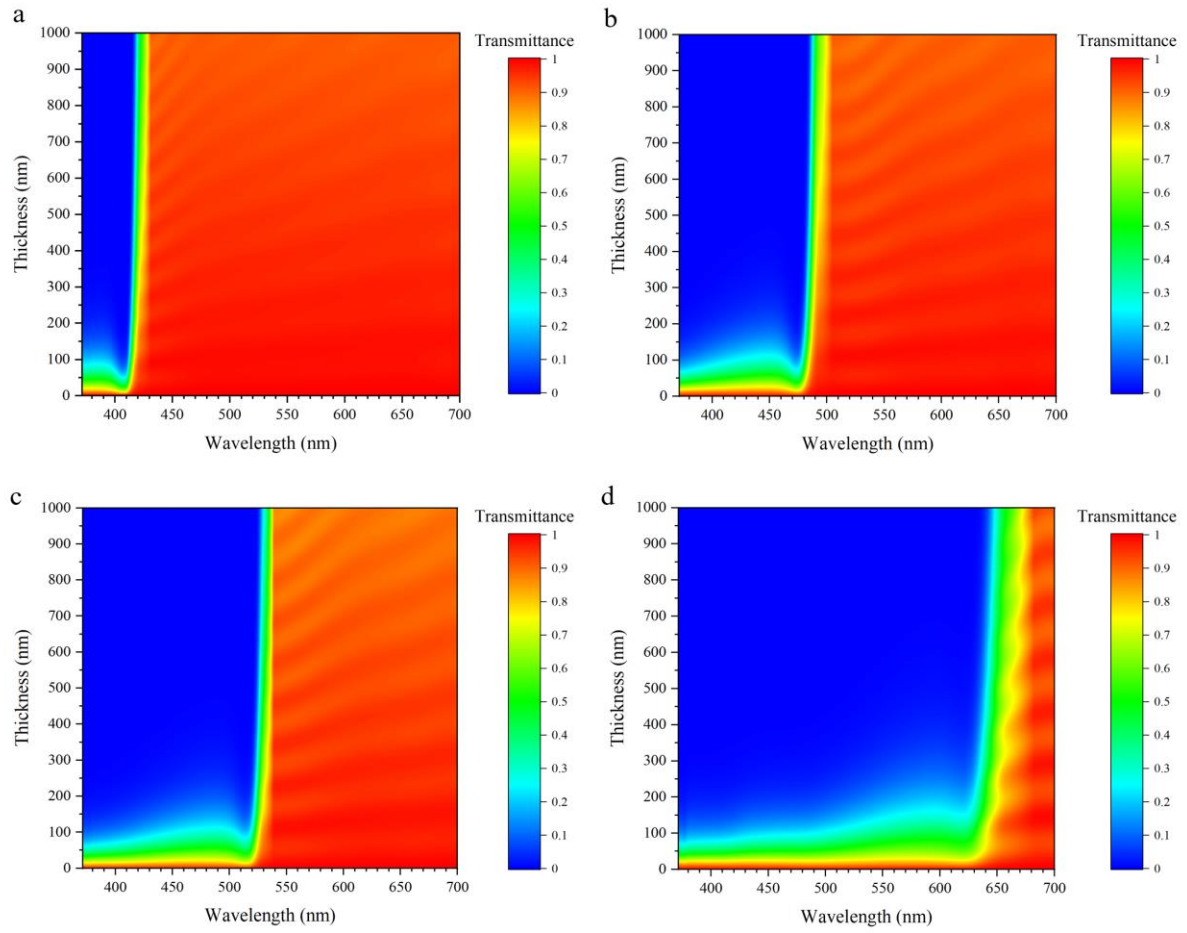


Fig. S2 Transmittance simulation within the depth of CsPbCl_3 , CsPbClBr_2 , CsPbBr_3 , and

CsPbBr_2 thin films.

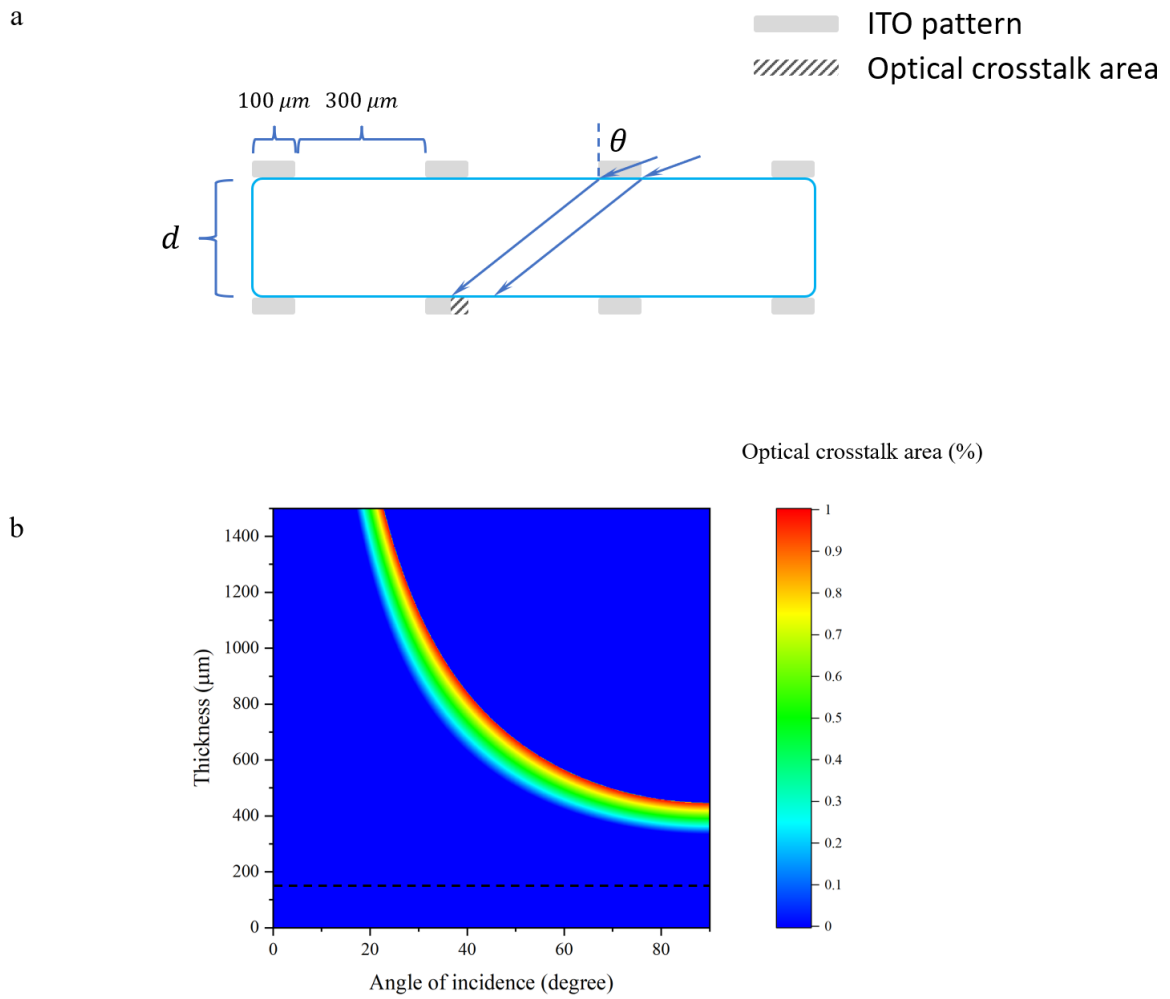


Fig. S3 Simulation of optical crosstalk with a function of light incidence angle (θ) and quartz thickness (d). **a**, Illustration of simulation model of optical crosstalk. The electrode linewidth and pixel pitch are 100 μm and 400 μm , respectively. The dashed area is the crosstalk area of adjacent pixel. **b**, Contour map of optical crosstalk simulation, and we chose 150 μm quartz to avoid optical crosstalk (dash line).

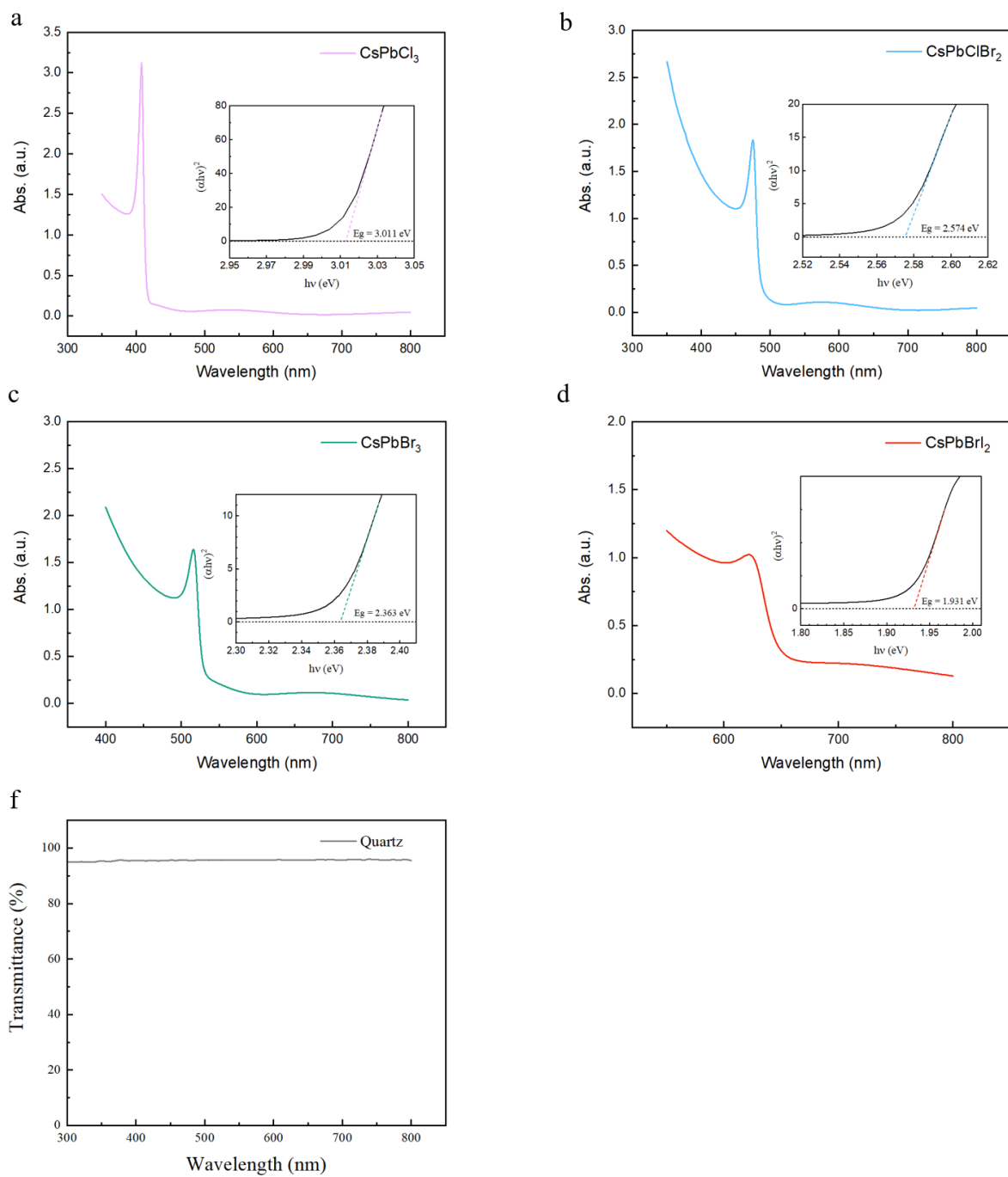


Fig. S4 UV-Vis spectra of CsPbCl₃, CsPbClBr₂, CsPbBr₃, CsPbBrI₂ thin films, and quartz. The

insert figures are the Tauc plots for estimating each direct band gap.

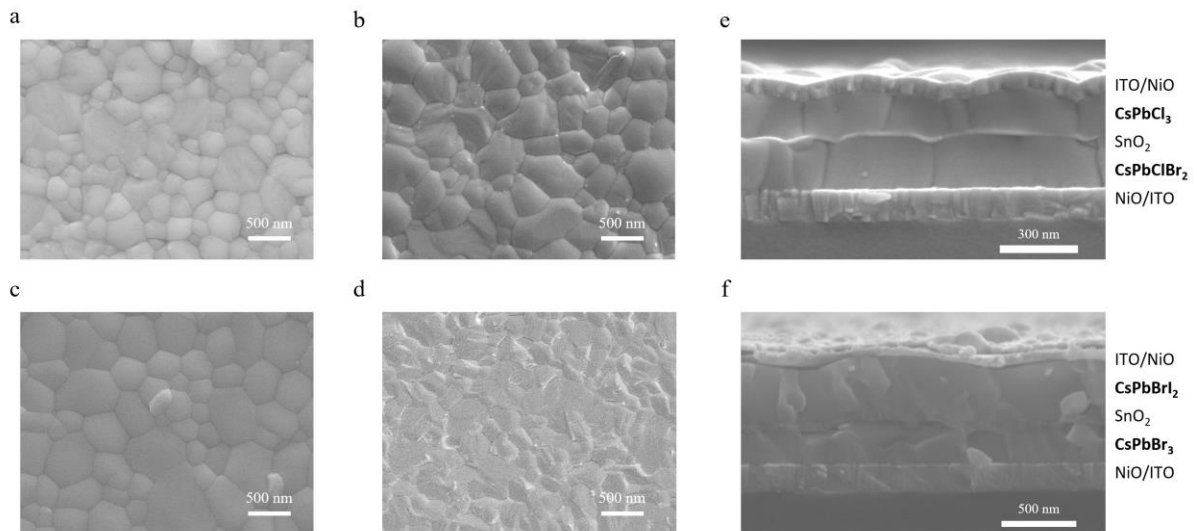


Fig. S5 SEM images of four materials and device. **a-d**, Top view of CsPbCl₃, CsPbClBr₂, CsPbBr₃, and CsPbBr₂ thin films, respectively. **e**, Cross-section of ITO/NiO/CsPbCl₃/SnO₂/CsPbClBr₂/NiO/ITO layers and **(f)** ITO/NiO/CsPbBr₃/SnO₂/CsPbBr₂/NiO/ITO layers. The photograph of the tetrachromatic image sensor and single-layer perovskite thin films are shown in Fig. S40.

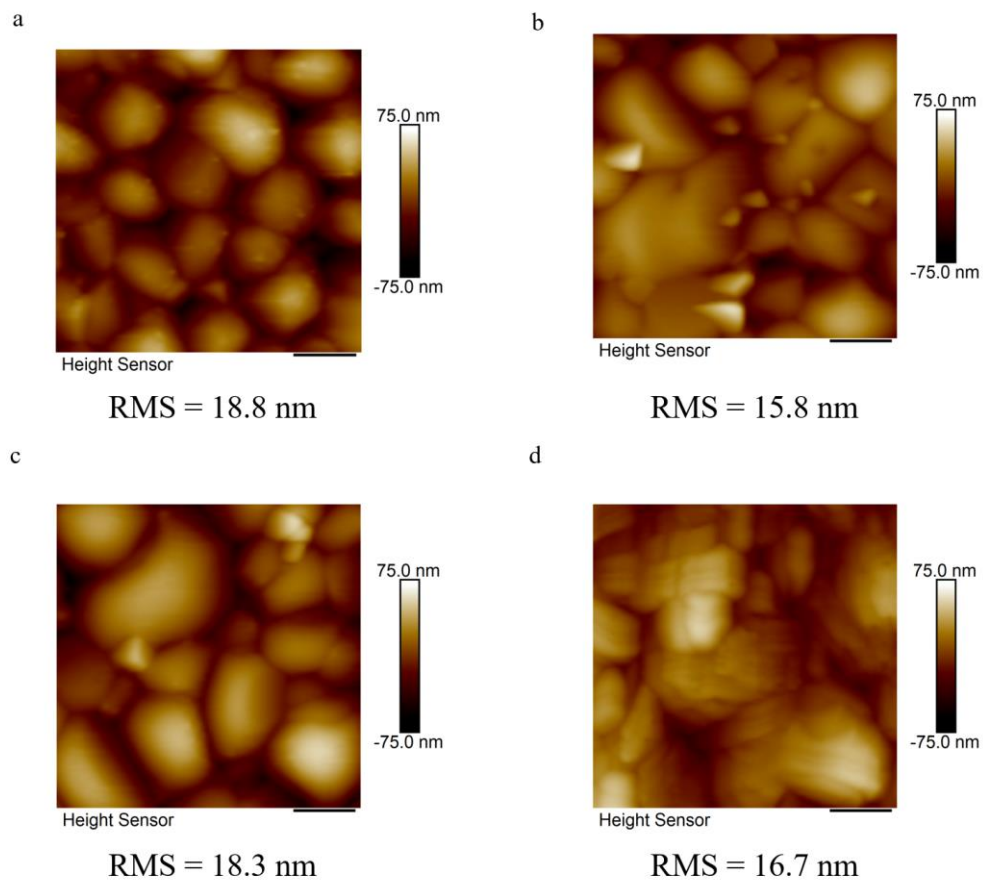


Fig. S6 AFM topography images and RMS surface roughness of perovskite films. a, CsPbCl_3 . b, CsPbClBr_2 . c, CsPbBr_3 . d, CsPbBrI_2 .

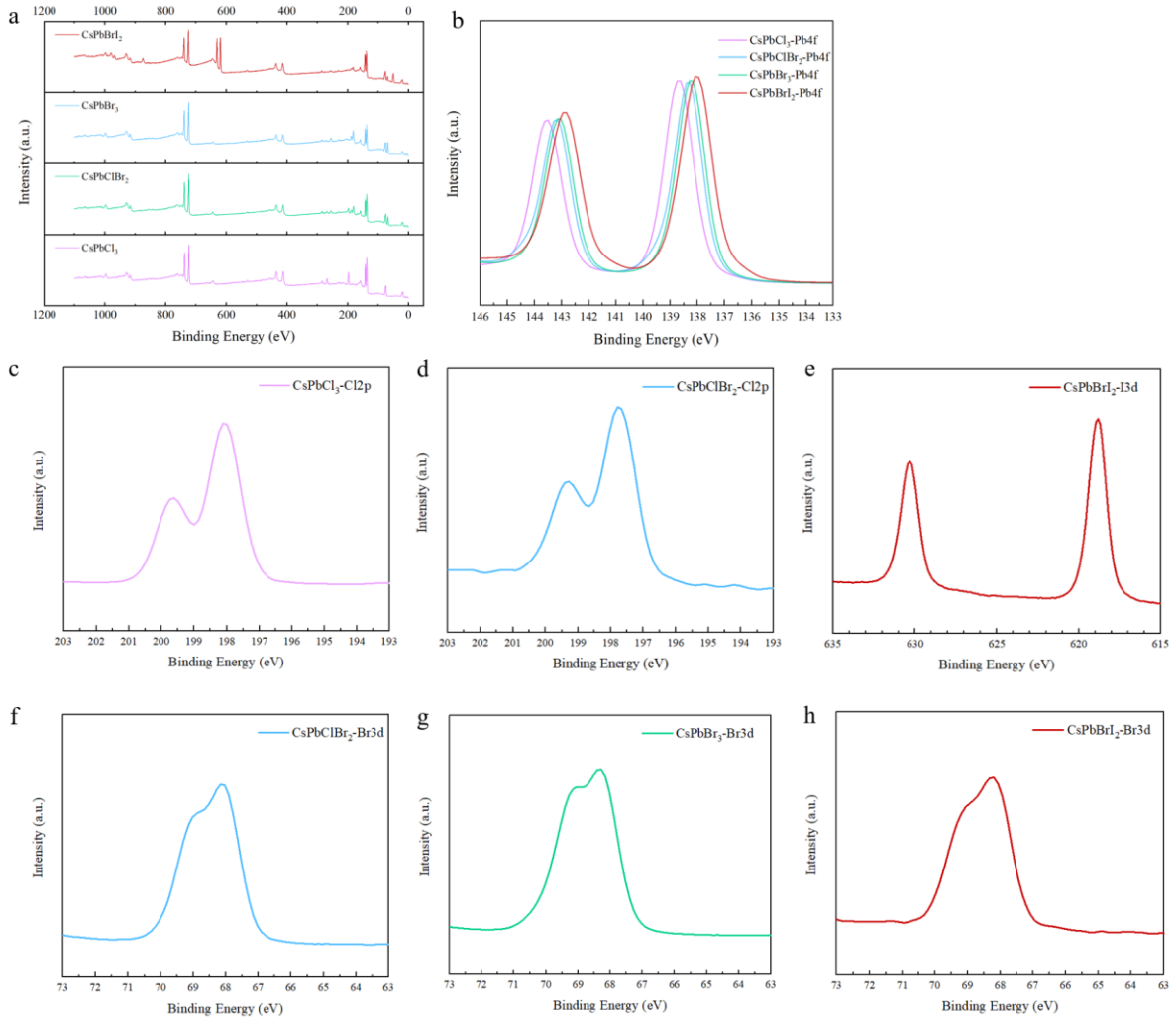


Fig. S7 XPS spectra of perovskite thin films. a, Full spectra of CsPbCl₃, CsPbClBr₂, CsPbBr₃, and CsPbBr₂ thin film. **b**, Pb 4f_{5/2} and 4f_{7/2}, Cl 3d of CsPbCl₃ (**c**) and CsPbClBr₂ (**d**). **e**, I 3d_{3/2} and 3d_{5/2}, Br 3d of CsPbClBr₂ (**f**), CsPbBr₃ (**g**), and CsPbBr₂ (**h**).

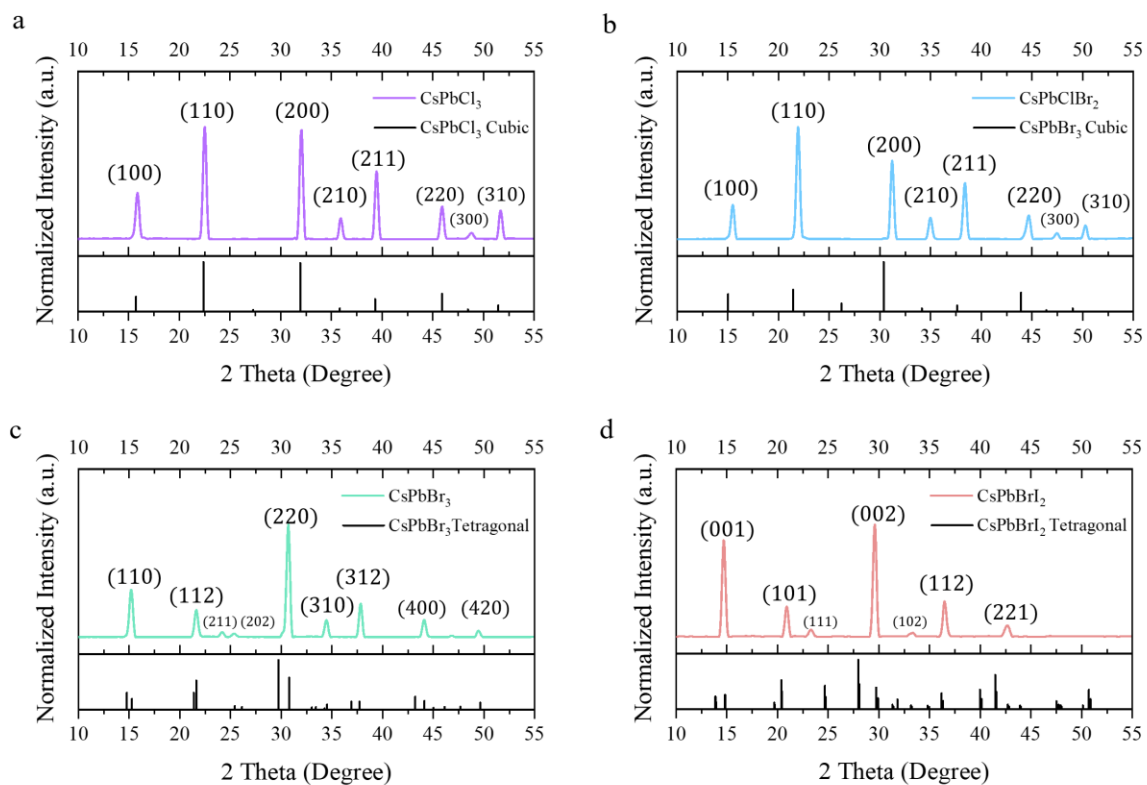


Fig. S8 XRD spectra of (a) CsPbCl₃, (b) CsPbClBr₂, (c) CsPbBr₃, and (d) CsPbBrI₂ thin films under

ambient conditions. An apparent peak shifting is observed when heavier halide atoms substitute X

sites. To determine the appropriate perovskite structure, we utilized VESTA software to calculate the

theoretical diffraction pattern based on the CIF source obtained from The Materials Project. Given the

limited availability of CsPbClBr₂ structural sources, we substituted it with the cubic CsPbBr₃ source for

our analysis. Materials ID: CsPbCl₃ cubic (mp-23037), CsPbBr₃ cubic (mp-600089), CsPbBr₃ tetragonal

(mp-1014168), CsPbBrI₂ (mp-2646981).

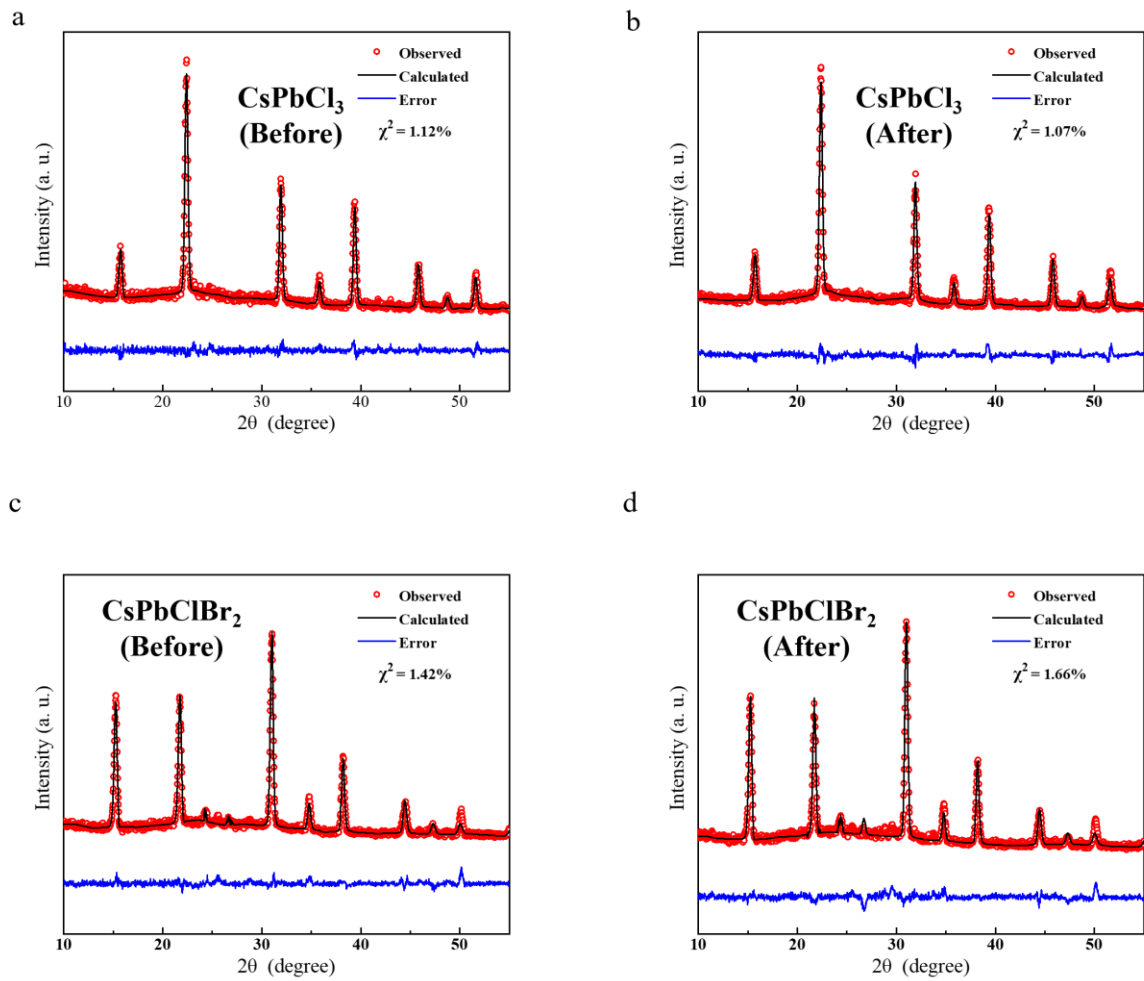


Fig. S9 XRD spectra of perovskite thin films before and after annealing. CsPbCl₃ (a) and CsPbClBr₂ (c) before annealing. CsPbCl₃ (b) and CsPbClBr₂ (d) after 100 h annealing at 200 °C. The experiment was conducted within a glovebox under a nitrogen atmosphere for protection. The sample was placed on a 200 °C hotplate for heating and subsequently cooled on a room temperature steel plate directly.

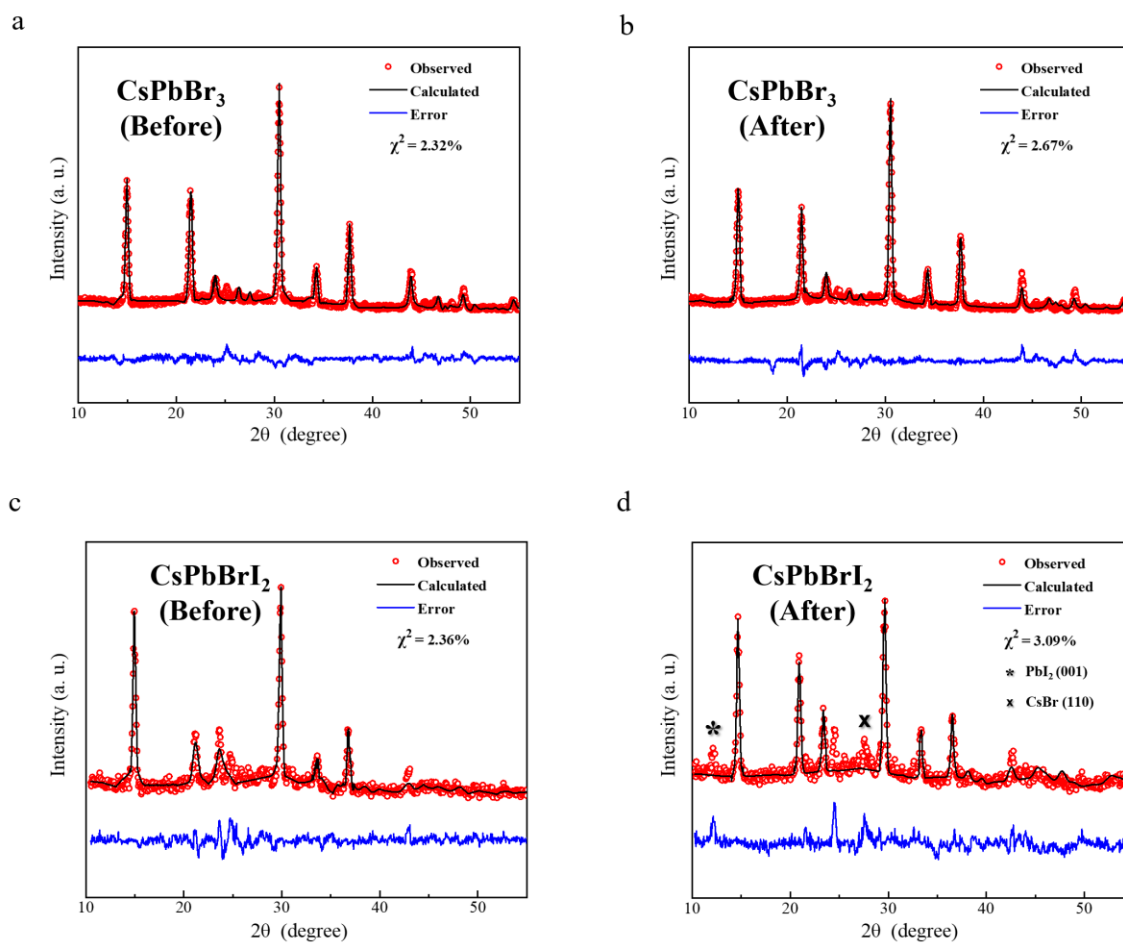


Fig. S10 XRD spectra of perovskite thin films before and after annealing. CsPbBr₃ (a) and CsPbBrI₂

(c) before annealing. CsPbCl₃ (b) and CsPbClBr₂ (d) after 100 h annealing at 200 °C. The experiment

process is same as Fig. S9.

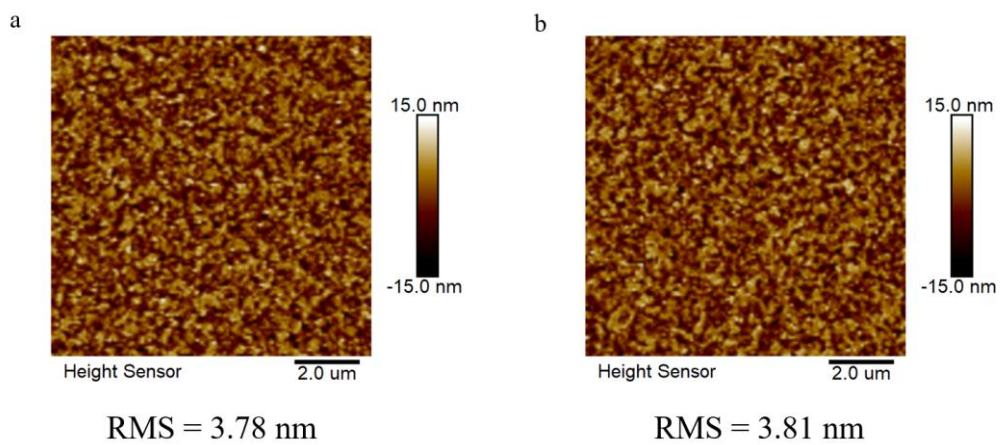


Fig. S11 AFM topography images and RMS surface roughness of SnO₂ (a) and NiO (b) films.

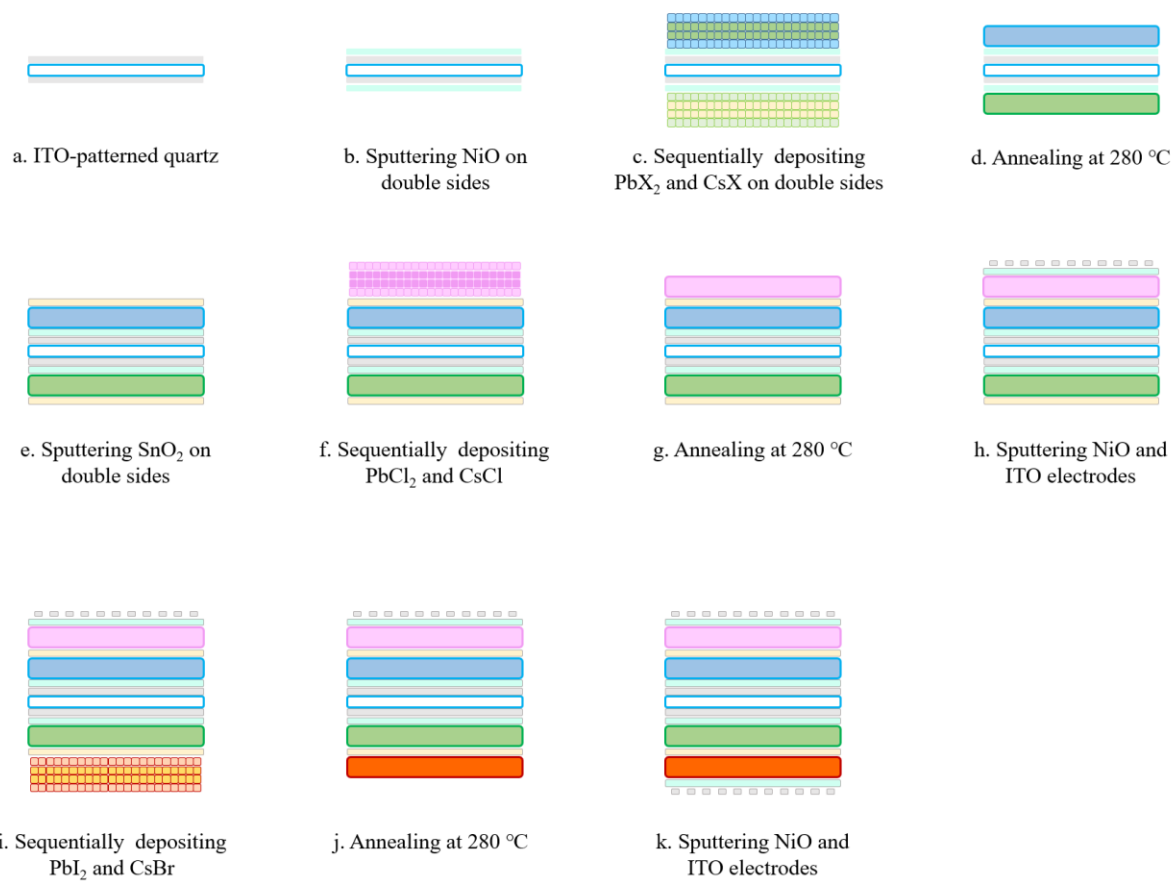


Fig. S12 Fabrication process of the tetrachromatic perovskite imaging sensor. The photograph of

the tetrachromatic image sensor and single-layer perovskite thin films are shown in Fig. S40.

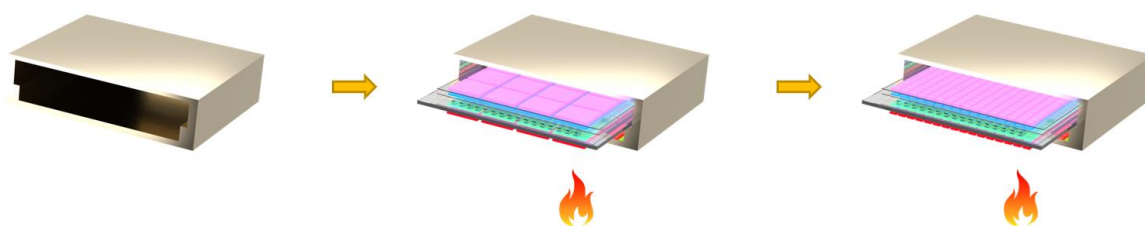


Fig. S13 A designed copper chamber for double sides perovskite thin films annealing.

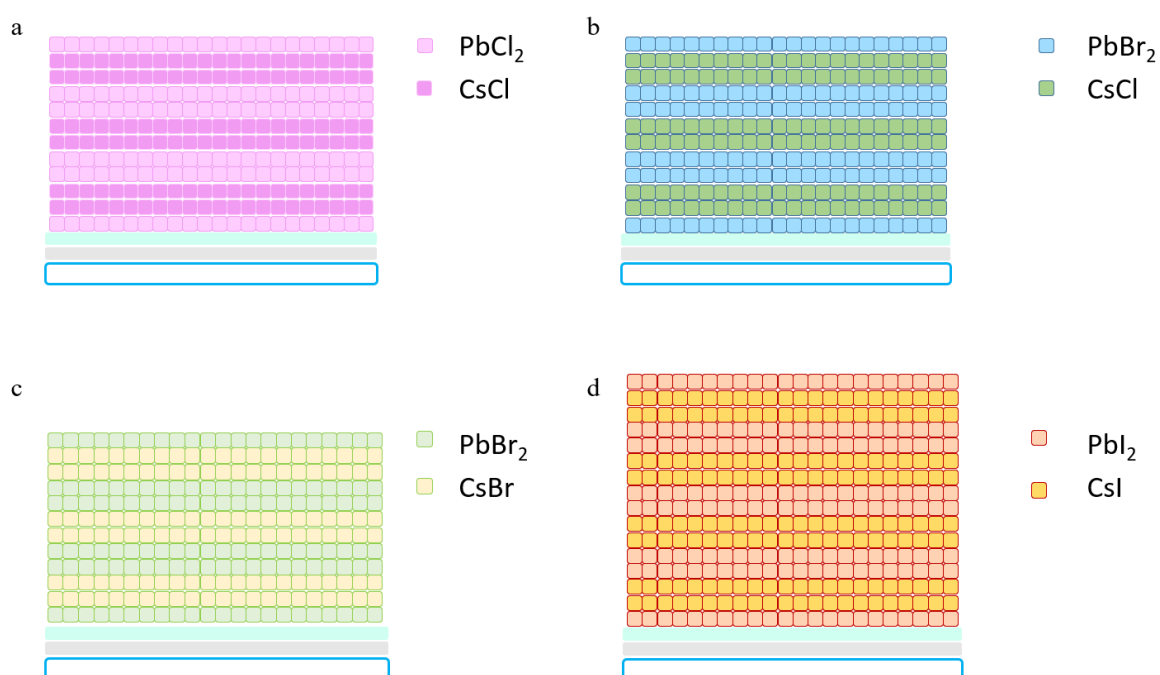


Fig. S14 Illustration of sequential evaporated metal halide layers before annealing. **a-c**, One-sixth stoichiometric PbX_2 evaporate on the first and last layers while other layers are one-third stoichiometric amounts of total CsX or PbX_2 . **d**, One-eighth stoichiometric PbI_2 evaporate on the first and last layer while other layers are one-fourth stoichiometric amounts of total CsBr or PbI_2 due to the total CsPbBrI_2 film being thicker than the other three. The total thickness of each layer after annealing is 200 nm, 300 nm, 320 nm, and 350 nm, separately.

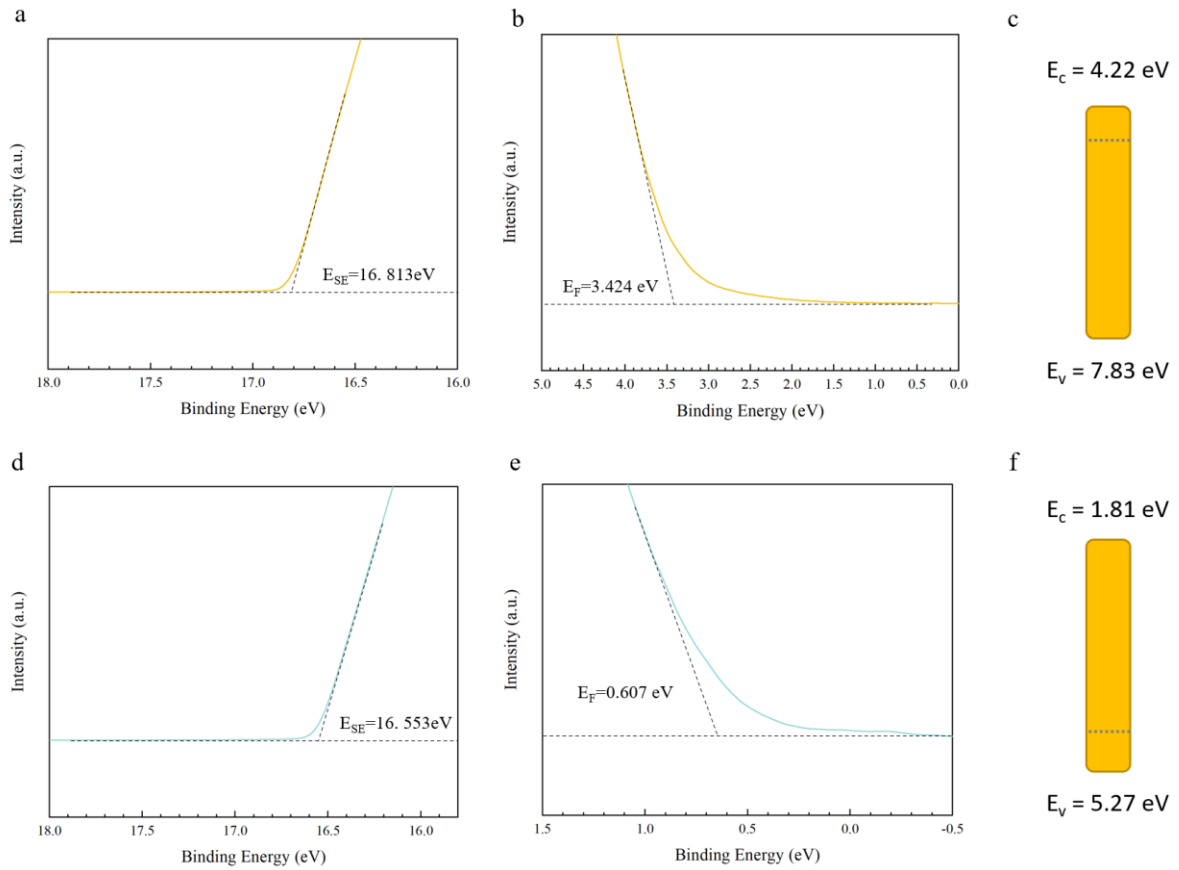


Fig. S15 UPS spectra of the secondary cutoff region and the Fermi level region of SnO₂ and NiO

thin film. E_{SE} (a, d), E_F (b, e), and estimated energy level (c, f) of SnO₂ and NiO, respectively. Energy

level of the valence band maximum (E_V) can be calculated by the equation: $\Phi = h\nu - (E_{SE} - E_F)$, where

$h\nu = 21.22$ eV. E_V of SnO₂ and NiO is 7.83 eV and 5.27 eV. Energy level of the conduction band

minimum (E_C) is defined by: $E_C = E_V + E_g$. E_C of SnO₂ and NiO is 4.22 eV and 1.81 eV.

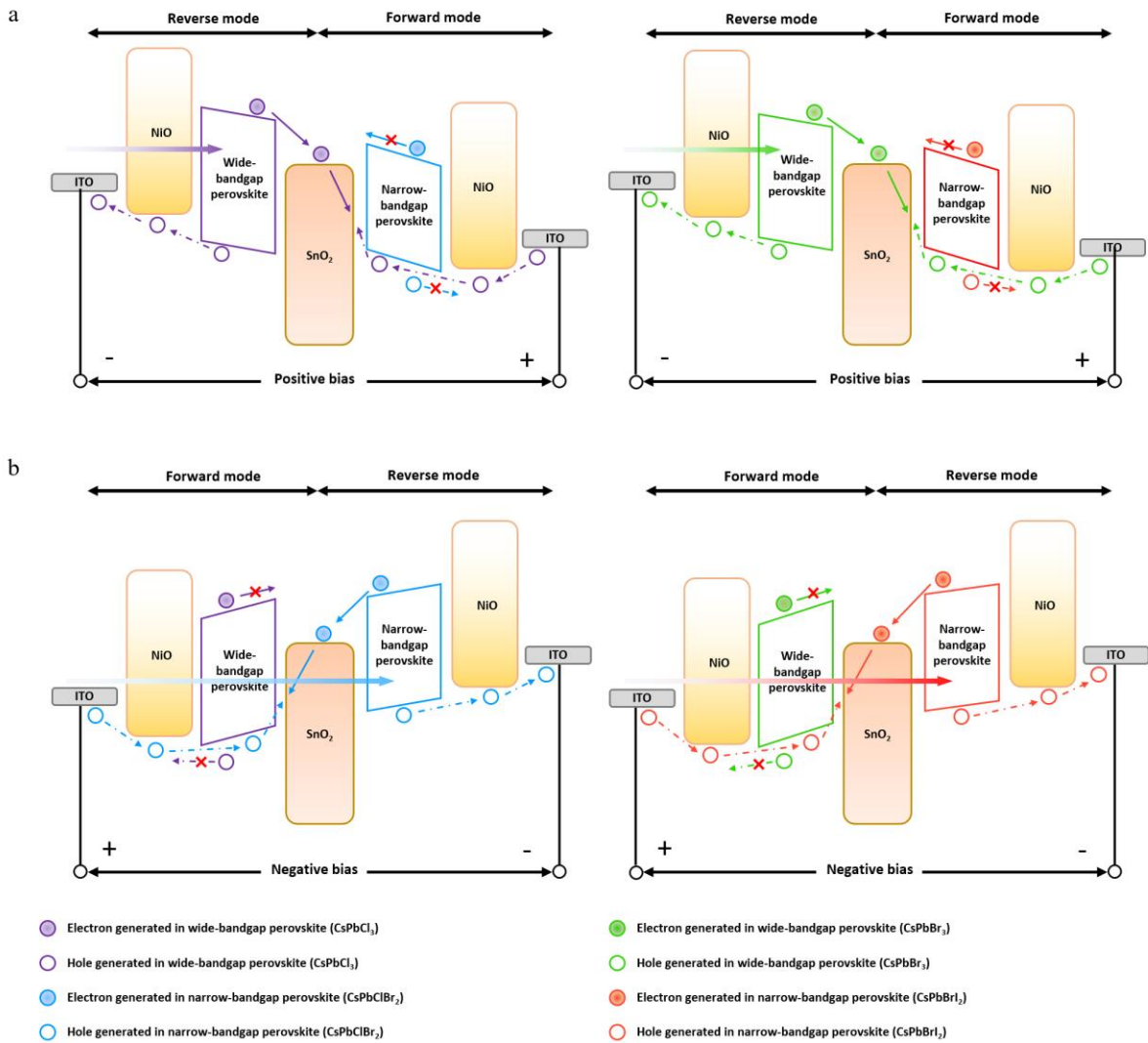


Fig. S16 Illustration of working mechanism of tetrachromatic image sensor. a, Tetrachromatic device is under positive bias, responding to UV and green light. **b,** Tetrachromatic device is under negative bias, responding to blue and red light.

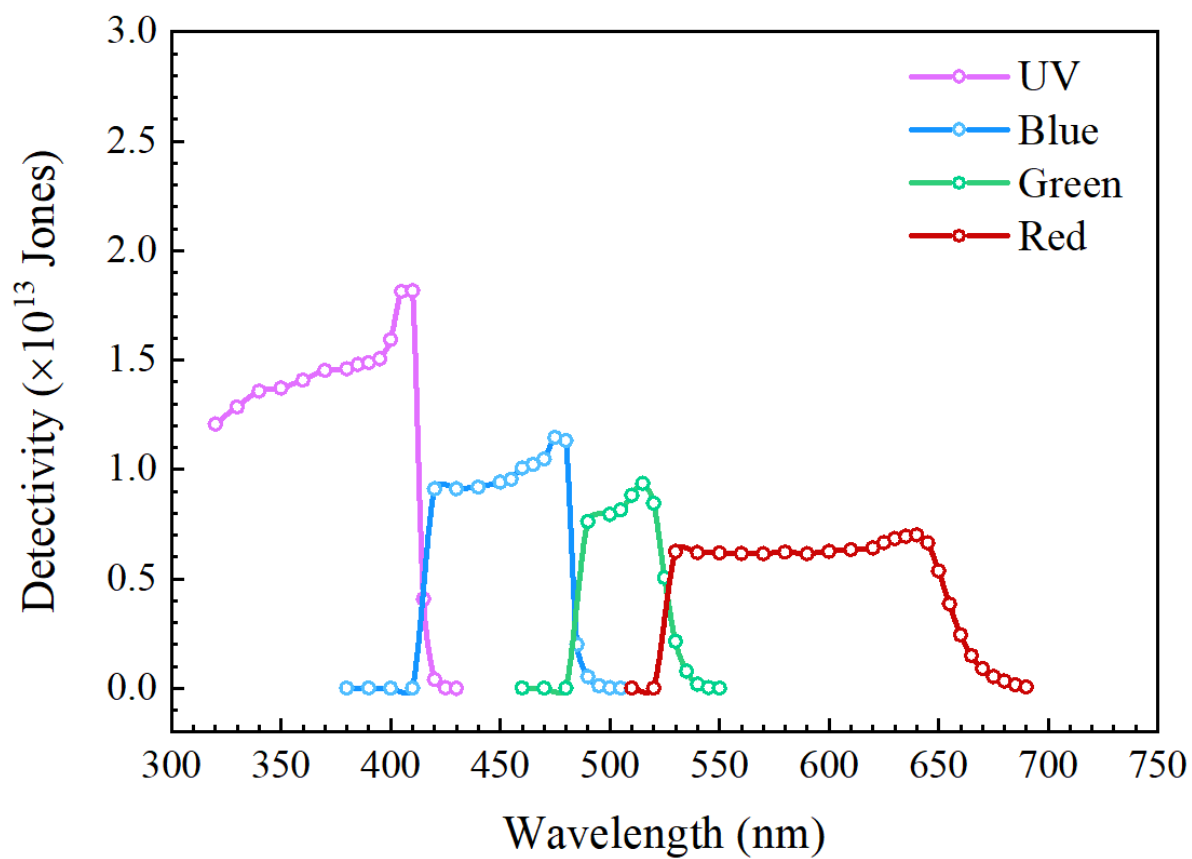


Fig. S17 Detectivity of CsPbCl₃, CsPbClBr₂, CsPbBr₃, and CsPbBrI₂ thin films under as a function of wavelength. The tests are under 405 nm, 450 nm, 520 nm, and 635 nm light sources, respectively.

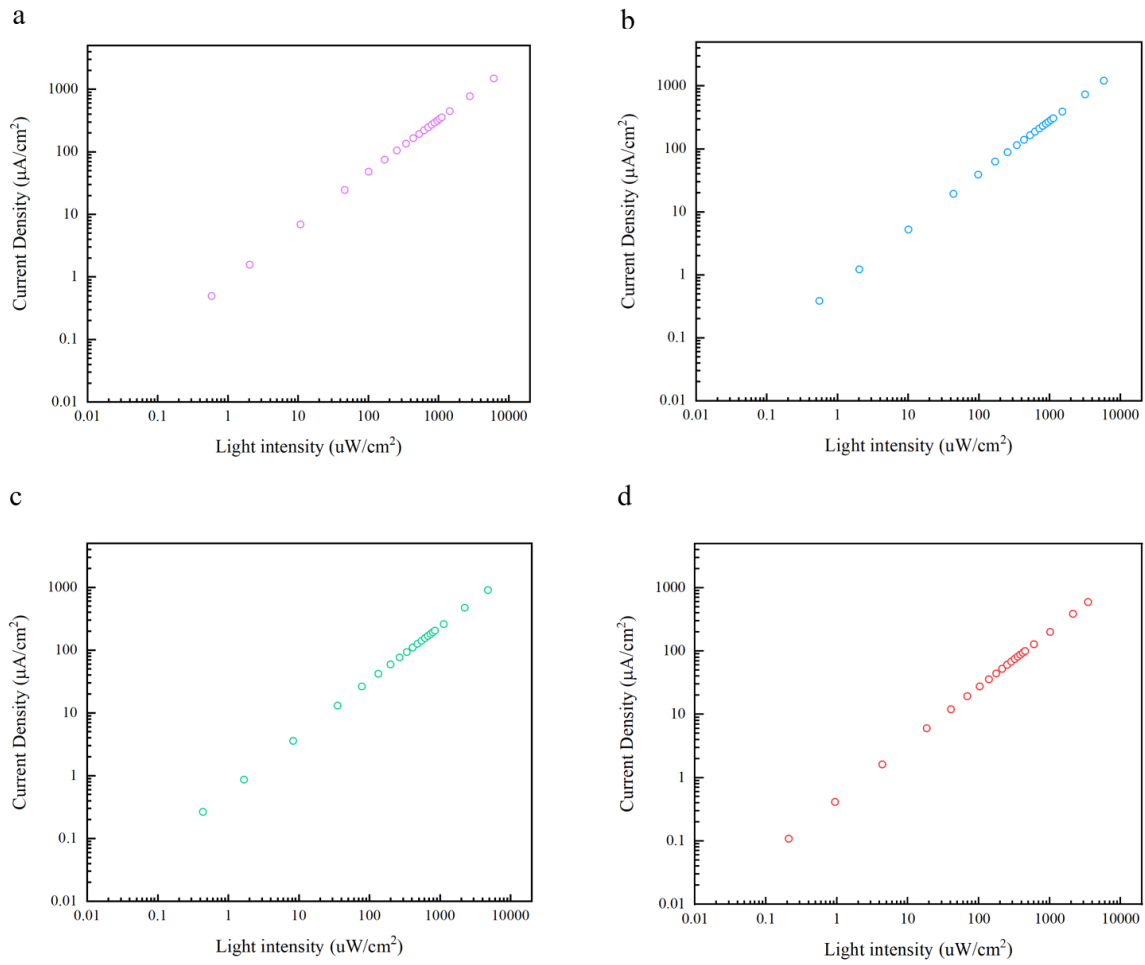


Fig. S18 Current density as a function of light intensity curves of the tetrachromatic perovskite

imaging sensor. a, CsPbCl_3 . b, CsPbClBr_2 . c, CsPbBr_3 . d, CsPbBrI_2 . The tests are under 405 nm, 450

nm, 520 nm, and 635 nm light sources, respectively.

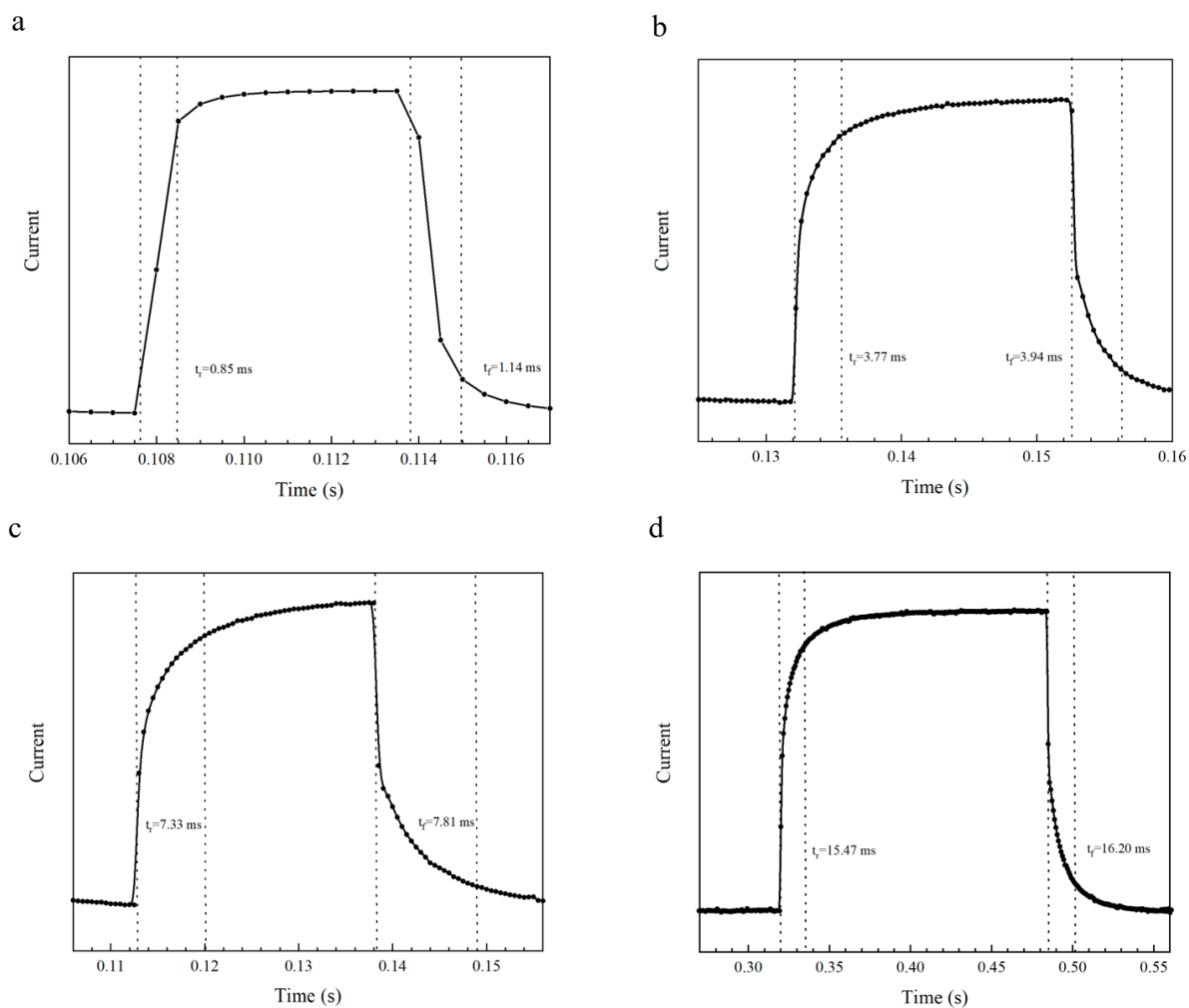


Fig. S19 Response time of four photo active layers. a, CsPbCl_3 . b, CsPbClBr_2 . c, CsPbBr_3 . d,

CsPbBr_2 . The tests are under 405 nm, 450 nm, 520 nm, and 635 nm light sources, respectively.

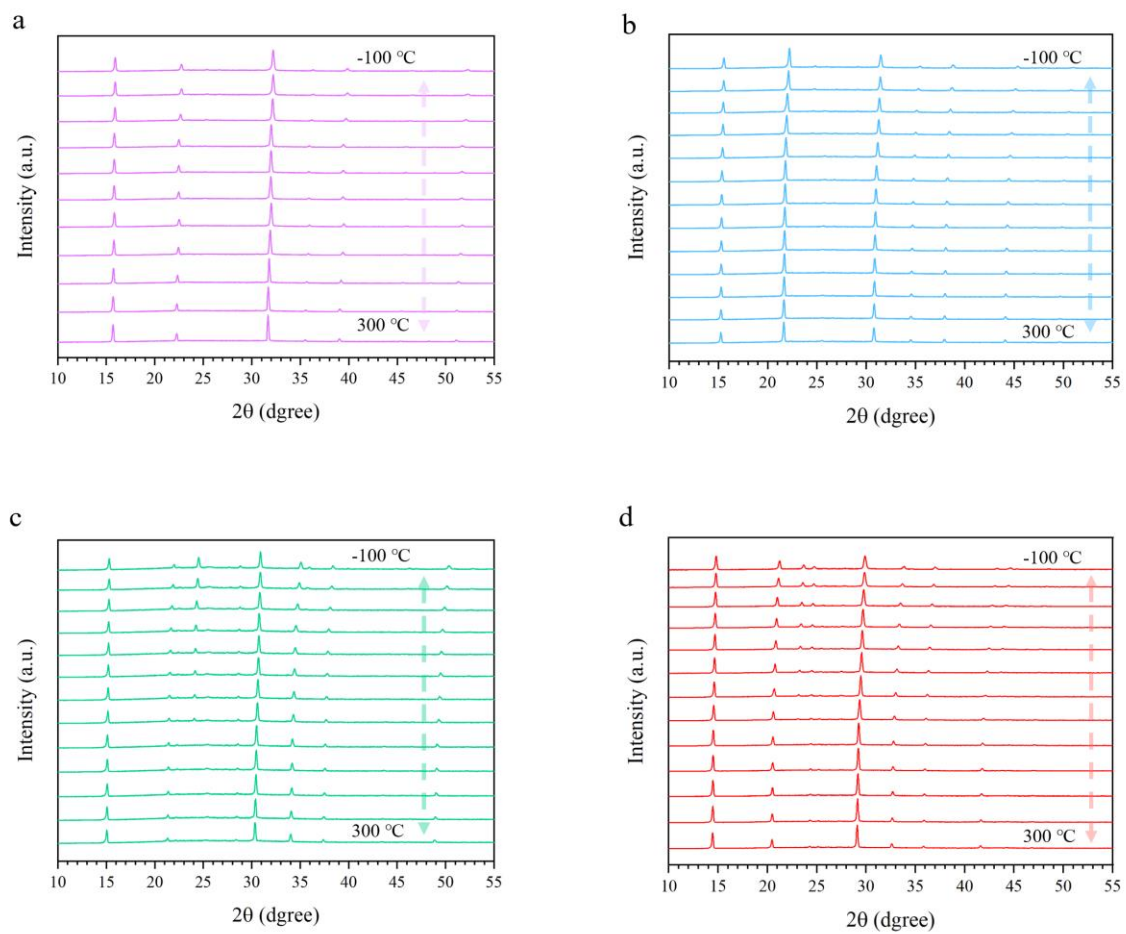


Fig. S20 TD-XRD spectra of perovskite thin films. a, CsPbCl_3 . b, CsPbClBr_2 . c, CsPbBr_3 . d, CsPbBrI_2 .

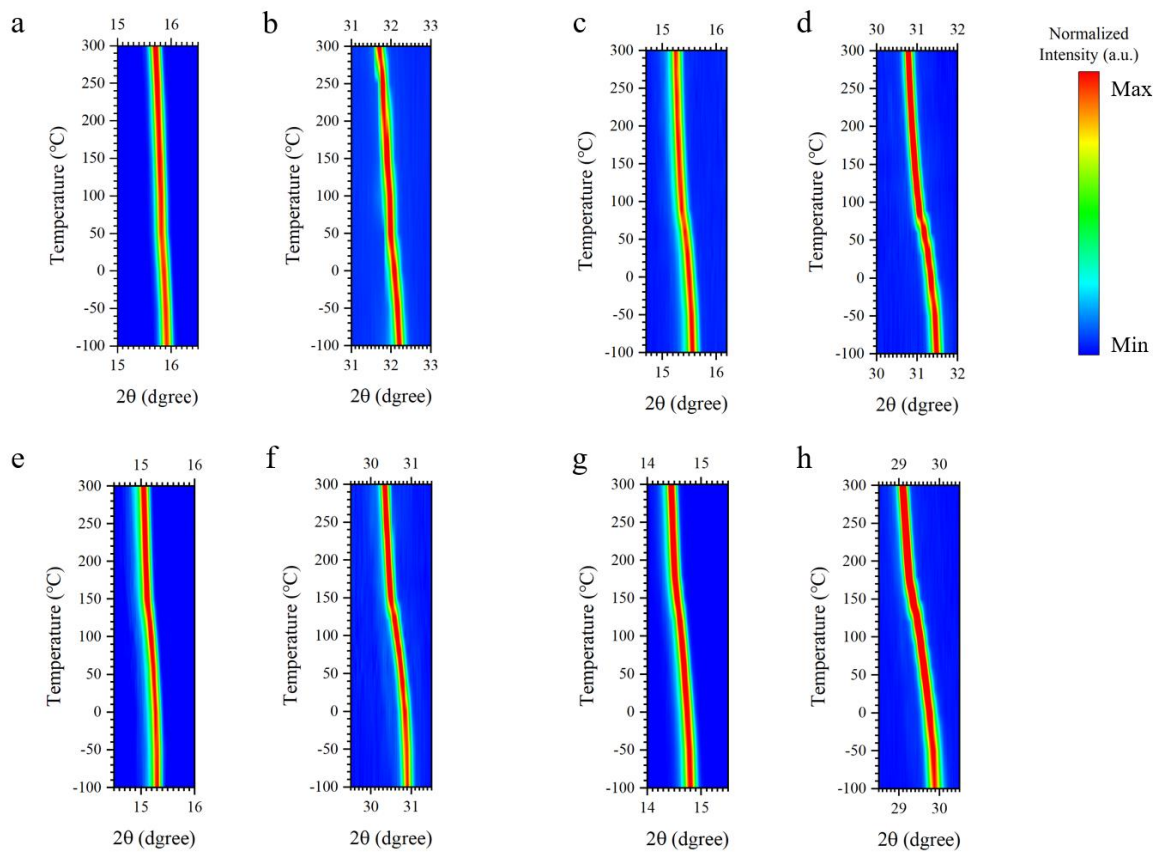


Fig. S21 Enlarged TD-XRD contour map of (100) and (200) planes of perovskite thin films. a, b,

c, d, CsPbClBr₂. e, f, CsPbBr₃. g, h, CsPbBr₂.

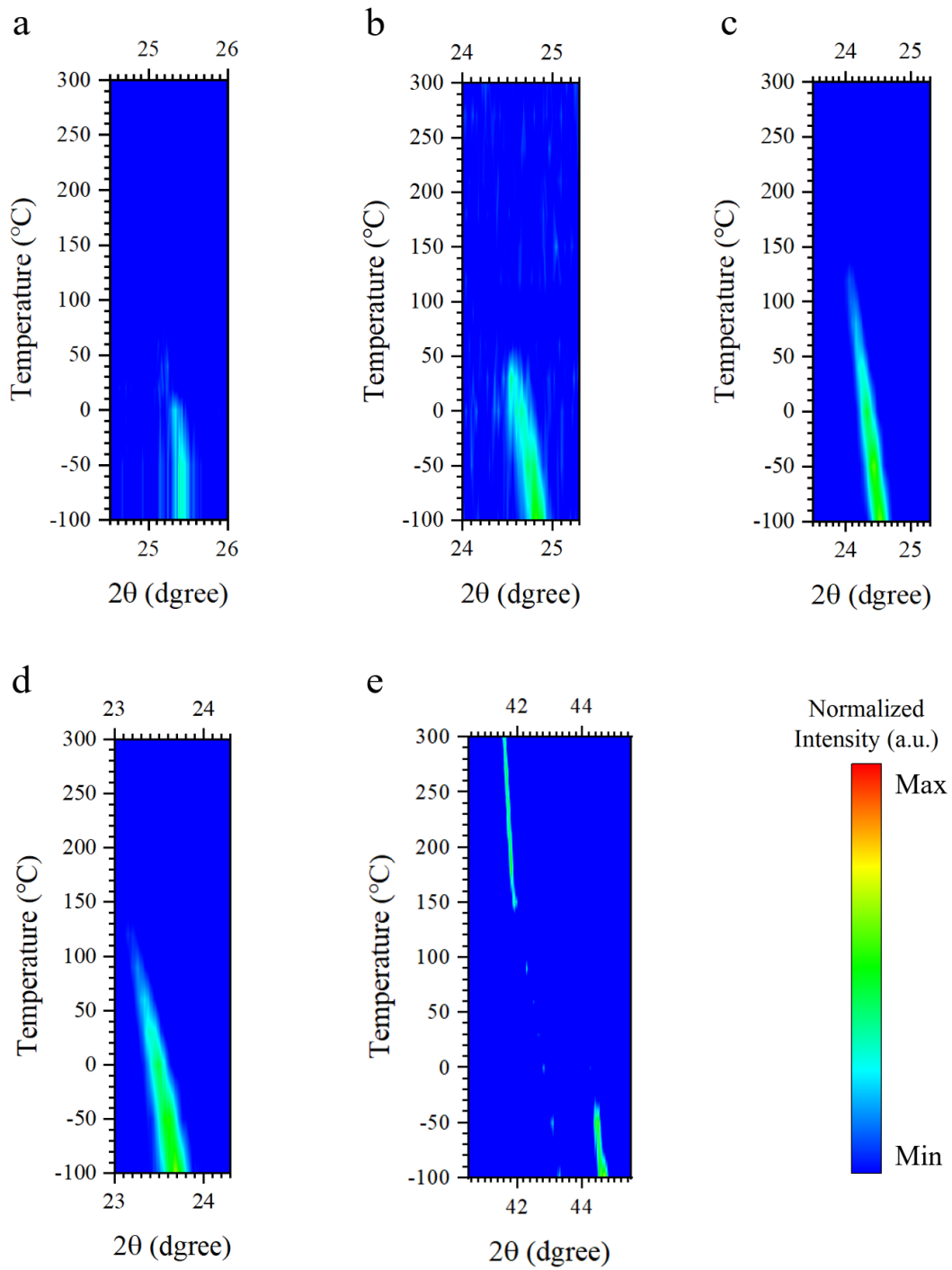


Fig. S22 Phase transition with the temperature evolution of perovskite thin films from TD-XRD

spectra. The (111) planes evolution of CsPbCl₃ (a), CsPbClBr₂ (b), CsPbBr₃ (c), and CsPbBrI₂ (d). e,

Two peaks evolution of CsPbBrI₂ at the range of 40.5° -45.5°.

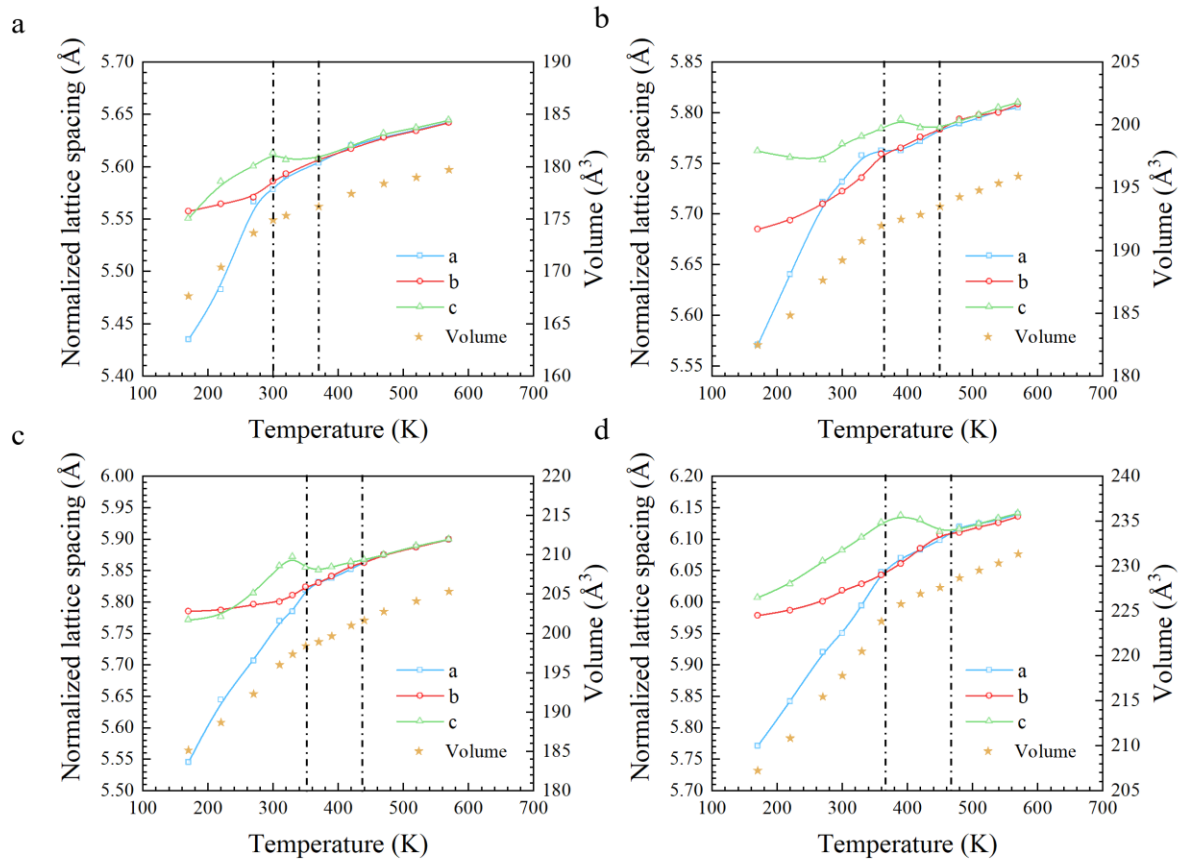


Fig. S23 Normalized anisotropic lattice constants and volumes of four materials with respect to temperature. The vertical dashes are the estimated phase transition points.

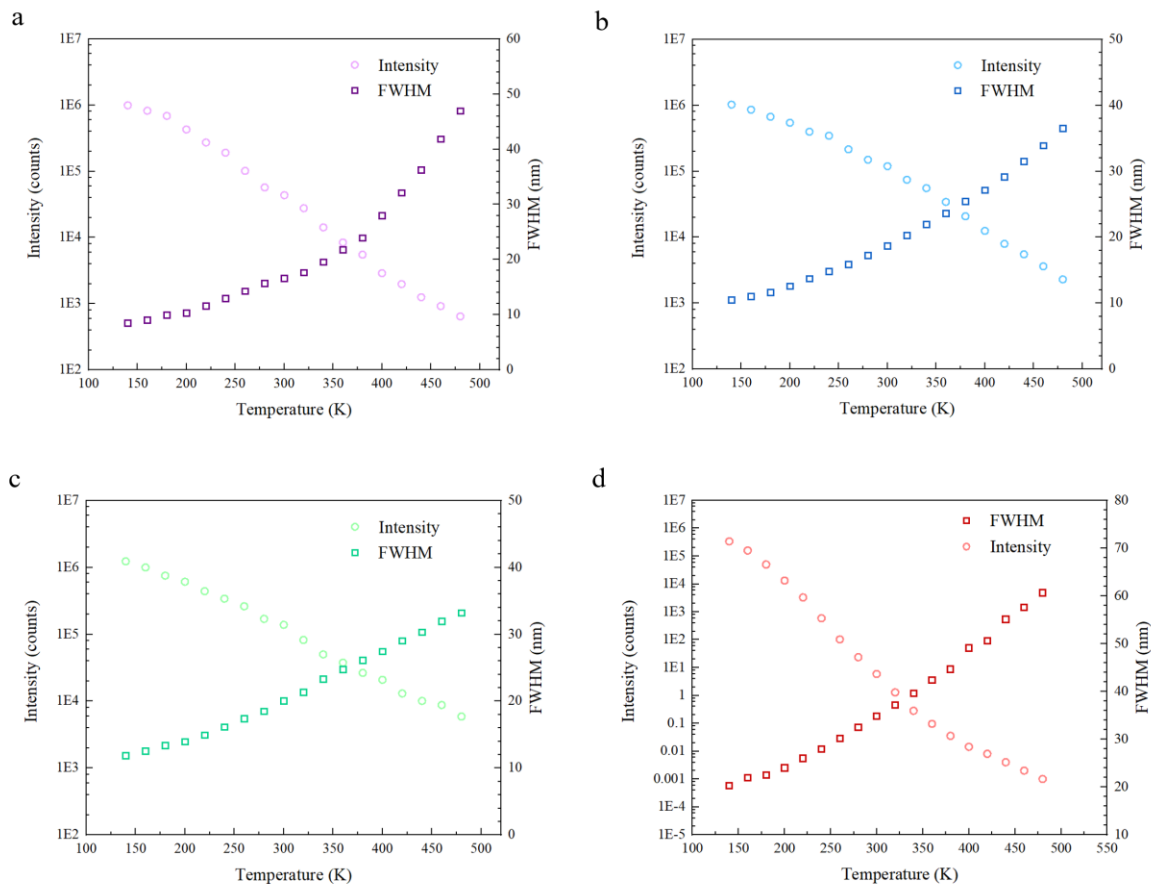


Fig. S24 The TD-PL intensity and FWHM of perovskite thin films. **a**, CsPbCl₃. **b**, CsPbClBr₂. **c**, CsPbBr₃. **d**, CsPbBrI₂.

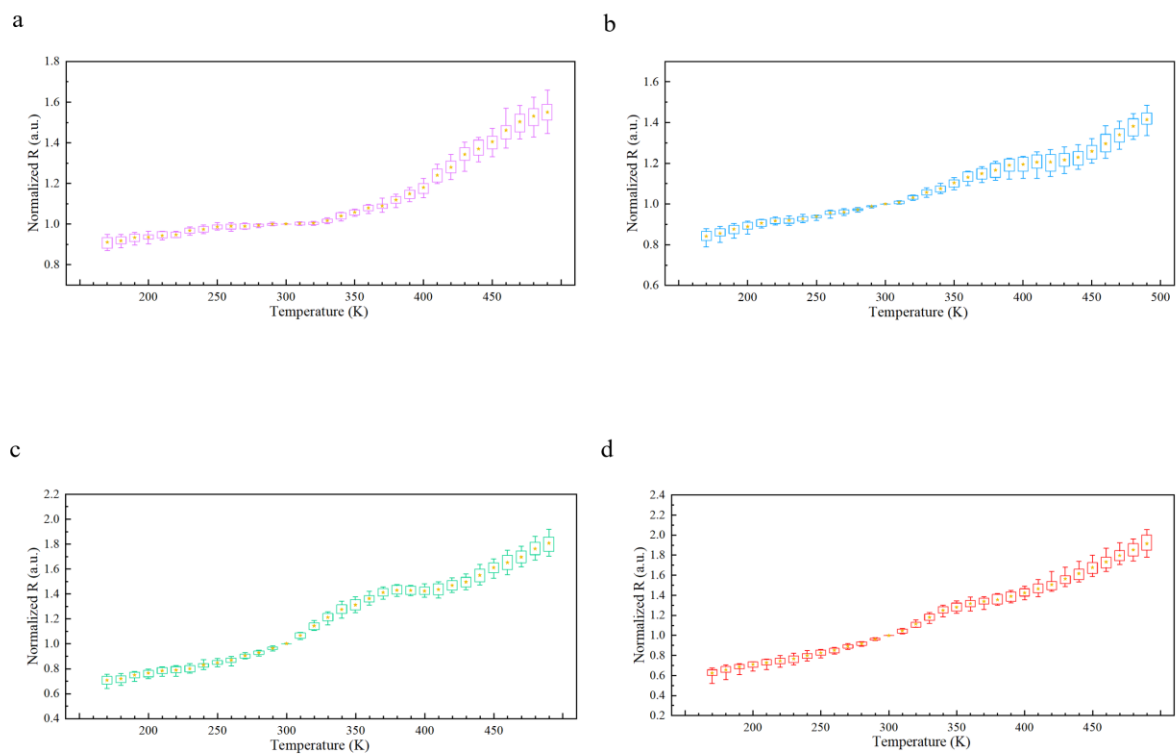


Fig. S25 Temperature dependent normalized responsivity of tetrachromatic image sensor. a,

b, CsPbClBr₂. **c,** CsPbBr₃. **d,** CsPbBrI₂.

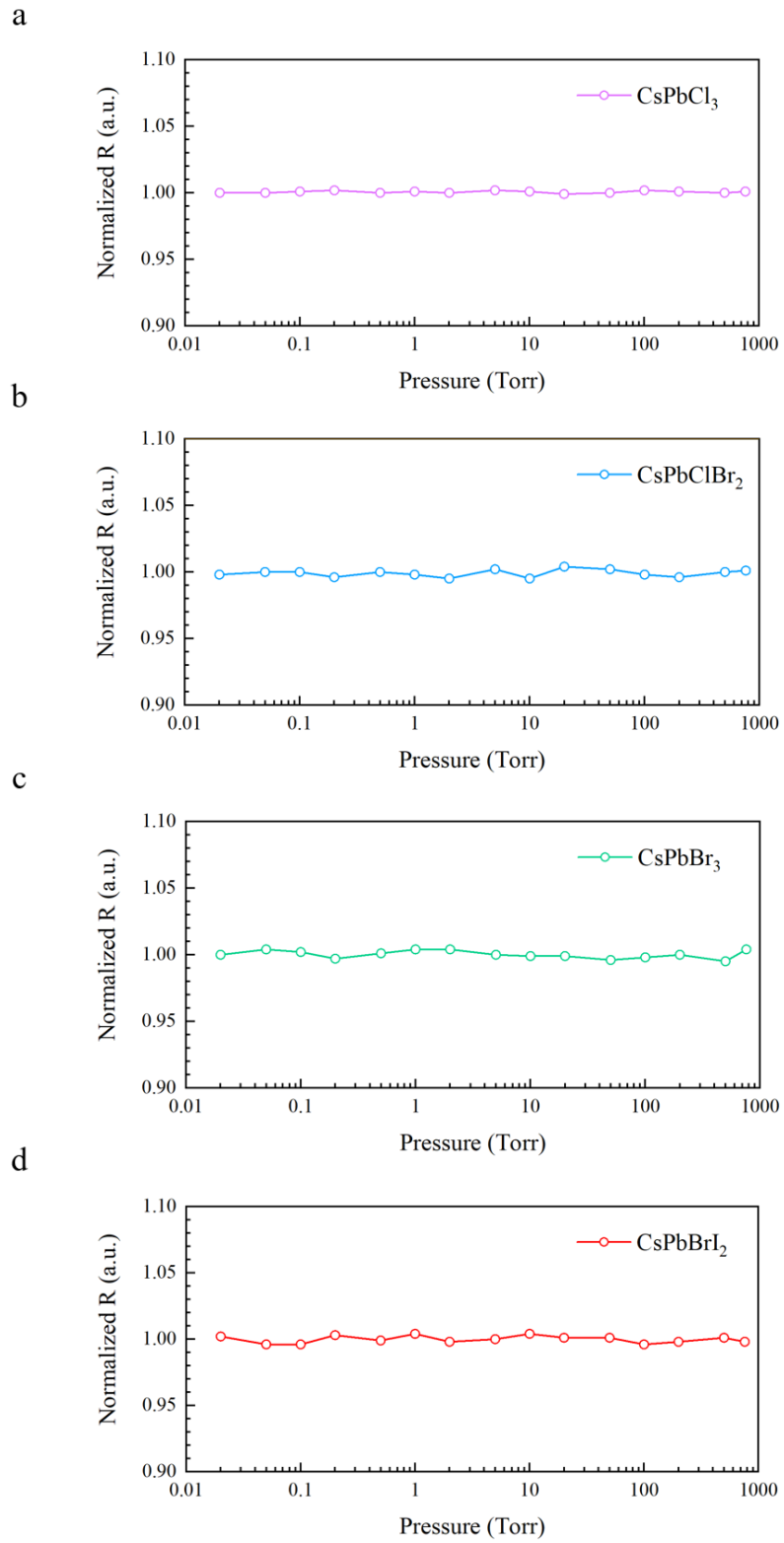


Fig. S26 Pressure dependent normalized responsivity. a, CsPbCl₃. b, CsPbClBr₂. c, CsPbBr₃. d,

CsPbBrI₂.

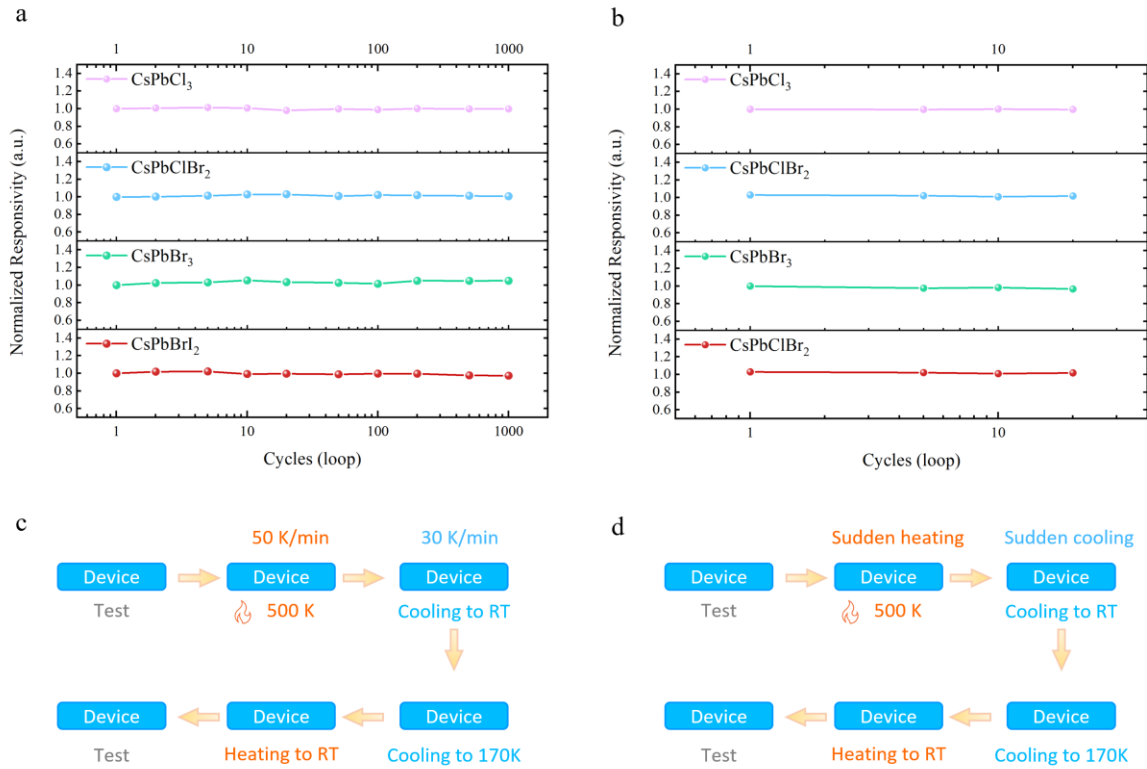


Fig. S27 Stability of devices with the simulated extravehicular thermal shock cycling test. a, Thermal cycling stability. **b**, Sudden temperature fluctuations cycling stability. **c**, The test process includes the following steps: measuring the device’s performance before cycling; heating it to 500 K by the heating rate of 50 K/min; cooling it to 170 K by the cooling rate of 30 K/min; heating it back to room temperature to measure the performance again. The test is running in a vacuum. **d**, A hotplate set to 500 K, a room-temperature metal plate, and a low-temperature vacuum stage set to 170 K. The device was kept on every stage for 1 min for every cycle.

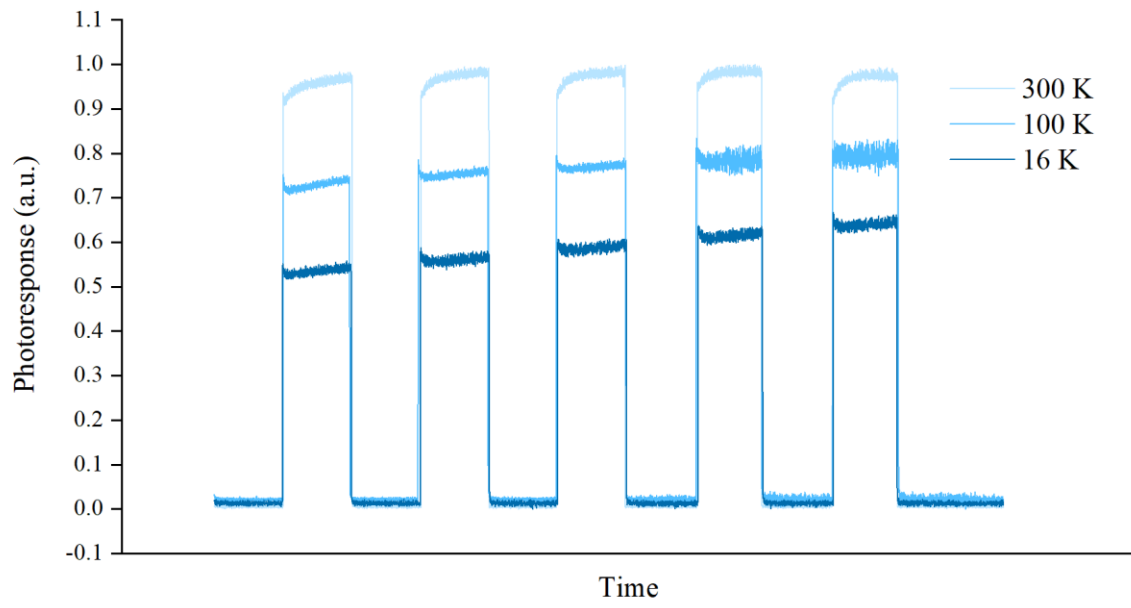


Fig. S28 Photoresponse of CsPbBr₃ layer (blue sensor) working under a cryogenic environment of 16 K. (Light source is 365 nm laser diode)

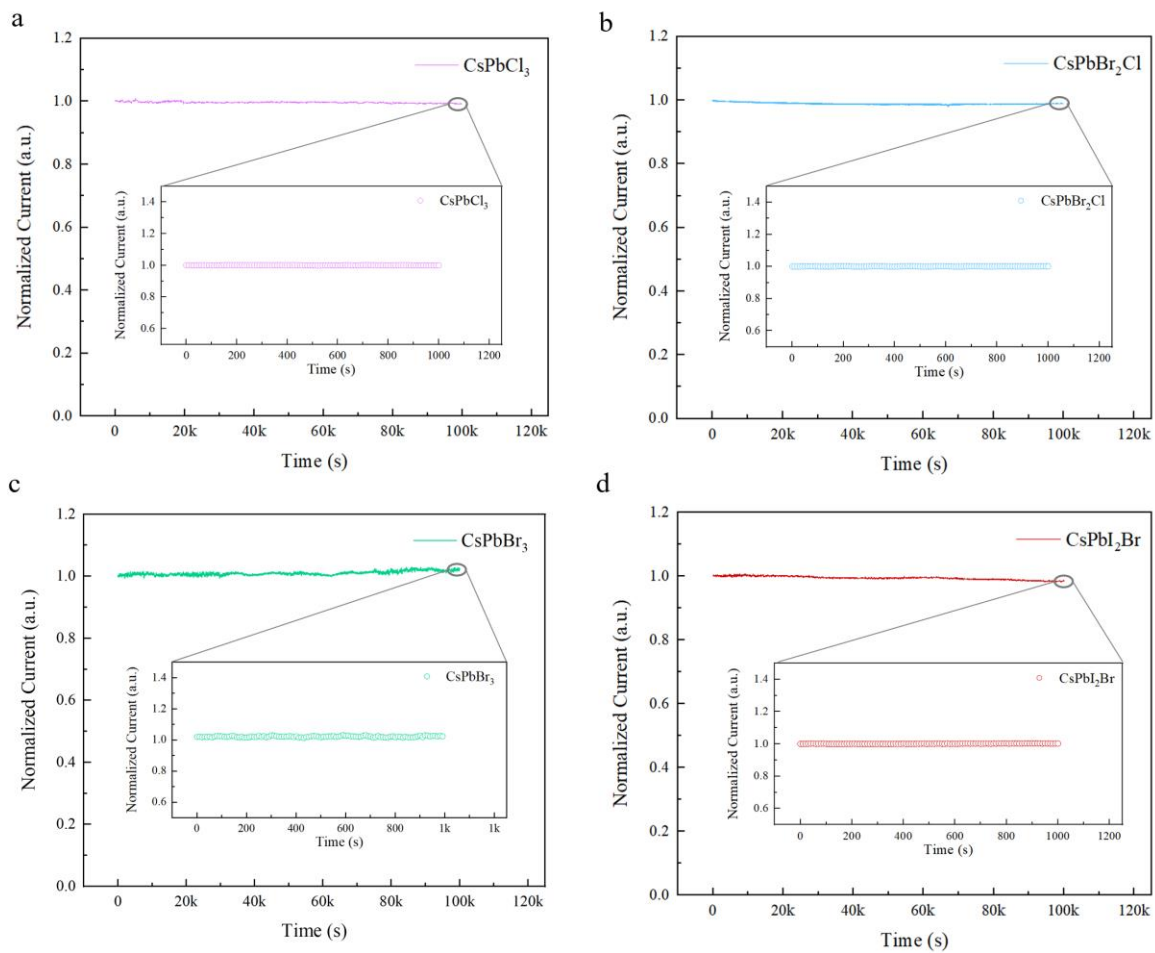


Fig. S29 Long-time device stability under continuous light soaking in a vacuum at 500 K. a,

b, CsPbCl_3 . **b,** CsPbClBr_2 . **c,** CsPbBr_3 . **d,** CsPbBrI_2 . Insets, zoom-in image from 99 ks to 100 ks.

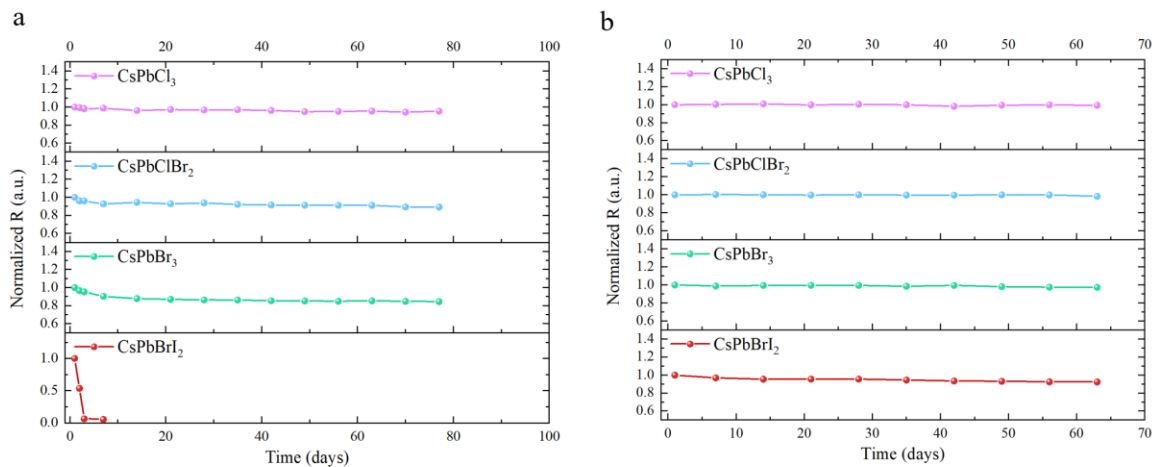


Fig. S30 Shelf stability of unencapsulated device under ambient storage (a) and vacuum (b) conditions.

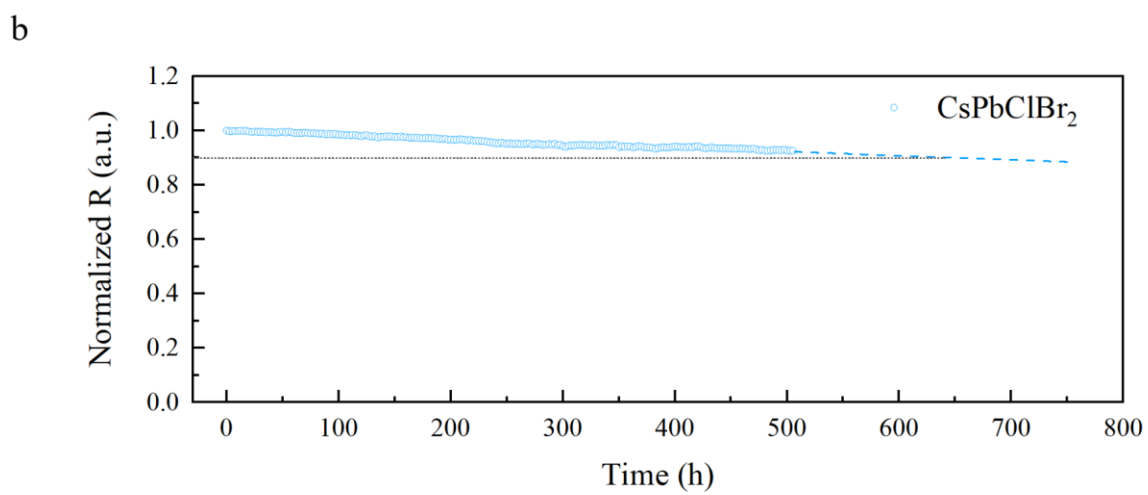
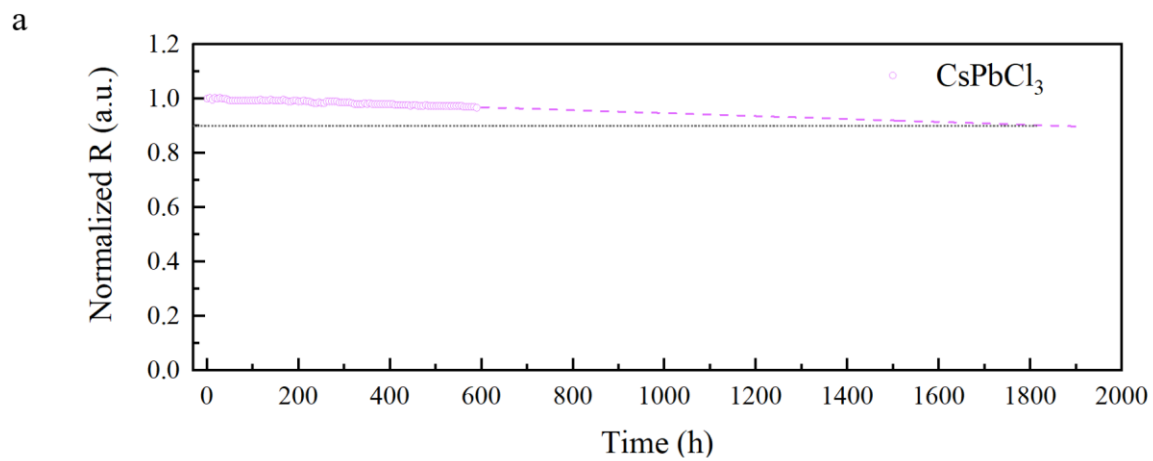
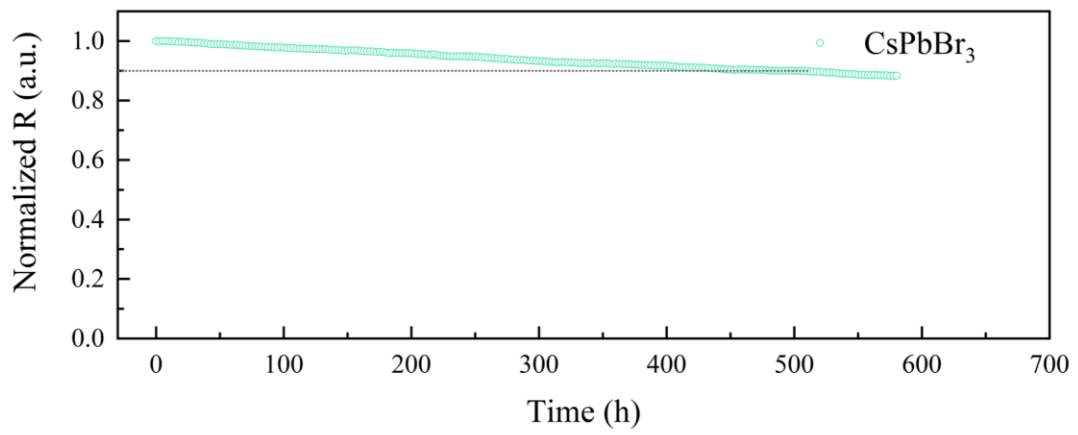


Fig. S31 Long-time operational device stability under continuous light soaking in a vacuum. a,

b, CsPbCl₃. **b,** CsPbClBr₂.

a



b

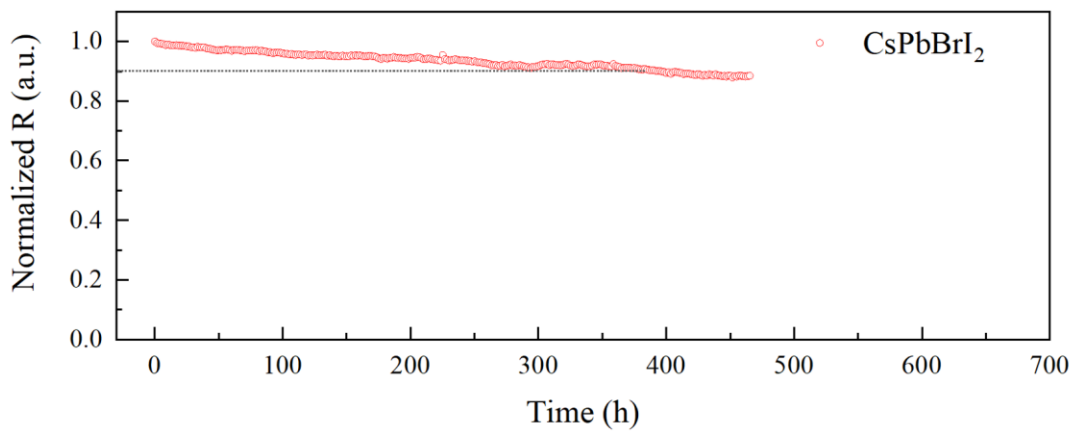


Fig. S32 Long-time operational device stability under continuous light soaking in a vacuum. a,

b, CsPbBr₃. **b,** CsPbBrI₂.

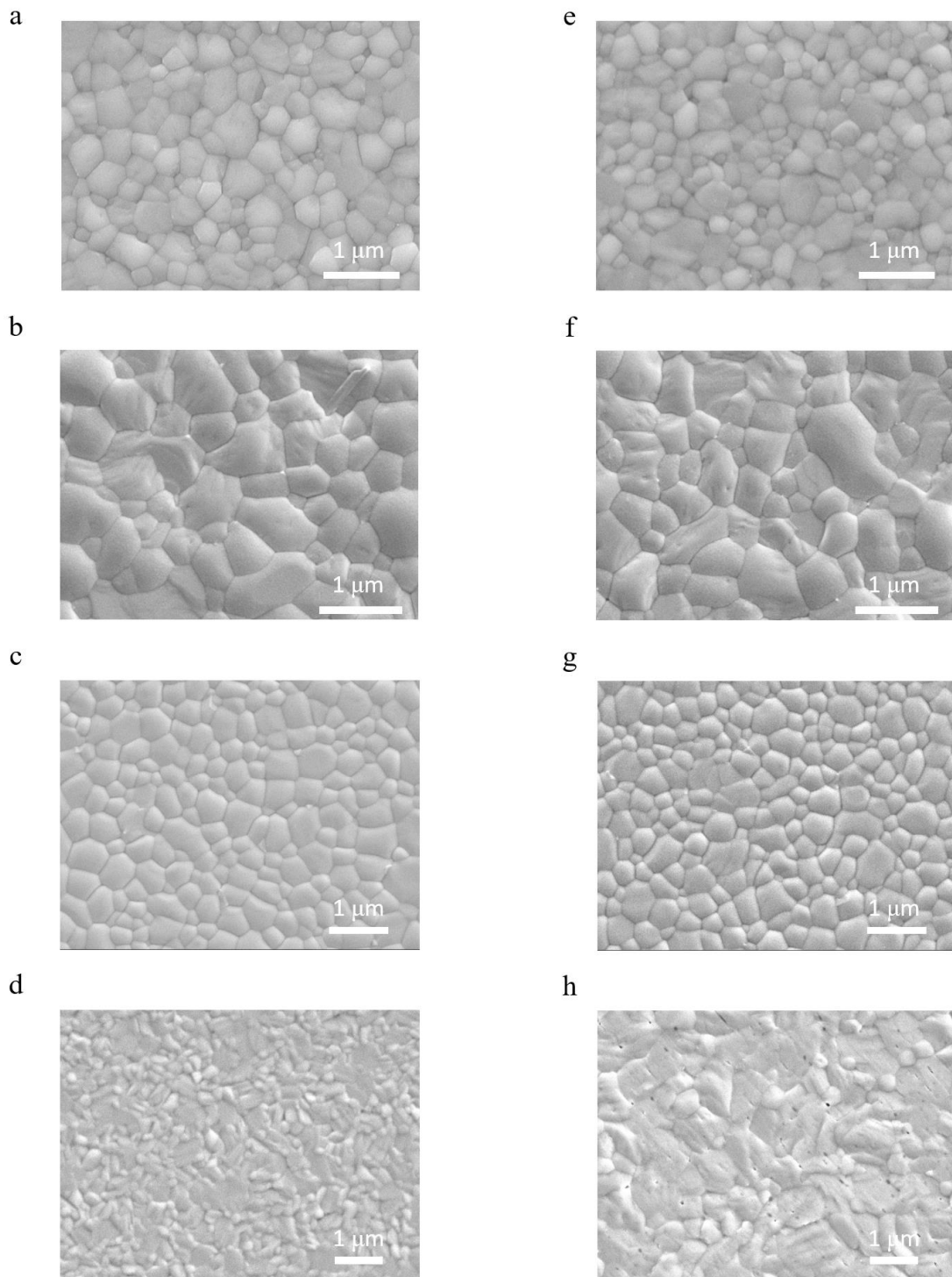


Fig. S33 SEM images of four materials before and after 100h annealing at 200 °C. Top view of CsPbCl_3 , CsPbClBr_2 , CsPbBr_3 , and CsPbBrI_2 thin films before (a-d) and after (e-h) annealing, respectively. Due to the easy decomposition of iodine-based perovskite in ambient air, we speculate that the black spots observed in the image are surface defects formed as a result of phase separation

or decomposition of CsPbBr₂. Moreover, the mixed halide perovskite thin films (CsPbClBr₂ and CsPbBr₂) are more prone to phase separation.

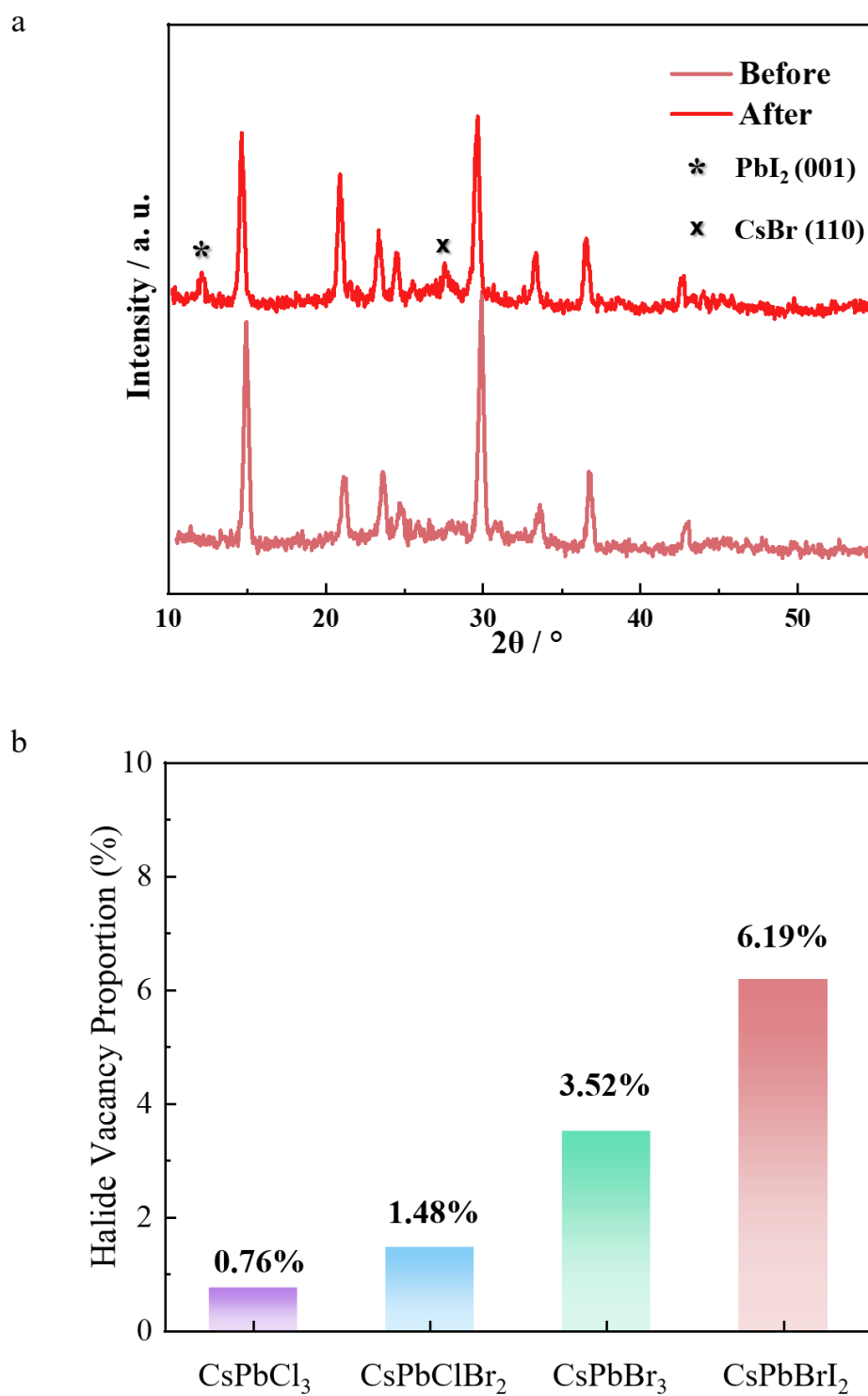


Fig. S34 a, XRD spectra of miscellaneous of CsPbBr₂ perovskite thin films. b, Halide vacancy proportion of each perovskite thin film compared with the films before annealing.

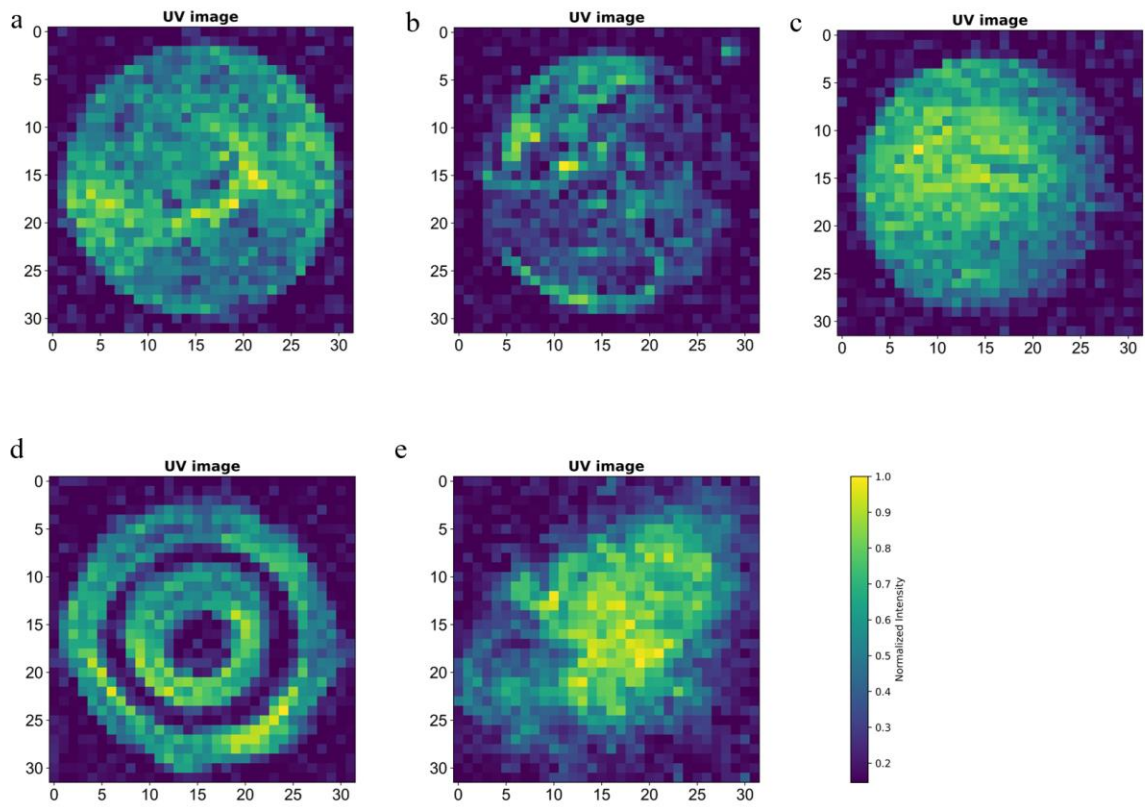


Fig. S35 UV channel demonstration. a, Earth; b, Neptune; c, Venus; d, Flame; e, Crab Nebula. All

images are grayscale.

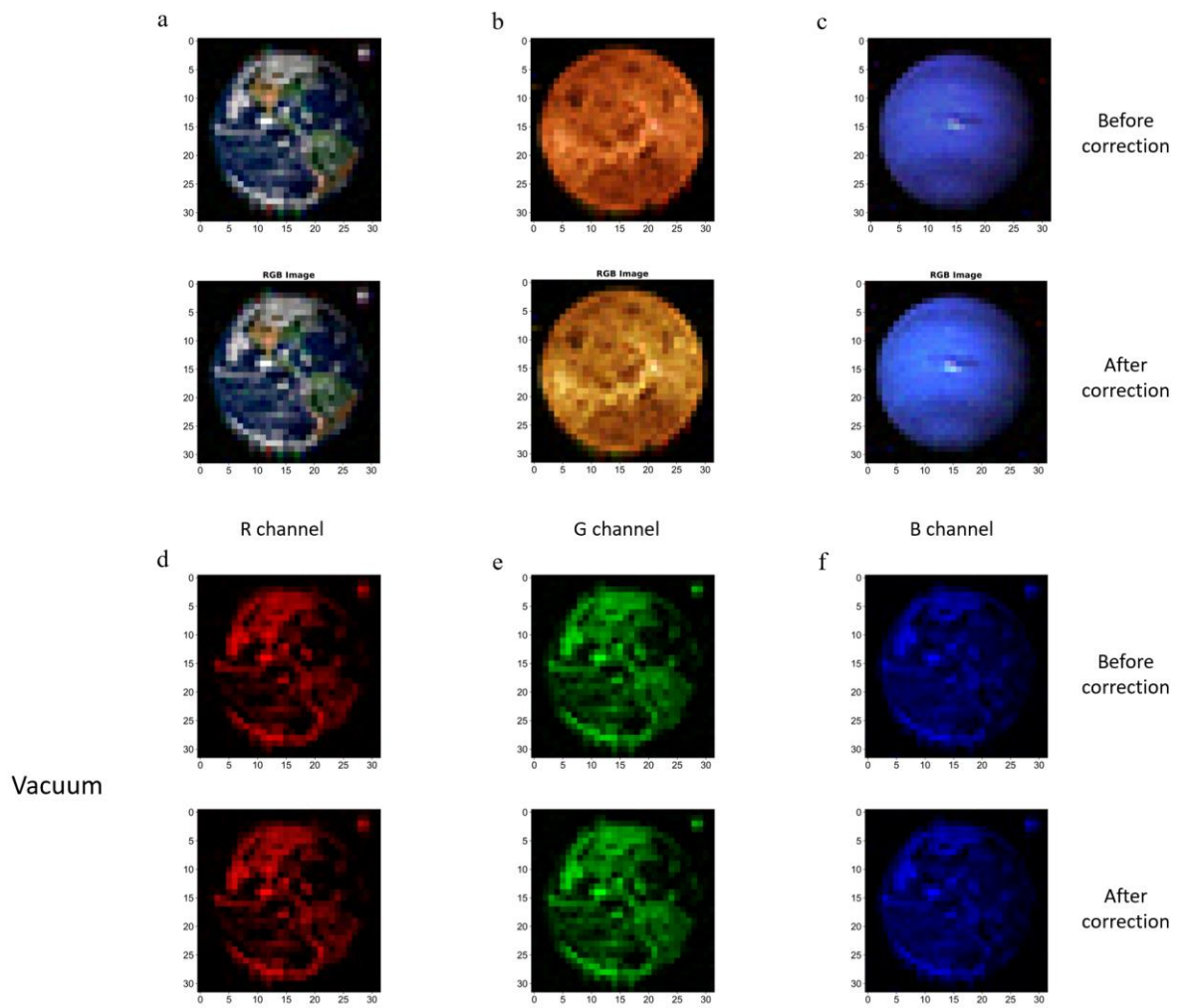


Fig. S36 RGB channels w/o temperature coefficient correction under the vacuum, low-, and high-temperature environments.

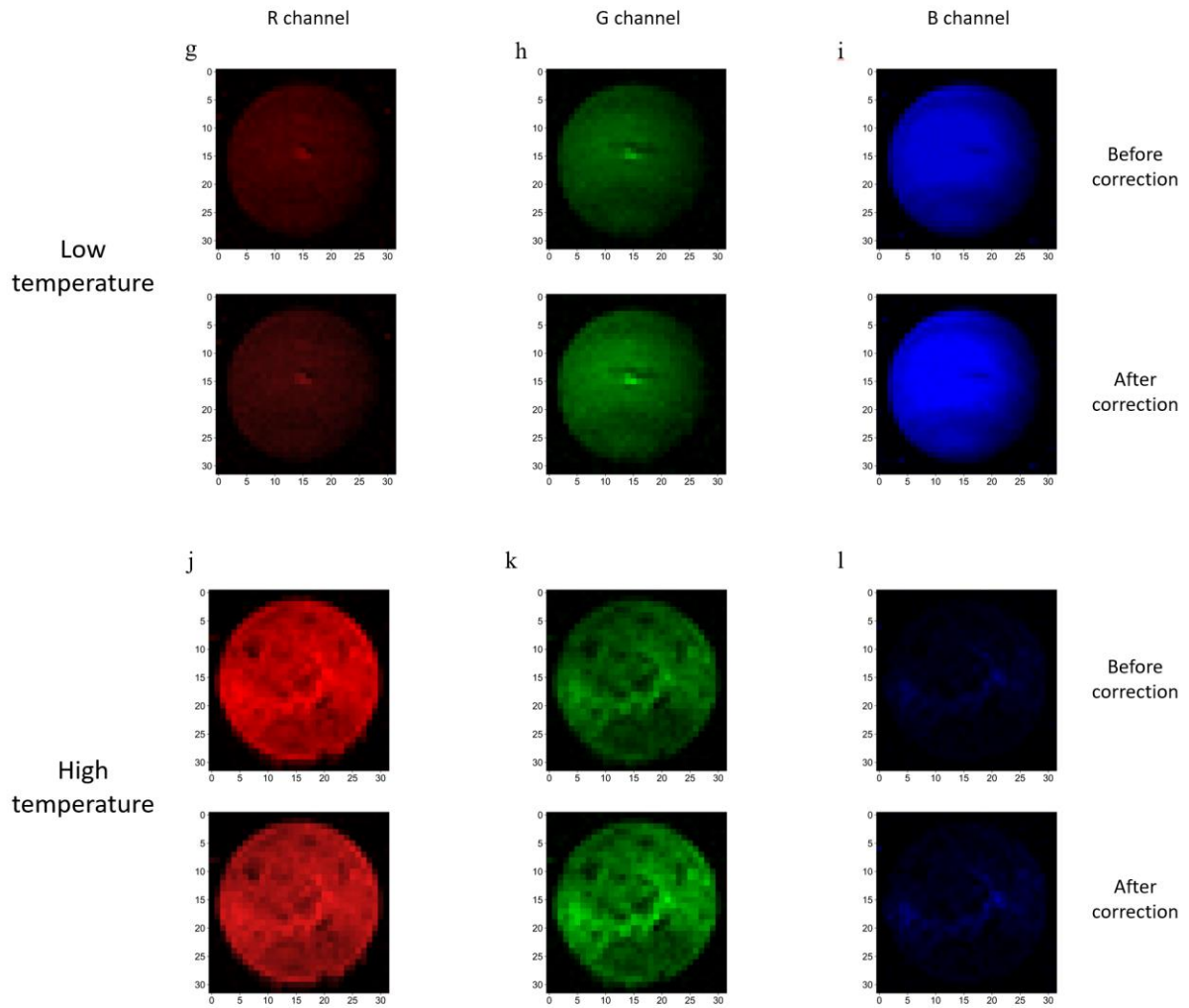


Fig. S36 RGB channels w/o temperature coefficient correction under the vacuum, low-, and high-temperature environments.

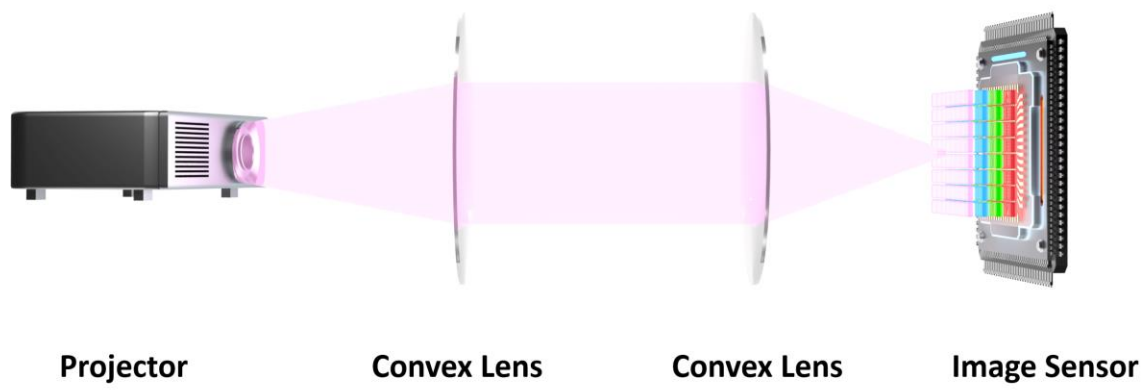


Fig. S37 Illustration of imaging setup.

8-Channel ADC

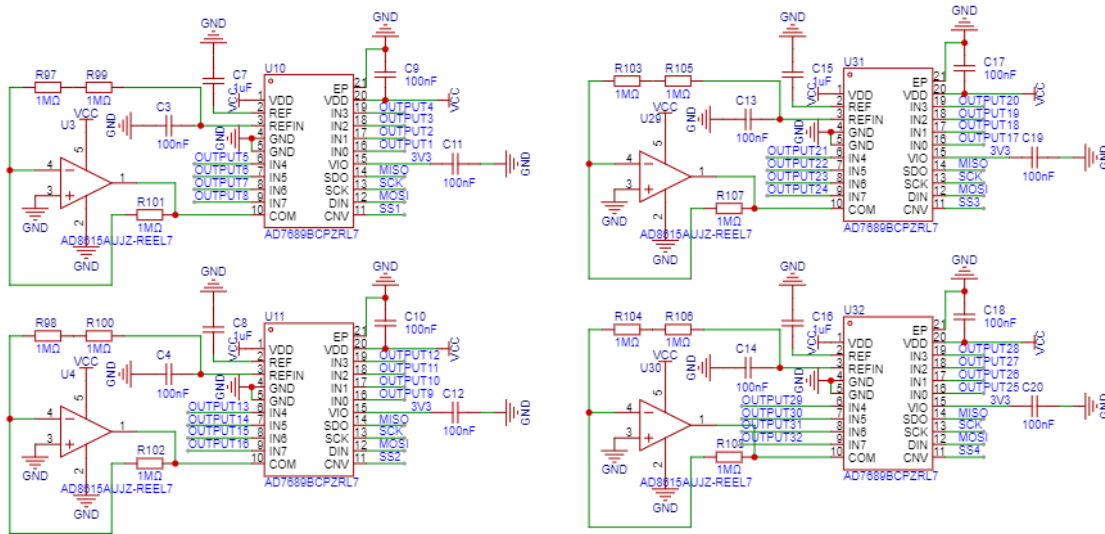
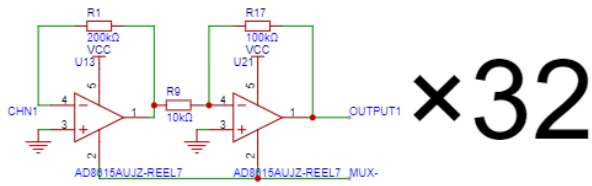
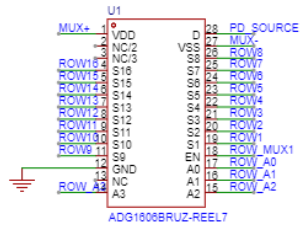


Fig. S38 Schematic diagram of signal-connecting circuits.

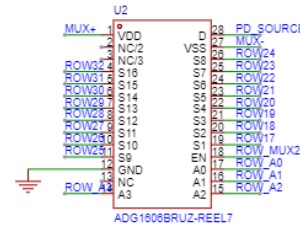
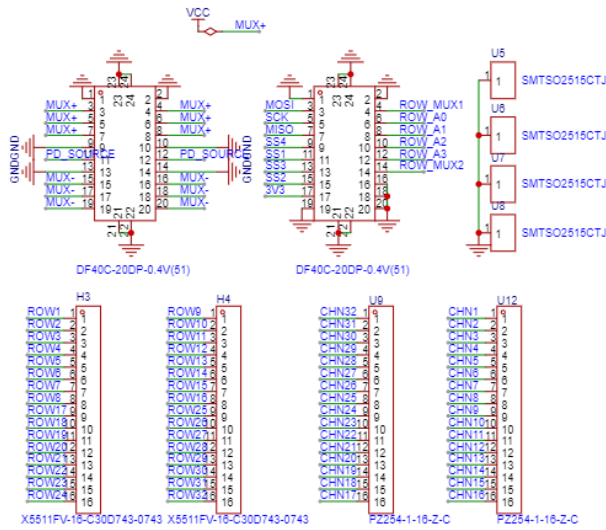
Amplifier



Multiplexer



Connector



By-pass Capacitors

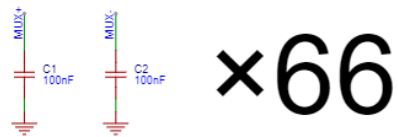


Fig. S38 Schematic diagram of signal-connecting circuits.

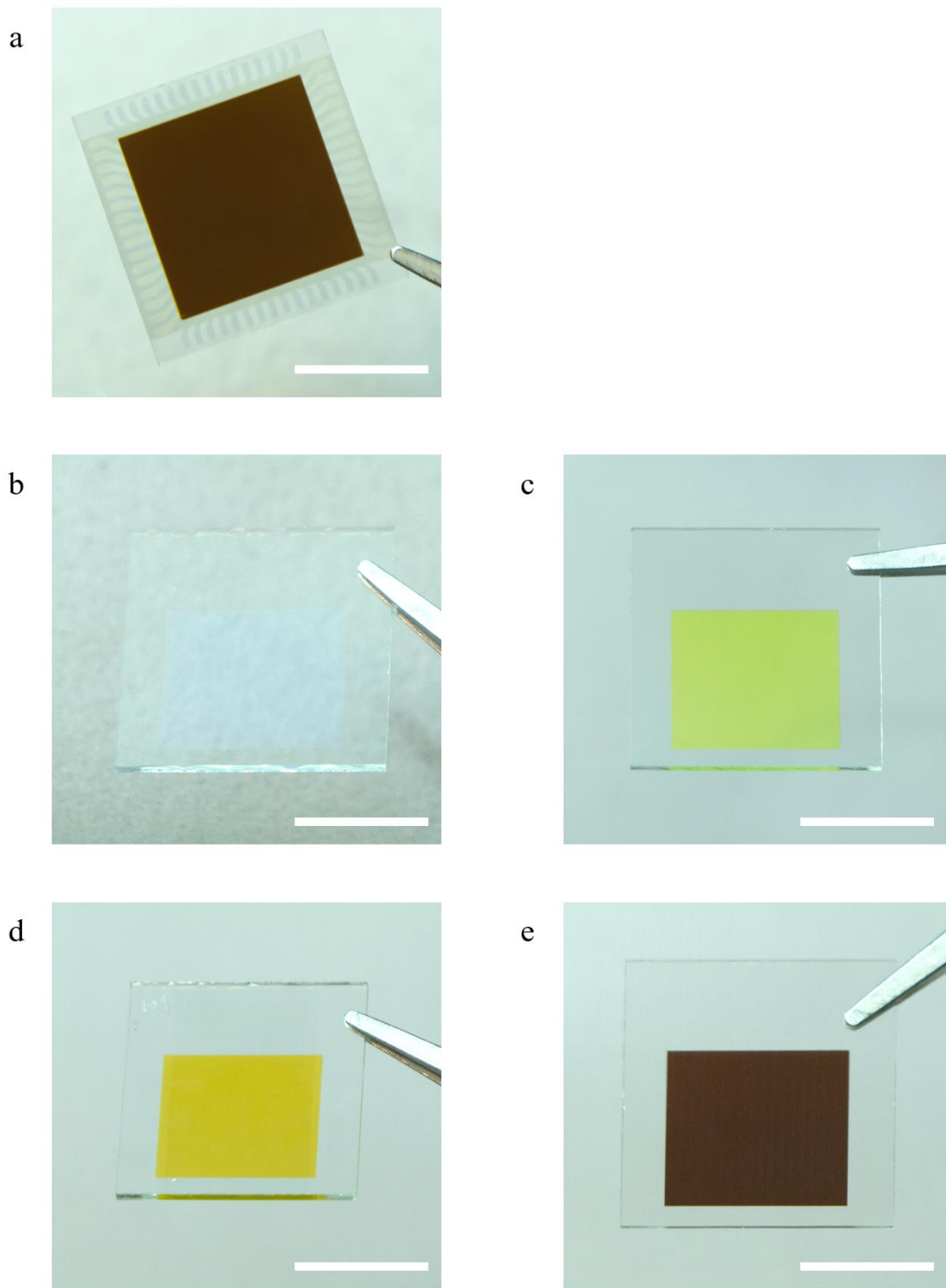


Fig. S40 Photograph of tetrachromatic image sensor and single layer perovskite thin films. a,

Entire Device. **b,** CsPbCl_3 , **c,** CsPbClBr_2 . **d** CsPbBr_3 . **e,** CsPbBrI_2 . Scale bar, 1 cm.

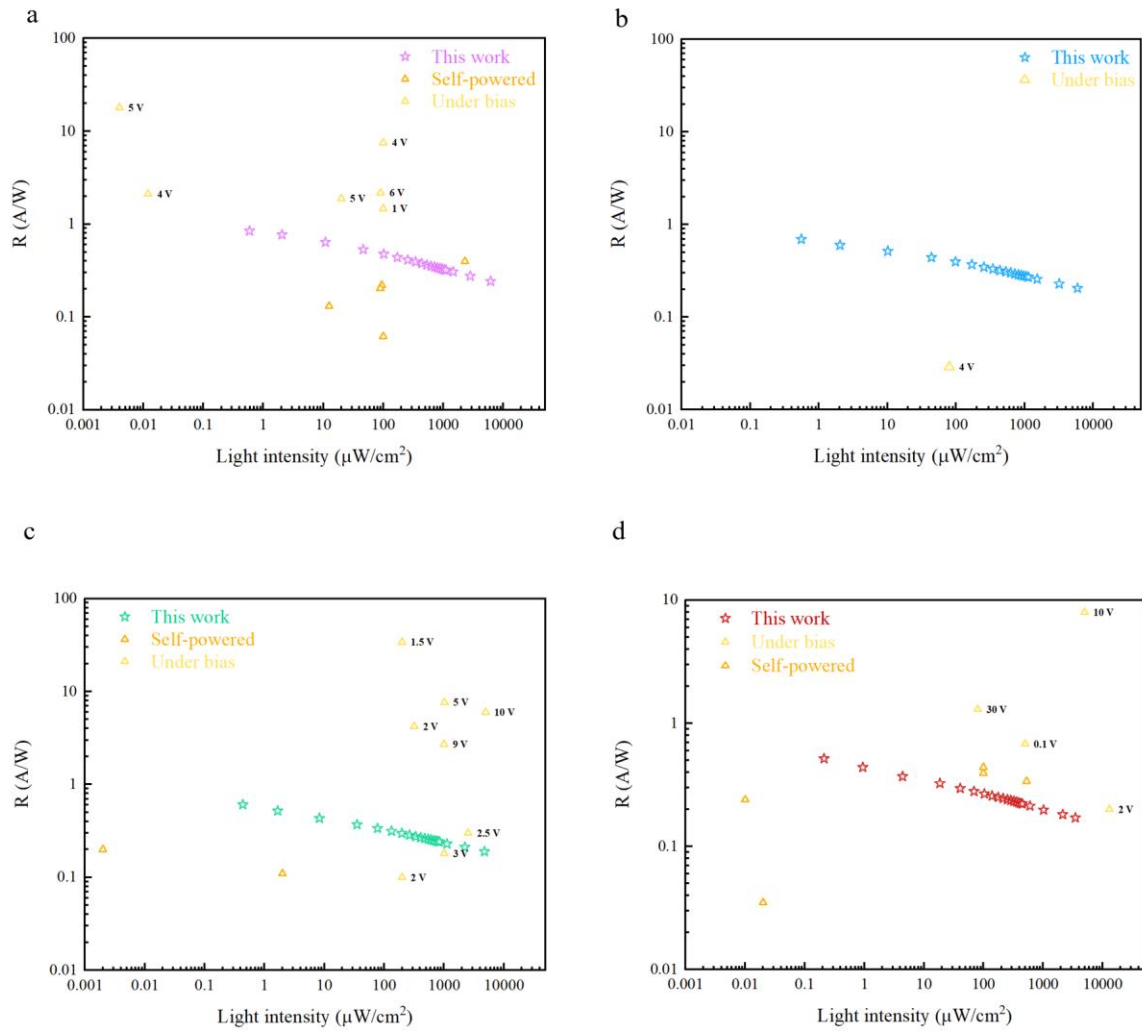


Fig. S41 Benchmark of the perovskite photodetectors' responsivity with a function of light

intensity. a, CsPbCl_3 . b, CsPbClBr_2 . c, CsPbBr_3 . d, CsPbBrI_2 .

Table S1 Comparison of the device performance between the tetrachromatic perovskite imaging sensor and other reported perovskite-based photodetectors.

Material	Device structure	Wavelength (nm)	Bias (V)	Responsivity (A/W)	Response time	Detectivity (Jones)	Light intensity	Ref.
MAPbCl ₃ PF/ZnO	Photocunductor	365	1	1.47	7.8 s/ 1.2 s		100 μW/cm ²	S3
CsPbCl ₃ PF/PbS	Photocunductor	375	0	0.22	1.92 μs/ 4.45 μs	4.06×10 ¹³	94.45 μW/cm ²	S4
CsPbCl ₃ -Cs ₄ PbCl ₆ PF	Photocunductor	405	0	0.0618	2.1 μs/ 5.3 μs	1.35×10 ¹²	100 μW/cm ²	S5
MAPbCl ₃ MC	Photocunductor	385	5	18	1 ms	1×10 ¹²	4 nW	S6
CsPbCl ₃ MC	Photocunductor	365	4	2.11	77 ms/ 63 ms	5.6×10 ¹²	0.012 μW/cm ²	S7
CsPbCl ₃ NW	Photodiode	360	0	0.398	24 ms/ 22 ms	3.3×10 ¹¹	2.3 mW/cm ²	S8
MAPbCl ₃ SC	Photocunductor	365	15	0.0469	24 ms/ 62 ms	1.2×10 ¹⁰	1 W/cm ²	S9
CsPbCl ₃ PF	Photocunductor	405	6	2.17	2.9 ms/ 18.8 ms	3.08×10 ¹²	0.09 mW/cm ²	S10
MAPbCl ₃ PF	Photocunductor	360	4	7.56	170 μs/ 220 μs		0.1 mW/cm ²	S11
MAPbCl ₃ PF	Photodiode	395	0	0.2028	3.91 ms/ 4.55 ms	4.49×10 ¹²	0.089 mW/cm ²	S12
CsPbCl ₃ NC	Photocunductor	365	5	1.89	41 ms/ 43 ms		~0.02 mW/cm ²	S13
CsPbCl ₃ PF	Photodiode	365	0	0.1309	46 μs/ 46 μs	1.4×10 ¹³	12.5 μW/cm ²	S14
CsPbClBr ₂ PF	Photocunductor	405	4	0.02893	270 ms/ 310 ms	5.32×10 ¹⁰	0.08 mW/cm ²	S15
CsPbBr ₃ PF	Photodiode	535	0	0.1066	3.9 ms/ 3.21 ms	2.2×10 ¹²		S16
CsPbBr ₃ SCF	Photocunductor	405	2.5	0.3	200 ns/ 300 ns		2.54 mW/cm ²	S17
CsPbBr ₃ PF	Photocunductor	405	6	55	430 μs/ 318 μs	9×10 ¹²	0.03 mW	S18
CsPbBr ₃ NC	Photocunductor	442	3	0.18	1 ms/ 1.8 ms		1.01 mW/cm ²	S19
CsPbBr ₃ PF	Photocunductor	520	9	2.7	0.35 ms/ 1.26 ms		1 mW/cm ²	S20
CsPbBr ₃ NP	Photocunductor	442	1.5	34	0.6 ms/ 0.9 ms	7.5×10 ¹²	0.2 mW/cm ²	S21

MAPbBr ₃ NC	Photocunductor	550	2	0.1	0.08 s / 0.09 s		0.2 mW/cm ²	S22
MAPbBr ₃ NC	Photodiode	540	0	~0.26-0.1	/ 7.2 μs	1.5×10 ¹³	0.35 pW/cm ² - 2 W/cm ²	S23
CsPbBr ₃ NC	Photocunductor	550	10	6			5 mW/cm ²	S24
CsPbBr ₃ NS	Photocunductor	517	10	0.64	19 μs/ 24 μs			S25
CsPbBr ₃ MW	Photodiode	532	2	4.2		9.9×10 ⁸	0.318 mW/cm ²	S26
CsPb ₂ Br ₅ -CsPbBr ₃ PF	Photodiode	473	0	0.11	6 μs/ 64 μs	1.4×10 ¹²	2 μW/cm ²	S27
CsPbBr ₃ MW	Photocunductor	400	5	7.66	275 ms/ 550 ms	4.05×10 ¹²	1.02 mW/cm ²	S28
FAPbI ₃ SC	Photodiode	380	-0.1	0.68	12.4 ms/ 17.2 ms		0.5 mW/cm ²	S29
MAPbI ₃ SC	Photocunductor	White light	2	~0.2			13 mW/cm ²	S30
MAPbI ₃ SC	Photocunductor	808	0	0.24	71 μs/ 112 μs		10 nW/cm ²	S31
MAPbI ₃ NW	Photocunductor	650	30	1.3	0.2 ms/ 0.3 ms	2.5×10 ¹²	80 μW/cm ²	S32
MAPbI ₃ PF	Photodiode	600	0	0.395	1.2 μs/ 3.2 μs	1×10 ¹²	0.1 mW/cm ²	S33
MAPbI ₃ PF	Photodiode	500	0	0.339	~0.1-1 μs	4.8×10 ¹²	0.53 mW/cm ²	S34
MAPbI ₃ PF	Photocunductor	White light	10	~8	<290 ms/ <20 ms	1.3×10 ¹¹	5 mW/cm ²	S35
CsPbI ₃ NC	Photodiode	640	0	0.035		1.8×10 ¹²	~20 nW/cm ²	S36
CsPbI ₃ :Er ³⁺ PQDs	Photodiode	460	0	0.4398	~0.25 ms/ 0.25 ms	2.46×10 ¹²	0.1 mW/cm ²	S37
CsPbI ₃ NW	Photocunductor	460	-1	0.0067	0.292 s/ 0.234 s	1.57×10 ⁸	1.5 mW/cm ²	S38
CsPbI ₃ QDs	Photodiode	450	0	0.105		5×10 ¹³		S39

References

- S1. Smith, T., and Guild, J. (1931). The C.I.E. colorimetric standards and their use. *Transactions of the Optical Society* *33*, 73–134. 10.1088/1475-4878/33/3/301.
- S2. Kim, H., Kim, W., Pak, Y., Yoo, T.J., Lee, H., Lee, B.H., Kwon, S., and Jung, G.Y. (2020). Bias-Modulated Multicolor Discrimination Enabled by an Organic–Inorganic Hybrid Perovskite Photodetector with a p-i-n-i-p Configuration. *Laser Photon Rev* *14*, 2000305. 10.1002/lpor.202000305.
- S3. Yang, J., Liu, K., Cheng, Z., Jing, P., Ai, Q., Chen, X., Li, B., Zhang, Z., Zhang, L., Zhao, H., et al. (2018). Investigation of Interface Effect on the Performance of CH₃NH₃PbCl₃/ZnO UV Photodetectors. *ACS Appl Mater Interfaces* *10*, 34744–34750. 10.1021/acsami.8b11722.
- S4. Zhan, X., Zhang, X., Liu, Z., Chen, C., Kong, L., Jiang, S., Xi, S., Liao, G., and Liu, X. (2021). Boosting the Performance of Self-Powered CsPbCl₃-Based UV Photodetectors by a Sequential Vapor-Deposition Strategy and Heterojunction Engineering. *ACS Appl Mater Interfaces* *13*, 45744–45757. 10.1021/acsami.1c15013.
- S5. Zhu, W., Deng, M., Chen, D., Zhang, Z., Chai, W., Chen, D., Xi, H., Zhang, J., Zhang, C., and Hao, Y. (2020). Dual-Phase CsPbCl₃–Cs₄PbCl₆ Perovskite Films for Self-Powered, Visible-Blind UV Photodetectors with Fast Response. *ACS Appl Mater Interfaces* *12*, 32961–32969. 10.1021/acsami.0c09910.
- S6. Adinolfi, V., Ouellette, O., Saidaminov, M.I., Walters, G., Abdelhady, A.L., Bakr, O.M., and Sargent, E.H. (2016). Fast and Sensitive Solution-Processed Visible-Blind Perovskite UV Photodetectors. *Advanced Materials* *28*, 7264–7268. 10.1002/adma.201601196.
- S7. Zhu, Z., Deng, W., Li, W., Chun, F., Luo, C., Xie, M., Pu, B., Lin, N., Gao, B., and Yang, W. (2021). Antisolvent-Induced Fastly Grown All-Inorganic Perovskite CsPbCl₃ Microcrystal Films for High-Sensitive UV Photodetectors. *Adv Mater Interfaces* *8*, 2001812. 10.1002/admi.202001812.
- S8. Wu, X., Sun, J., Shao, H., Zhai, Y., Li, L., Chen, W., Zhu, J., Dong, B., Xu, L., Zhou, D., et al. (2021). Self-powered UV photodetectors based on CsPbCl₃ nanowires enabled by the synergistic effect of acetate and lanthanide ion passivation. *Chemical Engineering Journal* *426*, 131310. 10.1016/j.cej.2021.131310.
- S9. Maculan, G., Sheikh, A.D., Abdelhady, A.L., Saidaminov, M.I., Haque, M.A., Murali, B., Alarousu, E., Mohammed, O.F., Wu, T., and Bakr, O.M. (2015). CH₃NH₃PbCl₃ Single Crystals: Inverse Temperature Crystallization and Visible-Blind UV-Photodetector. *J Phys Chem Lett* *6*, 3781–3786. 10.1021/acs.jpcllett.5b01666.
- S10. Guo, T., Zhao, S., Chu, Z., Ma, J., Xu, W., Li, Y., Shi, Z., and Ran, G. (2022). Large-Area large-grain CsPbCl₃perovskite films by confined re-growth for violet photodetectors. *Nanotechnology* *33*. 10.1088/1361-6528/ac6f65.

- S11. Wang, W., Xu, H., Cai, J., Zhu, J., Ni, C., Hong, F., Fang, Z., Xu, F., Cui, S., Xu, R., et al. (2016). Visible blind ultraviolet photodetector based on $\text{CH}_3\text{NH}_3\text{PbCl}_3$ thin film. *Opt Express* *24*, 8411. 10.1364/OE.24.008411.
- S12. Zhou, Y., Qiu, X., Wan, Z., Long, Z., Poddar, S., Zhang, Q., Ding, Y., Chan, C.L.J., Zhang, D., Zhou, K., et al. (2022). Halide-exchanged perovskite photodetectors for wearable visible-blind ultraviolet monitoring. *Nano Energy* *100*, 107516. 10.1016/j.nanoen.2022.107516.
- S13. Zhang, J., Wang, Q., Zhang, X., Jiang, J., Gao, Z., Jin, Z., and Liu, S. (Frank) (2017). High-performance transparent ultraviolet photodetectors based on inorganic perovskite CsPbCl_3 nanocrystals. *RSC Adv* *7*, 36722–36727. 10.1039/C7RA06597C.
- S14. Yang, L., Tsai, W.-L., Li, C.-S., Hsu, B.-W., Chen, C.-Y., Wu, C.-I., and Lin, H.-W. (2019). High-Quality Conformal Homogeneous All-Vacuum Deposited CsPbCl_3 Thin Films and Their UV Photodiode Applications. *ACS Appl Mater Interfaces* *11*, 47054–47062. 10.1021/acsami.9b16264.
- S15. Li, X., Wang, Y., Chen, T., Xu, T., Ye, S., Liu, R., Sun, Z., Tan, C., Lv, X., Yang, J., et al. (2022). Unencapsulated CsPbClBr_2 Film Photodetectors Grown by Thermal Vacuum Deposition Exhibit Exceptional Environmental Stability in High-Humidity Air. *ACS Appl Energy Mater* *5*, 8709–8716. 10.1021/acsaem.2c01237.
- S16. Guo, F., Wang, J., Li, Y., Yu, S., Xu, X., Cai, X., Fang, Y., Vayssieres, L., Saidaminov, M.I., and Yang, S. (2022). Postripening Fabrication and Self-Driven Narrowband Photoresponse of Large-Grain, Phase-Pure CsPbBr_3 Films. *Solar RRL* *6*, 2200828. 10.1002/solr.202200828.
- S17. Chen, F., Li, C., Shang, C., Wang, K., Huang, Q., Zhao, Q., Zhu, H., and Ding, J. (2022). Ultrafast Response of Centimeter Scale Thin CsPbBr_3 Single Crystal Film Photodetector for Optical Communication. *Small* *18*, 2203565. 10.1002/smll.202203565.
- S18. Li, Y., Shi, Z.-F., Li, S., Lei, L.-Z., Ji, H.-F., Wu, D., Xu, T.-T., Tian, Y.-T., and Li, X.-J. (2017). High-performance perovskite photodetectors based on solution-processed all-inorganic CsPbBr_3 thin films. *J Mater Chem C Mater* *5*, 8355–8360. 10.1039/C7TC02137B.
- S19. Li, X., Yu, D., Cao, F., Gu, Y., Wei, Y., Wu, Y., Song, J., and Zeng, H. (2016). Healing All-Inorganic Perovskite Films via Recyclable Dissolution-Recrystallization for Compact and Smooth Carrier Channels of Optoelectronic Devices with High Stability. *Adv Funct Mater* *26*, 5903–5912. 10.1002/adfm.201601571.
- S20. Xue, J., Gu, Y., Shan, Q., Zou, Y., Song, J., Xu, L., Dong, Y., Li, J., and Zeng, H. (2017). Constructing Mie-Scattering Porous Interface-Fused Perovskite Films to Synergistically Boost Light Harvesting and Carrier Transport. *Angewandte Chemie* *129*, 5316–5320. 10.1002/ange.201700600.
- S21. Liu, X., Yu, D., Cao, F., Li, X., Ji, J., Chen, J., Song, X., and Zeng, H. (2017). Low-Voltage

- Photodetectors with High Responsivity Based on Solution-Processed Micrometer-Scale All-Inorganic Perovskite Nanoplatelets. *Small* *13*, 1700364. 10.1002/smll.201700364.
- S22. Lin, Q., Armin, A., Burn, P.L., and Meredith, P. (2016). Near infrared photodetectors based on sub-gap absorption in organohalide perovskite single crystals. *Laser Photon Rev* *10*, 1047–1053. 10.1002/lpor.201600215.
- S23. Bao, C., Chen, Z., Fang, Y., Wei, H., Deng, Y., Xiao, X., Li, L., and Huang, J. (2017). Low-Noise and Large-Linear-Dynamic-Range Photodetectors Based on Hybrid-Perovskite Thin-Single-Crystals. *Advanced Materials* *29*, 1703209. 10.1002/adma.201703209.
- S24. Dirin, D.N., Cherniukh, I., Yakunin, S., Shynkarenko, Y., and Kovalenko, M. V. (2016). Solution-Grown CsPbBr₃ Perovskite Single Crystals for Photon Detection. *Chemistry of Materials* *28*, 8470–8474. 10.1021/acs.chemmater.6b04298.
- S25. Song, J., Xu, L., Li, J., Xue, J., Dong, Y., Li, X., and Zeng, H. (2016). Monolayer and Few-Layer All-Inorganic Perovskites as a New Family of Two-Dimensional Semiconductors for Printable Optoelectronic Devices. *Advanced Materials* *28*, 4861–4869. 10.1002/adma.201600225.
- S26. Yang, Z., Jiang, M., Guo, L., Hu, G., Gu, Y., Xi, J., Huo, Z., Li, F., Wang, S., and Pan, C. (2021). A high performance CsPbBr₃ microwire based photodetector boosted by coupling plasmonic and piezo-phototronic effects. *Nano Energy* *85*, 105951. 10.1016/j.nanoen.2021.105951.
- S27. Liu, R., Zhang, J., Zhou, H., Song, Z., Song, Z., Grice, C.R., Wu, D., Shen, L., and Wang, H. (2020). Solution-Processed High-Quality Cesium Lead Bromine Perovskite Photodetectors with High Detectivity for Application in Visible Light Communication. *Adv Opt Mater* *8*, 1901735. 10.1002/adom.201901735.
- S28. Tong, G., Jiang, M., Son, D., Ono, L.K., and Qi, Y. (2020). 2D Derivative Phase Induced Growth of 3D All Inorganic Perovskite Micro–Nanowire Array Based Photodetectors. *Adv Funct Mater* *30*, 2002526. 10.1002/adfm.202002526.
- S29. Han, Q., Bae, S., Sun, P., Hsieh, Y., Yang, Y. (Michael), Rim, Y.S., Zhao, H., Chen, Q., Shi, W., Li, G., et al. (2016). Single Crystal Formamidinium Lead Iodide (FAPbI₃): Insight into the Structural, Optical, and Electrical Properties. *Advanced Materials* *28*, 2253–2258. 10.1002/adma.201505002.
- S30. Qin, X., Yao, Y., Dong, H., Zhen, Y., Jiang, L., and Hu, W. (2016). Perovskite Photodetectors based on CH₃NH₃PbI₃ Single Crystals. *Chem Asian J* *11*, 2675–2679. 10.1002/asia.201600430.
- S31. Ding, J., Fang, H., Lian, Z., Li, J., Lv, Q., Wang, L., Sun, J.-L., and Yan, Q. (2016). A self-powered photodetector based on a CH₃NH₃PbI₃ single crystal with asymmetric electrodes. *CrystEngComm* *18*, 4405–4411. 10.1039/C5CE02531A.
- S32. Deng, H., Dong, D., Qiao, K., Bu, L., Li, B., Yang, D., Wang, H.-E., Cheng, Y., Zhao, Z., Tang, J., et al. (2015). Growth, patterning and alignment of organolead iodide perovskite

- nanowires for optoelectronic devices. *Nanoscale* 7, 4163–4170. 10.1039/C4NR06982J.
- S33. Sutherland, B.R., Johnston, A.K., Ip, A.H., Xu, J., Adinolfi, V., Kanjanaboos, P., and Sargent, E.H. (2015). Sensitive, Fast, and Stable Perovskite Photodetectors Exploiting Interface Engineering. *ACS Photonics* 2, 1117–1123. 10.1021/acsp Photonics.5b00164.
- S34. Liu, C., Wang, K., Yi, C., Shi, X., Du, P., Smith, A.W., Karim, A., and Gong, X. (2015). Ultrasensitive solution-processed perovskite hybrid photodetectors. *J Mater Chem C Mater* 3, 6600–6606. 10.1039/C5TC00673B.
- S35. Kwon, K.C., Hong, K., Van Le, Q., Lee, S.Y., Choi, J., Kim, K.-B., Kim, S.Y., and Jang, H.W. (2016). Inhibition of Ion Migration for Reliable Operation of Organolead Halide Perovskite-Based Metal/Semiconductor/Metal Broadband Photodetectors. *Adv Funct Mater* 26, 4213–4222. 10.1002/adfm.201600405.
- S36. Sim, K.M., Swarnkar, A., Nag, A., and Chung, D.S. (2018). Phase Stabilized α -CsPbI₃ Perovskite Nanocrystals for Photodiode Applications. *Laser Photon Rev* 12, 1700209. 10.1002/lpor.201700209.
- S37. Ding, N., Wu, Y., Xu, W., Lyu, J., Wang, Y., Zi, L., Shao, L., Sun, R., Wang, N., Liu, S., et al. (2022). A novel approach for designing efficient broadband photodetectors expanding from deep ultraviolet to near infrared. *Light Sci Appl* 11, 91. 10.1038/s41377-022-00777-w.
- S38. Waleed, A., Tavakoli, M.M., Gu, L., Hussain, S., Zhang, D., Poddar, S., Wang, Z., Zhang, R., and Fan, Z. (2017). All Inorganic Cesium Lead Iodide Perovskite Nanowires with Stabilized Cubic Phase at Room Temperature and Nanowire Array-Based Photodetectors. *Nano Lett* 17, 4951–4957. 10.1021/acs.nanolett.7b02101.
- S39. Bi, C., Kershaw, S. V., Rogach, A.L., and Tian, J. (2019). Improved Stability and Photodetector Performance of CsPbI₃ Perovskite Quantum Dots by Ligand Exchange with Aminoethanethiol. *Adv Funct Mater* 29, 1902446. 10.1002/adfm.201902446.